

PORTABLE DEVICE BASED OPTICAL SENSORS FOR WATER RELATED  
ENVIRONMENTAL MONITORING

by

Soo Chung

---

Copyright © Soo Chung 2019

A Dissertation Submitted to the Faculty of the

DEPARTMENT OF BIOSYSTEMS ENGINEERING

In Partial Fulfillment of the Requirements

For the Degree of

DOCTOR OF PHILOSOPHY

In the Graduate College

THE UNIVERSITY OF ARIZONA

2019

THE UNIVERSITY OF ARIZONA  
GRADUATE COLLEGE

As members of the Dissertation Committee, we certify that we have read the dissertation prepared by Soo Chung, titled "Portable device based optical sensors for water related environmental monitoring" and recommend that it be accepted as fulfilling the dissertation requirement for the Degree of Doctor of Philosophy.

  
Jeong-Yeol Yoon

Date: Aug. 2<sup>nd</sup>, 2019

  
Donald Slack

Date: Aug. 2<sup>nd</sup>, 2019

  
Lingling An

Date: Aug. 2<sup>nd</sup>, 2019

  
Minkyu Kim

Date: Aug. 2<sup>nd</sup>, 2019

Final approval and acceptance of this dissertation is contingent upon the candidate's submission of the final copies of the dissertation to the Graduate College.



I hereby certify that I have read this dissertation prepared under my direction and recommend that it be accepted as fulfilling the dissertation requirement.

  
Jeong-Yeol Yoon  
Dissertation Committee Chair  
Biosystems Engineering

Date: Aug. 2<sup>nd</sup>, 2019

## STATEMENT BY AUTHOR

This dissertation has been submitted in partial fulfillment of the requirements for an advanced degree at the University of Arizona and is deposited in the University Library to be made available to borrowers under rules of the Library.

Brief quotations from this dissertation are allowable without special permission, provided that an accurate acknowledgement of the source is made. Requests for permission for extended quotation from or reproduction of this manuscript in whole or in part may be granted by the head of the major department or the Dean of the Graduate College when in his or her judgment the proposed use of the material is in the interests of scholarship. In all other instances, however, permission must be obtained from the author.

SIGNED: Soo Chung

## **Acknowledgements**

I would like to thank God for his grace on helping me out in every steps on my journey of Ph.D.

I am highly appreciated and thankful for my mentor and principle investigator, Dr. Jeong-Yeol Yoon for his support, guidance, and encouragement. I also appreciate my Dissertation Committee: Dr. Donald Slack, Dr. Lingling An, and Dr. Minkyu Kim for their support and valuable time.

I thank all of my Biosensors lab colleagues: Tusan Park, Ari Nicolini, Soohee Cho, Katie Klug, Robin Sweeney, Kattika Kaarj, Tiffany Ulep, Matt Bills, Kenneth Schackart, and Alex Day. I would also like to thank the undergraduate members of the biosensors lab who have assisted.

I thank my parents for their love and support. I thank so much my beloved wife, Stella for your support, and cheering me up whenever I feel down.

# Table of Contents

List of Figures .....	10
List of Tables .....	12
Abstract .....	13
Introduction.....	15
1.1 Demand for Health and Environmental Monitoring in the field.....	15
1.2 Conventional Analysis Methods .....	15
1.2.1 Biological Pathogen Analysis .....	15
1.2.2 Chemical and Elemental Analysis .....	17
1.2.3 Plant Health Analysis.....	18
1.3 Hand-held devices for Sensing .....	19
1.3.1 Smartphone .....	19
1.3.2 Raspberry Pi.....	19
1.4 Hand-held Sensing Platform .....	20
1.4.1 Colorimetric method .....	20
1.4.2 Fluorescence-based method.....	20
1.4.3 Spectrometric method .....	21
1.4.4 Flow rate-based method.....	21
1.5 Utilized technique and Analysis methods.....	22
1.5.1 Particle immunoagglutination.....	22
1.5.2 Nonparametric test.....	23
1.5.3 Normalized Difference Vegetation Index .....	23
1.5.4 Principal Component Analysis .....	24

1.5.5 Support Vector Machine .....	25
Conclusion .....	26
References.....	28
Appendix A.....	35
Abstract .....	36
1. Introduction.....	37
2. Results and Discussion .....	41
Benchtop Microscope Assays. ....	41
Specificity Test. ....	44
Smartphone Microscope Assays. ....	45
Smartphone Microscope Assays with Field Water Samples. ....	48
3. Conclusion .....	52
4. Methods.....	53
$\mu$ PAD Fabrication. ....	53
Antibody Conjugation to Fluorescent Particles. ....	53
Norovirus Sample Preparation. ....	53
Specificity Test. ....	55
Water Samples. ....	55
Assay Procedure.....	55
Imaging Particle Aggregation on $\mu$ PADs Using a Benchtop Fluorescence Microscope.....	56
Imaging Particle Aggregation on $\mu$ PADs Using a Smartphone-based Fluorescence Microscope.....	56

Image Analysis for Benchtop Fluorescence Microscopic Images.....	57
Image Analysis for Smartphone-based Fluorescence Microscopic Images. ....	59
Statistical Analysis.....	60
Associated content .....	61
Supporting Information.....	61
Author Information .....	82
Acknowledgment .....	83
References.....	83
Appendix B.....	88
Abstract.....	89
1. Introduction.....	91
2. Materials and Method .....	93
2.1. Various smartphones' abilities in recognizing NIR.....	93
2.2. Chlorophyll solutions.....	94
2.3. Chlorophyll extraction and spectrophotometric quantification from plant leaves .....	94
2.4. Water contents of plant leaves .....	95
2.5. NDVI measurements using a smartphone and an NIR filter .....	95
2.6. Image analysis.....	96
3. Results and discussion .....	98
3.1. Various smartphones' abilities in recognizing NIR.....	98
3.2. Smartphone-acquired NDVI values of chlorophyll solutions.....	99
3.3. Smartphone-acquired NDVI vs. The leaf chlorophyll content .....	101

3.4. Smartphone-acquired NDVI values vs. Water contents of plant leaves .....	102
4. Conclusion .....	103
Acknowledgements.....	104
References.....	104
Appendix C .....	107
Abstract.....	108
1. Introduction.....	109
2. Distance-based detection on LFA or $\mu$ PAD .....	112
3. Capillary flow dynamics-based detection on LFA or $\mu$ PAD.....	117
3. Conclusion .....	125
Acknowledgements.....	126
References.....	126
Appendix D.....	131
ABSTRACT.....	132
1. Introduction.....	133
2. Materials and Method .....	135
2.1. $\mu$ PAD fabrication .....	135
2.2. Oil samples preparation .....	136
2.3. Raspberry Pi device .....	136
2.4. Flow rate analysis .....	137
2.5. Statistical analysis for classification .....	137
3. Results and Discussion .....	139
3.1. Flow rate profiles .....	139

3.2. Oil classification by PCA.....	140
3.3. Oil classification by t-SNE and SVM.....	144
4. Conclusion .....	148
Acknowledgements.....	149
References.....	149

## List of Figures

Figure A-1.....	41
Figure A-2.....	43
Figure A-3.....	45
Figure A-4.....	47
Figure A-5.....	49
Figure A-6.....	50
Figure A-7.....	58
Figure A-S1.....	61
Figure A-S2.....	62
Figure A-S3.....	63
Figure A-S4.....	82
Figure B-1.....	96
Figure B-2.....	97
Figure B-3.....	99
Figure B-4.....	101
Figure B-5.....	102
Figure C-1.....	112
Figure C-2.....	115
Figure C-3.....	118
Figure C-4.....	120
Figure C-5.....	123
Figure C-6.....	124

Figure D-1.....	137
Figure D-2.....	139
Figure D-3.....	140
Figure D-4.....	141
Figure D-5.....	145

## List of Tables

Table C-1 .....	113
Table D-1 .....	142
Table D-2 .....	143
Table D-3 .....	144
Table D- 4 .....	147
Table D-5 .....	148

## **Abstract**

Demand for field-usable analytical devices is growing in many areas, including medical diagnosis, food safety, and environmental monitoring. There is commercially available equipment but they are not intended for use in the field or at home because of high prices and large size. To overcome these shortcomings, portable devices are needed that are easy to fabricate, low-cost, user-friendly and sufficiently sensitive. The spread of smartphones and the development of microcontrollers have the potential to be used as portable diagnostic devices. This dissertation includes a series of three research articles and one review article that is aimed at developing portable water related environmental monitoring devices.

The first project focused on developing a biosensor for the immediate detection of norovirus in a water sample. We visualized norovirus directly on paper microfluidics chip through the addition of antibody-conjugated submicron fluorescent particles using smartphone-based fluorescence microscope. This method allows for the diagnosis of virus close to a single virus particle level in a short amount of time.

The second project demonstrates an optical sensor used to evaluate normalized difference vegetation index (NDVI) from plant leaves using a smartphone camera and 800 nm high-pass filter. NDVI values were correlated with chlorophyll concentration and water content and allowed to predict the health of plants.

The third project details an optical sensor for distinguishing the type and origin of different oils. A Raspberry Pi and camera were used to collect capillary flow rate on paper chip. Depending on the composition and viscosity of each oil, the flow pattern differed and

made it possible to distinguish between samples using principal component analysis (PCA) and the support vector machine classification algorithm (SVM).

The review article introduces capillary flow dynamics-based method using microfluidic paper-based analytic device which has the potential for future applications towards point-of-care diagnostics and field applications.

These articles present some of the directions for developing portable sensors for water related environmental monitoring.

# **Introduction**

## **1.1 Demand for Health and Environmental Monitoring in the field**

Recently, Point-of Care (POC) diagnostic has become an essential keyword in developing sensors. The market for POC diagnostic is prospected to rise to \$11.7 billion dollars by 2024.<sup>1</sup> Existing conventional equipment use in the field is limited by the need for skilled personnel, pre-treatment on samples, and mostly large to carry out. However, a POC diagnostic device aims for rapid diagnosis at the user's location or an industrial site. These POC diagnostics have well developed in the field of medical diagnosis. The major benefit of POC diagnostic devices is that they permit quick and easy diagnosis at places like a person's own home, which makes it possible for many people to detect their diseases in early stage.<sup>2-4</sup> Recognizing their diseases in an earlier stage allows a person to get proper treatment immediately and increases the likelihood of a successful medical intervention. Also, POC diagnostics have applications in the environmental field where it is possible to detect environmental pollution quickly, such as diagnosing heavy metals in water and then avoiding drinking the contaminated water.<sup>5,6</sup>

## **1.2 Conventional Analysis Methods**

### **1.2.1 Biological Pathogen Analysis**

Conventional methods for monitoring pathogens and other contaminants are generally inappropriate for on-site use due to the time-consuming nature of material preparation, large and expensive instrumentation, and the requirement of trained-labor to

safely and effectively use the equipment.<sup>7,8</sup> The major methods for conventional monitoring are polymerase chain reaction (PCR), immunoassay, and microbial culturing.

PCR has become the gold standard for identification and quantification of target genome. PCR amplifies DNA or RNA from biological sample over 20-40 cycles using thermocycler and target primers. This process typically requires 1-2 hours for running and in advance to amplification, it requires pre-treatment such as cell lysis and nucleic acid extraction which obstructs real-time monitoring. Moreover, the cost of primer, other reagents and additional equipment is expensive and too large to move into field. These shortcomings induce the hurdle to use in the field.

Immunoassay uses the specific reaction of antibodies to antigens. For example, enzyme-linked immunosorbent assay (ELISA) can provide rapid results for pathogens. In sandwich ELISA, target sample is added into antibody coated well. Then, the enzyme conjugated secondary antibody is added. After all the conjugation procedures have been completed, the remaining solution is washed out and substrate is added to generate color that indicates the presence of target. However, the sensitivity of ELISA is inferior to PCR and mainly used for qualitative analysis.

Cultivating bacteria and counting the colony forming unit (CFU) is the most classical method for identification and quantification. For virus, it counts plaque-forming units (PFU) which are affected by the growth of host cell. Even though these methods show good efficiency, it requires 8 hours to a few days to culture in proper growth conditions. Additionally, labor is required to ensure proper growth conditions and there is a risk of contamination. Moreover, there are also pathogens (e.g. norovirus) that do not

grow well *in vitro* conditions and only grow *in vivo* conditions. Therefore, it is not suitable for real-time use in the field.

### **1.2.2 Chemical and Elemental Analysis**

Conventional methods for monitoring chemical and elemental analysis methods such as

Chromatography-mass spectrometry and spectroscopy.

Chromatography is a laboratory technique to identify components of a mixture using separation. This method is mainly used to analyze organic compounds, detect and quantify trace elements among various environmental samples, and analyze components such as medicines and pesticides. The mixture is dissolved into a fluid, called the mobile phase, that carries the analytes and flows through a structure called the stationary phase. The various components in the mixture move at different speeds and generate separation through differences in partition coefficient of each component. It can use either gas (Gas chromatography) or liquid (Liquid chromatography) as a carrier. Gas chromatography can analyze rapidly with decent sensitivity and requires only a small number of samples, but the sample must be vaporized without decomposition. Liquid chromatography can analyze more diverse types of samples and have higher accuracy and reproducibility than gas chromatography. However, high pressure pumps are needed to move the samples. Moreover, chromatography is suitable for a qualitative analysis. Mass spectrometry can be coupled with chromatography which is an analytical technique to quantify the concentration of components in mixture using mass-to-charge ratio of ion. The intensity of plot which called mass spectrum represents the concentration of molecules. These devices

allow accurate and sensitive measurement, but they are large and expensive. Additionally, a vacuum system is required for the gas chromatography-mass spectrometry.

### **1.2.3 Plant Health Analysis**

Conventional methods for measuring the health condition of plants are divided by direct and indirect methods, the direct method is similar to the pathogen detection methods, and the spectroscopic and imaging method are mainly used as indirect methods.<sup>9</sup>

Visible and infrared (IR) spectroscopy has been used as non-destructive method for monitoring plant health. This range of spectra contains a lot of information about plant stress. Therefore, it is possible to predict the health of a plant using information from a particular wavelength band.<sup>10</sup> Several indexes have been studied and used to make worthy of these information. For example, normalized difference vegetation index (NDVI) can be used to observe live green vegetation<sup>11</sup>, water band index for water content<sup>10</sup>, and red-edge vegetation stress index to estimate chlorophyll content.<sup>12</sup> However, the information in the visible wavelength alone is not superior to that of the human eye, it must be supplemented by information in the NIR or IR area, and the spectroscopy that can be obtained in those ranges are expensive and require training in their use.

Hyperspectral imaging has become a spotlighting topic in the field of precision agriculture. The hyperspectral image acquires the spectral reflectance of each pixel in the image from the electromagnetic spectrum. It is similar to multispectral imaging, but hyperspectral imaging uses a continuous range of wavelength from visible to IR and obtains more information. Therefore, there are many attempts to monitor the health of plants by using hyperspectral imaging.<sup>13,14</sup> However, an extensive dataset is required to

use statistical classification algorithms which require time-consuming analyses. Moreover, the price of device itself is highly expensive.

## **1.3 Hand-held devices for Sensing**

### **1.3.1 Smartphone**

Recently, the smartphone market has grown rapidly and is widespread to many users. Smartphone cameras allow the user to collect images and/or signal and the software can be used as data processing module.<sup>15</sup> Therefore, the smartphone has emerged as an ideal portable low-cost signal acquisition and analyzing tool for diagnostics. For this reason, the use of smartphone as point-of-care to biological and chemical sensor has been studied in many areas. The biological and chemical target respond to target-specific components and indicate a specific signal which can be represented by color, fluorescence scattering, and flow rate.

### **1.3.2 Raspberry Pi**

Raspberry Pi is a type of microcontroller that is useful tool for data acquisition and analysis.<sup>16,17</sup> The performance of the latest Raspberry Pi is comparable to a certain extent of computer with a 1.4GHz 64-bit quad-core processor of central processing units (CPU). This device is easy to access, learn and improve since many of the program codes are open source. Its program language is Python, but it can also be changed to C ++ or Java which are common languages. Also, many accessories such as a camera or touchscreen make it more convenient for user to develop into a device.

## **1.4 Hand-held Sensing Platform**

### **1.4.1 Colorimetric method**

Currently, most of the smartphone and Raspberry Pi cameras use complementary metal oxide semiconductor (CMOS) array which can obtain red, green, and blue (RGB) color value through utilizing Bayer color filter arrays.<sup>18</sup> This inexpensive CMOS array can produce stable and reproducible visual results. This allows measurements of the colorimetric changes more accurately compared to when it is performed with naked eye in the past, which was subjective.<sup>19</sup> Therefore, colorimetric assay has been applied to many field research studies such as disease diagnoses,<sup>20</sup> metal ion detection,<sup>21</sup> and other biological components<sup>22</sup> with these portable devices. However, it is difficult to precisely analyze the signal with the obtained image as it is difficult to control lighting conditions such as sunlight, indoor lighting, and camera-to-target alignment with these cameras. Therefore, an external frame is often required to eliminate the difference in lighting conditions and camera position.<sup>23</sup>

### **1.4.2 Fluorescence-based method**

Fluorescence imaging is an effective method to improve the resolution of the colorimetric image using fluorescence label samples such as DNA, virus and nanoparticles.<sup>24,25</sup> The fluorescence intensity is related to the concentration of the excitation source which absorbs energy from a specific wavelength and releases a certain range of emission spectrum. Typically, an optical filter such as band-, high-, pass filter is

required for a CMOS array since it is not able to distinguish small differences in wavelength.

Many groups have used fluorescence-based detection methods using smartphone to quantify biochemical targets such as bacterial pathogens, DNA, and antibody<sup>26-28</sup>

### **1.4.3 Spectrometric method**

Spectrometric method can be utilized in diverse area of science anytime electromagnetic radiation interacts with materials. Optical spectrum contains a lot of information that characterizes target quantities and properties.<sup>29</sup> The performance of many smartphone spectrometers in recent years are comparable to that of conventional benchtop spectrometer in terms of accuracy and wavelength resolution.<sup>30</sup> The most common detection method with smartphone spectrometers is absorption. Spectroscopy attachments on smartphone camera such as micro-prism array or optical filter allow capture of wavelengths by spatially distinguishing them.<sup>31,32</sup>

In Appendix B, chlorophyll content, which is a good indicator of photosynthetic activity and the health of a plant, was estimated in non-destructive way by measuring the NIR wavelength and Red wavelength through smartphone camera and high-pass filter

### **1.4.4 Flow rate-based method**

Lateral flow assay (LFA) and microfluidic paper-based analytic device ( $\mu$ PAD) is appropriate for use for flow rate-based detection method. This method works when liquid flows on a paper strip, through capillary action, and time-dependent changes of flow rate

can provide information of composition of components or the amount (concentration) of targets. It is not affected by ambient lighting and does not require additional devices to conduct a sample flow experiment. Recently, this method was demonstrated when it estimated *Escherichia coli* K12 and Zika virus concentration.<sup>33</sup> Appendix C introduces the future direction of the method in more detail. Furthermore, Appendix D describes a method where crude oil flows through a paper chip and a Raspberry Pi camera collects a flow rate profile to estimate the geographic origin of the crude oils identify oil tankers that have spilt oil.

## **1.5 Utilized technique and Analysis methods**

### **1.5.1 Particle immunoagglutination**

Particle immunoagglutination detection method uses antibody-conjugated polystyrene particles to identify the target antigen. Particles generate agglutination with decent specificity in the presence of a target according to antibody-antigen interaction. The increase of immunoagglutination indicates a higher concentration of target. Particle immunoagglutination can be detected through Mie scattering measurements or fluorescent imaging (fluorescent particle or dye required). A Mie scattering profile is dependent on the particle size and when the size changes from a singlet to an aggregated particle, the scattering profile changes. Therefore, it is possible to measure the target concentration based on the change in the scattering profile from the singlet particle. Moreover, fluorescent imaging measures the intensity of particles and distinguishes the aggregated

particles from the background through image processing. The increase in the number of aggregated particles is then related to target concentration.

### **1.5.2 Nonparametric test**

Nonparametric test and distribution free methods which do not depend on the assumptions of a normal distribution and can reduce errors that may occur without satisfying this assumption. A nonparametric test is generally less precise compared to the parametric test and statistical verification ability to tease out differences between two groups is weaker. However, while parametric test needs a normal distribution based on Central Limit Theorem which can be applied for large sample sizes, nonparametric test is suitable in small number of samples and the results are easy to interpret. In Appendix A, a nonparametric test is performed because the sample number was small and because of small samples size there are no obvious tests to determine the distribution of underlying data.

### **1.5.3 Normalized Difference Vegetation Index**

The NDVI can used for remote sensing of overall health of plants and can predict crop yield and biomass - the main goal of precision agriculture.<sup>34</sup> This index uses visible (around 660 nm) and NIR (around 800nm) wavelength reflectance which are related to photosynthetically active radiation absorbed by a plant.<sup>35</sup> The NDVI is calculated from this equation:  $(\text{NIR reflectance} - \text{red reflectance}) / (\text{NIR reflectance} + \text{red reflectance})$ . The

value varies between -1.0 and 1.0 and the closer the value is to 1, the healthier the state is of the plant.

Many research studies have been carried out to estimate yield<sup>36</sup>, Leaf Area Index<sup>37</sup>, green biomass<sup>38</sup> using satellite or unmanned aircraft such as a drone. In Appendix B, similar performance was achieved using a smartphone, which is simpler than the equipment used in these previous studies.

#### **1.5.4 Principal Component Analysis**

Principal component analysis (PCA) is a statistical method uses an orthogonal transformation to classify a set of the associated variables into a small number of new variables that contain most of the information. Through this method, multi-dimensional data can be reduced to a lower dimension (usually 2 or 3).

Principal component one (PC1) would be the data that explains the largest portion of the variance in the data set, while PC2, PC3 and on would continuously indicate the next lowest portion of the variance in the data set. Therefore, it can determine the most important elements from the data by deciding the PC that explains highest portion of the data. All the dataset displayed on the score plot which axis are PC and the location indicate the similarities or differences between the data set which even look random.

In Appendix D, PCA is used to find out the main components for representing the variation in the dataset that has 25 dimensions. PCA determines the most influential component of such a high dimensional dataset which is almost impossible without a statistical tool.

### **1.5.5 Support Vector Machine**

Support vector machine (SVM) is a supervised learning algorithm used for data classification and categorizing using pattern recognition and data mapping. Classification model designed to maximize the margin that exist between groups using training data and is used to determine which group a new set of data belongs to. While PCA can only perform linear classification SVM can achieve non-linear classification using kernel trick and is able to distinguish data more efficiently. Due to this improvement, SVM algorithm has been applied to classify proteins,<sup>39</sup> heavy metal,<sup>40</sup> and pest detection.<sup>41</sup>

## Conclusion

Appendix A, B, and D covers development of 3 different portable diagnostic sensors and Appendix C presents the new direction to move forward for various water related environmental monitoring. Through these researches, portable devices were developed that were able to detect targets more easily, quickly and obtained the desired information using simple assays. These portable assays reduced cost, time, and supplies that are required to monitor or obtain such results.

First, we developed a portable fluorescence sensing platform using smartphone and microscope attachment towards norovirus detection in various water samples. Drinking water which containing norovirus or eating food washed with that water often causes serious gastroenteritis. Norovirus can be outbreak at very low concentration but the detection limit of the assays up to now were insufficient and lacked effectiveness. However, our device can detect close to the single-virus level which is enough to detect an outbreak which require a minimum number of 10 virus particles. It is expected to prevent people from drinking virus containing water or food using this device more rapidly and can be particularly useful in places where it is difficult to use commercial equipment such as houses or ships.

The second smartphone-based sensor uses spectrometric method using red and NIR reflectance wavelength from a plant to estimate chlorophyll content and water stress. Many people grow plants, but it is very difficult to judge the health of the plants with the naked eye. In particular, it is difficult to determine when and how much water should be given, and it can cause death by missing the timing of watering. By attaching optical high-pass filter to smartphone plant health indicators can be analyzed which is also related to water

stress. This simple device makes it easy to check plant health at home or in the office for the people who are not experienced in growing plants.

Third, capillary flow dynamic-based method was explained with potential future applications for medical diagnostics and water related environmental monitoring. This method is effective for the detection of heavy metal contamination or biological pathogen in rivers or reservoirs since it is based on measuring the flow rate of liquid samples flowing through the porous paper.

Fourth, a sensor that can distinguish origin of crude oil according to its composition was developed by measuring flow rate profiles using microcontroller and its camera. The oil spills from the ship not only pollutes the sea but can also lead to big accidents. Therefore, it is necessary to analyze the oil composition at an early stage to find suspicious vessels and warn them. Currently, the samples are being taken to the laboratory for analysis, which takes too long and when the results come out, the ship has already left the port. However, our device can rapidly categorize the types and origin of oil samples and can be used on the ship to analyze the oils collected from surface of the sea water and find out ships that are suspected of leaking.

## References

- (1) Point-of-Care Diagnostics Market to touch US\$11.7 bn by 2024 | TMR  
<https://www.transparencymarketresearch.com/pressrelease/care-diagnostics-market.htm> (accessed Jun 26, 2019).
- (2) Su, J.; Xu, J.; Chen, Y.; Xiang, Y.; Yuan, R.; Chai, Y. Personal Glucose Sensor for Point-of-Care Early Cancer Diagnosis. *Chem. Commun.* **2012**, 48 (55), 6909–6911. <https://doi.org/10.1039/C2CC32729E>.
- (3) Kaarj, K.; Akarapipad, P.; Yoon, J.-Y. Simpler, Faster, and Sensitive Zika Virus Assay Using Smartphone Detection of Loop-Mediated Isothermal Amplification on Paper Microfluidic Chips. *Sci. Rep.* **2018**, 8 (1). <https://doi.org/10.1038/s41598-018-30797-9>.
- (4) Hwang, S. G.; Ha, K.; Guk, K.; Lee, D. K.; Eom, G.; Song, S.; Kang, T.; Park, H.; Jung, J.; Lim, E.-K. Rapid and Simple Detection of Tamiflu-Resistant Influenza Virus: Development of Oseltamivir Derivative-Based Lateral Flow Biosensor for Point-of-Care (POC) Diagnostics. *Sci. Rep.* **2018**, 8 (1). <https://doi.org/10.1038/s41598-018-31311-x>.
- (5) Chen, G.-H.; Chen, W.-Y.; Yen, Y.-C.; Wang, C.-W.; Chang, H.-T.; Chen, C.-F. Detection of Mercury(II) Ions Using Colorimetric Gold Nanoparticles on Paper-Based Analytical Devices. *Anal. Chem.* **2014**, 86 (14), 6843–6849. <https://doi.org/10.1021/ac5008688>.
- (6) Sumriddetchkajorn, S.; Chaitavon, K.; Intaravanne, Y. Mobile-Platform Based Colorimeter for Monitoring Chlorine Concentration in Water. *Sens. Actuators B Chem.* **2014**, 191, 561–566. <https://doi.org/10.1016/j.snb.2013.10.024>.

- (7) Mabey, D.; Peeling, R. W.; Ustianowski, A.; Perkins, M. D. Diagnostics for the Developing World. *Nat. Rev. Microbiol.* **2004**, *2* (3), 231.  
<https://doi.org/10.1038/nrmicro841>.
- (8) Martinez, A. W.; Phillips, S. T.; Whitesides, G. M.; Carrilho, E. Diagnostics for the Developing World: Microfluidic Paper-Based Analytical Devices. *Anal. Chem.* **2010**, *82* (1), 3–10. <https://doi.org/10.1021/ac9013989>.
- (9) Sankaran, S.; Mishra, A.; Ehsani, R.; Davis, C. A Review of Advanced Techniques for Detecting Plant Diseases. *Comput. Electron. Agric.* **2010**, *72* (1), 1–13.  
<https://doi.org/10.1016/j.compag.2010.02.007>.
- (10) Xu, H. R.; Ying, Y. B.; Fu, X. P.; Zhu, S. P. Near-Infrared Spectroscopy in Detecting Leaf Miner Damage on Tomato Leaf. *Biosyst. Eng.* **2007**, *96* (4), 447–454. <https://doi.org/10.1016/j.biosystemseng.2007.01.008>.
- (11) Tian, F.; Brandt, M.; Liu, Y. Y.; Verger, A.; Tagesson, T.; Diouf, A. A.; Rasmussen, K.; Mbow, C.; Wang, Y.; Fensholt, R. Remote Sensing of Vegetation Dynamics in Drylands: Evaluating Vegetation Optical Depth (VOD) Using AVHRR NDVI and in Situ Green Biomass Data over West African Sahel. *Remote Sens. Environ.* **2016**, *177*, 265–276. <https://doi.org/10.1016/j.rse.2016.02.056>.
- (12) Naidu, R. A.; Perry, E. M.; Pierce, F. J.; Mekuria, T. The Potential of Spectral Reflectance Technique for the Detection of Grapevine Leafroll-Associated Virus-3 in Two Red-Berried Wine Grape Cultivars. *Comput. Electron. Agric.* **2009**, *66* (1), 38–45. <https://doi.org/10.1016/j.compag.2008.11.007>.

- (13) Lowe, A.; Harrison, N.; French, A. P. Hyperspectral Image Analysis Techniques for the Detection and Classification of the Early Onset of Plant Disease and Stress. *Plant Methods* **2017**, *13* (1), 80. <https://doi.org/10.1186/s13007-017-0233-z>.
- (14) Xie, C.; Yang, C.; He, Y. Hyperspectral Imaging for Classification of Healthy and Gray Mold Diseased Tomato Leaves with Different Infection Severities. *Comput. Electron. Agric.* **2017**, *135*, 154–162. <https://doi.org/10.1016/j.compag.2016.12.015>.
- (15) Yetisen, A. K.; Akram, M. S.; Lowe, C. R. Paper-Based Microfluidic Point-of-Care Diagnostic Devices. *Lab. Chip* **2013**, *13* (12), 2210. <https://doi.org/10.1039/c3lc50169h>.
- (16) Gomez-Cruz, J.; Nair, S.; Manjarrez-Hernandez, A.; Gavilanes-Parra, S.; Ascanio, G.; Escobedo, C. Cost-Effective Flow-through Nanohole Array-Based Biosensing Platform for the Label-Free Detection of Uropathogenic E. Coli in Real Time. *Biosens. Bioelectron.* **2018**, *106*, 105–110. <https://doi.org/10.1016/j.bios.2018.01.055>.
- (17) Ting, H.; Hu, J.-B.; Hsieh, K.-T.; L. Urban, P. A Pinch-Valve Interface for Automated Sampling and Monitoring of Dynamic Processes by Gas Chromatography-Mass Spectrometry. *Anal. Methods* **2014**, *6* (13), 4652–4660. <https://doi.org/10.1039/C4AY00637B>.
- (18) Ulep, T.-H.; Yoon, J.-Y. Challenges in Paper-Based Fluorogenic Optical Sensing with Smartphones. *Nano Converg.* **2018**, *5* (1), 14. <https://doi.org/10.1186/s40580-018-0146-1>.

- (19) Zhang, D.; Liu, Q. Biosensors and Bioelectronics on Smartphone for Portable Biochemical Detection. *Biosens. Bioelectron.* **2016**, *75*, 273–284.  
<https://doi.org/10.1016/j.bios.2015.08.037>.
- (20) Mei, Q.; Jing, H.; Li, Y.; Yisibashaer, W.; Chen, J.; Nan Li, B.; Zhang, Y. Smartphone Based Visual and Quantitative Assays on Upconversion Paper Sensor. *Biosens. Bioelectron.* **2016**, *75*, 427–432.  
<https://doi.org/10.1016/j.bios.2015.08.054>.
- (21) Yetisen, A. K.; Montelongo, Y.; Qasim, M. M.; Butt, H.; Wilkinson, T. D.; Monteiro, M. J.; Yun, S. H. Photonic Nanosensor for Colorimetric Detection of Metal Ions. *Anal. Chem.* **2015**, *87* (10), 5101–5108.  
<https://doi.org/10.1021/ac504274q>.
- (22) Bueno, L.; N. Meloni, G.; M. Reddy, S.; C. Paixão, T. R. L. Use of Plastic-Based Analytical Device, Smartphone and Chemometric Tools to Discriminate Amines. *RSC Adv.* **2015**, *5* (26), 20148–20154. <https://doi.org/10.1039/C5RA01822F>.
- (23) Roda, A.; Michelini, E.; Zangheri, M.; Di Fusco, M.; Calabria, D.; Simoni, P. Smartphone-Based Biosensors: A Critical Review and Perspectives. *TrAC Trends Anal. Chem.* **2016**, *79*, 317–325. <https://doi.org/10.1016/j.trac.2015.10.019>.
- (24) Wei, Q.; Luo, W.; Chiang, S.; Kappel, T.; Mejia, C.; Tseng, D.; Chan, R. Y. L.; Yan, E.; Qi, H.; Shabbir, F.; et al. Imaging and Sizing of Single DNA Molecules on a Mobile Phone. *ACS Nano* **2014**, *8* (12), 12725–12733.  
<https://doi.org/10.1021/nn505821y>.

- (25) Zhu, H.; Yaglidere, O.; Su, T.-W.; Tseng, D.; Ozcan, A. Cost-Effective and Compact Wide-Field Fluorescent Imaging on a Cell-Phone. *Lab. Chip* **2011**, *11* (2), 315–322. <https://doi.org/10.1039/C0LC00358A>.
- (26) F. Fronczek, C.; San Park, T.; K. Harshman, D.; M. Nicolini, A.; Yoon, J.-Y. Paper Microfluidic Extraction and Direct Smartphone-Based Identification of Pathogenic Nucleic Acids from Field and Clinical Samples. *RSC Adv.* **2014**, *4* (22), 11103–11110. <https://doi.org/10.1039/C3RA47688J>.
- (27) Yu, H.; Tan, Y.; Cunningham, B. T. Smartphone Fluorescence Spectroscopy. *Anal. Chem.* **2014**, *86* (17), 8805–8813. <https://doi.org/10.1021/ac502080t>.
- (28) Arts, R.; den Hartog, I.; Zijlema, S. E.; Thijssen, V.; van der Beelen, S. H. E.; Merkx, M. Detection of Antibodies in Blood Plasma Using Bioluminescent Sensor Proteins and a Smartphone. *Anal. Chem.* **2016**, *88* (8), 4525–4532. <https://doi.org/10.1021/acs.analchem.6b00534>.
- (29) Valeur, B.; Brochon, J.-C. *New Trends in Fluorescence Spectroscopy: Applications to Chemical and Life Sciences*; Springer Science & Business Media, 2012.
- (30) Das, A. J.; Wahi, A.; Kothari, I.; Raskar, R. Ultra-Portable, Wireless Smartphone Spectrometer for Rapid, Non-Destructive Testing of Fruit Ripeness. *Sci. Rep.* **2016**, *6*, 32504. <https://doi.org/10.1038/srep32504>.
- (31) Wang, L.-J.; Chang, Y.-C.; Sun, R.; Li, L. A Multichannel Smartphone Optical Biosensor for High-Throughput Point-of-Care Diagnostics. *Biosens. Bioelectron.* **2017**, *87*, 686–692. <https://doi.org/10.1016/j.bios.2016.09.021>.

- (32) Gallegos, D.; D. Long, K.; Yu, H.; P. Clark, P.; Lin, Y.; George, S.; Nath, P.; T. Cunningham, B. Label-Free Biodetection Using a Smartphone. *Lab. Chip* **2013**, *13* (11), 2124–2132. <https://doi.org/10.1039/C3LC40991K>.
- (33) Klug, K. E.; Reynolds, K. A.; Yoon, J.-Y. A Capillary Flow Dynamics-Based Sensing Modality for Direct Environmental Pathogen Monitoring. *Chem. – Eur. J.* **2018**, *24* (23), 6025–6029. <https://doi.org/10.1002/chem.201800085>.
- (34) Berger, A.; Ettlin, G.; Quincke, C.; Rodríguez-Bocca, P. Predicting the Normalized Difference Vegetation Index (NDVI) by Training a Crop Growth Model with Historical Data. *Comput. Electron. Agric.* **2019**, *161*, 305–311. <https://doi.org/10.1016/j.compag.2018.04.028>.
- (35) Stanton, C.; Starek, M. J.; Elliott, N.; Brewer, M.; Maeda, M. M.; Chu, T. Unmanned Aircraft System-Derived Crop Height and Normalized Difference Vegetation Index Metrics for Sorghum Yield and Aphid Stress Assessment. *J. Appl. Remote Sens.* **2017**, *11* (2), 026035. <https://doi.org/10.1117/1.JRS.11.026035>.
- (36) Stroppiana, D.; Migliazzi, M.; Chiarabini, V.; Crema, A.; Musanti, M.; Franchino, C.; Villa, P. Rice Yield Estimation Using Multispectral Data from UAV: A Preliminary Experiment in Northern Italy. In *2015 IEEE International Geoscience and Remote Sensing Symposium (IGARSS)*; 2015; pp 4664–4667. <https://doi.org/10.1109/IGARSS.2015.7326869>.
- (37) Shabanov, N. V.; Dong Huang; Wenzhe Yang; Tan, B.; Knyazikhin, Y.; Myneni, R. B.; Ahl, D. E.; Gower, S. T.; Huete, A. R.; Aragao, L. E. O. C.; et al. Analysis and Optimization of the MODIS Leaf Area Index Algorithm Retrievals over Broadleaf

Forests. *IEEE Trans. Geosci. Remote Sens.* **2005**, *43* (8), 1855–1865.

<https://doi.org/10.1109/TGRS.2005.852477>.

- (38) Wylie, B. K.; Meyer, D. J.; Tieszen, L. L.; Mannel, S. Satellite Mapping of Surface Biophysical Parameters at the Biome Scale over the North American Grasslands: A Case Study. *Remote Sens. Environ.* **2002**, *79* (2), 266–278.  
[https://doi.org/10.1016/S0034-4257\(01\)00278-4](https://doi.org/10.1016/S0034-4257(01)00278-4).
- (39) Tahir, M.; Khan, A. Protein Subcellular Localization of Fluorescence Microscopy Images: Employing New Statistical and Texton Based Image Features and SVM Based Ensemble Classification. *Inf. Sci.* **2016**, *345*, 65–80.  
<https://doi.org/10.1016/j.ins.2016.01.064>.
- (40) Klug Katherine E.; Jennings Christian M.; Lytal Nicholas; An Lingling; Yoon Jeong-Yeol. Mie Scattering and Microparticle-Based Characterization of Heavy Metal Ions and Classification by Statistical Inference Methods. *R. Soc. Open Sci.* **6** (5), 190001. <https://doi.org/10.1098/rsos.190001>.
- (41) Ebrahimi, M. A.; Khoshtaghaza, M. H.; Minaei, S.; Jamshidi, B. Vision-Based Pest Detection Based on SVM Classification Method. *Comput. Electron. Agric.* **2017**, *137*, 52–58. <https://doi.org/10.1016/j.compag.2017.03.016>.

## Appendix A

### Smartphone-based paper microfluidic particulometry of norovirus from environmental water samples at single copy level

Soo Chung,<sup>†</sup> Lane E. Breshears,<sup>‡</sup> Sean Perea,<sup>€</sup> Christina M. Morrison,<sup>§</sup> Walter Q. Betancourt,<sup>§</sup> Kelly A. Reynolds,<sup>||</sup> and Jeong-Yeol Yoon<sup>\*,†</sup>

<sup>†</sup>Department of Biosystems Engineering, <sup>‡</sup>Department of Biomedical Engineering, <sup>€</sup>Department of Chemical and Environmental Engineering, <sup>§</sup>Department of Soil, Water and Environmental Science, <sup>||</sup>Mel and Enid Zuckerman College of Public Health, The University of Arizona, Tucson, Arizona 85721, United States

Received: March 20, 2019

Accepted: June 14, 2019

Published June 27, 2019

Corresponding author: [jyyoon@email.arizona.edu](mailto:jyyoon@email.arizona.edu).

<https://pubs.acs.org/doi/abs/10.1021/acsomega.9b00772>

ACS Omega © 2019 American Chemical Society

## **Abstract**

Human enteric viruses can be highly infectious and thus capable of causing disease upon ingestion of low doses ranging from  $10^0$  to  $10^2$  virions. Norovirus is a good example with a minimum infectious dose as low as a few tens of virions, that is, below femtogram scale. Norovirus detection from commonly implicated environmental matrices (water and food) involves complicated concentration of viruses and/or amplification of the norovirus genome, thus rendering detection approaches not feasible for field applications. In this work, norovirus detection was performed on a microfluidic paper analytic device without using any sample concentration or nucleic acid amplification steps by directly imaging and counting on-paper aggregation of antibody-conjugated, fluorescent submicron particles. An in-house developed smartphone-based fluorescence microscope and an image-processing algorithm isolated the particles aggregated by antibody-antigen binding, leading to an extremely low limit of norovirus detection, as low as 1 genome copy/ $\mu\text{L}$  in deionized water and 10 genome copies/ $\mu\text{L}$  in reclaimed wastewater.

**KEYWORDS:** fluorescence microscopy, particle immunoassay, microfluidic device,  $\mu\text{PAD}$ , waterborne pathogen

## 1. Introduction

Human enteric viruses are small infectious agents that can cause gastrointestinal disease upon ingestion of very low doses. Detection of these viruses requires an extremely low limit of detection (LOD), especially when assessing viruses in reclaimed wastewater or unconfined aquifers used as sources of drinking water. Norovirus is one of such well-known examples and is the most common cause of epidemic and sporadic gastroenteritis worldwide.<sup>1</sup> Studies have indicated that norovirus infection can occur upon exposure to as few as 18 virions.<sup>2,3</sup> Highly sensitive detection methods are needed for assessing exposure to norovirus, especially considering that the methods for virus recovery and concentration from environmental matrices are rather inefficient. In addition, the infectivity of human noroviruses by in vitro cell culture has proven to be quite complex (only possible in stem cell-derived human enteroids),<sup>4</sup> which prevents the use of traditional culture-based assays for evaluating virus infectivity in environmental matrices. Because of this limitation, norovirus has been assayed by either reverse transcription polymerase chain reaction (RT-PCR)<sup>5</sup> or sandwich immunoassay<sup>6</sup> techniques. While RT-PCR-based techniques do provide necessary specificity for detection and identification of norovirus, these molecular methods are susceptible to inhibition by multiple components associated with environmental matrices and fail to provide sufficient rapidity and field-applicability.<sup>7</sup> Immunoassay techniques are simpler than RT-PCR and have the potential to be incorporated on a microfluidic platform. Specifically, microfluidic paper analytic devices ( $\mu$ PADs) have shown numerous advantages over silicone-based microfluidic devices, as they are lightweight, easy to fabricate via wax printing (no lithography), use spontaneous flow by capillary action, and have potential on-chip filtration capability.<sup>8,9</sup> However,

optical detection of low concentrations of pathogens has rarely been demonstrated on paper substrates because paper is optically opaque and non-homogeneous (porous), generating substantial background scatter and reflection. So far, single virus copy level detection of norovirus has rarely been demonstrated on paper substrates (including lateral flow assays and  $\mu$ PADs). While single copy level detection of other virus targets has indeed been demonstrated on paper substrates (20 copies of Ebola, 20 copies/ $\mu$ L of pseudorabies, and 1 copy/ $\mu$ L of HIV), all of them required nucleic acid amplifications, most notably isothermal methods such as loop-mediated isothermal amplification (LAMP).<sup>10-12</sup> Such methods are not sufficiently simple for field-based applications (requiring a heater and thermostat system plus an expensive isothermal amplification kit) and cannot be considered near-real-time (just the amplification part can take from 15 min to 2.5 h). As described previously, immunoassay on  $\mu$ PAD without sample concentration and/or nucleic acid amplification is the ideal method for field-based norovirus detection, which has unfortunately not been demonstrated at the single virus copy level. The LODs of paper-based norovirus immunoassays ranged from  $10^4$  to  $10^6$  copies/ $\mu$ L (=10 fg/ $\mu$ L to 1 pg/ $\mu$ L, as the weight of a single norovirus particle is approximately 10 ag considering its diameter of 35–40 nm)<sup>13</sup> without concentration or amplification<sup>14,15</sup> and  $10^2$  copies/ $\mu$ L with 1 h reaction of signal amplification.<sup>16</sup>

In this work, we attempted to “visualize” the norovirus-induced particle immunoagglutination down to the single virus copy level directly on a  $\mu$ PAD toward field-based applications. Antibody-conjugated, submicron, fluorescent polystyrene particles were used on  $\mu$ PAD to quantify norovirus. The  $\mu$ PAD allows the antibody-conjugated particles and norovirus to “flow” through paper pores spontaneously via capillary action,

which is much faster and more effective than passive, diffusional mixing. As the submicron particles move much slower than norovirus, unbound noroviruses can also be washed from the antibody-conjugated particles, potentially eliminating a separate washing step.<sup>17</sup> The extent of particle aggregation caused by antibody–antigen binding was correlated to the norovirus concentration in the samples. A smartphone-based fluorescence microscope was used to identify and quantify these aggregated particles to provide additional field applicability. Only the aggregated particles could be isolated through image processing, enabling extremely sensitive detection down to the single virus copy level. Neither sample concentration nor nucleic acid amplification steps are necessary due to such an extremely low LOD. This novel method is wholly different from other optical biosensing methods where their signals are ensemble-averaged, that is, specific, nonspecific, and background signals are not fully isolated. By securing direct evidence of particle aggregation, credibility and accuracy of the assay could be improved. In addition, it is also entirely different from other imaging-based virus counting methods, where host cells are infected with target viruses.<sup>18</sup> Such methods require in vitro cultivation of noroviruses, which is costly and time-intensive,<sup>19</sup> and most importantly, are complex and difficult for norovirus.

To accomplish our goal, we designed and tested a smartphone-based fluorescence microscope to image aggregated particles directly on a wax-printed  $\mu$ PAD (Figure A-1a). In this novel method, norovirus target solutions (5  $\mu$ L each) were first loaded on  $\mu$ PADs, followed by the addition of antibodyconjugated, yellow-green fluorescent polystyrene particle suspension that resulted in particle aggregation (i.e., immunoagglutination). This alternative approach enabled the antibody-conjugated particles to spread and flow through the entire channel, allowing them to be imaged separately and minimizing nonspecific

aggregation. In addition, much lower concentration of the antibody-conjugated particles (0.001– 0.002%) was used for the particle suspension than those used in other particle immunoassays, which also contributed to minimizing nonspecific aggregation. A smartphone-based fluorescence microscope (Figure A-1b) was constructed to fluorescently image the several different areas of a  $\mu$ PAD channel. Through a novel image processing algorithm, only the aggregated particles were isolated to relate them to the norovirus concentration. Field water samples-tap water and reclaimed wastewater-were also evaluated.

The overarching aim of this work is to demonstrate extremely low LOD, preferably near to the single virus copy level (corresponding to  $\sim 10$  ag), in a rapid and field-ready manner using a  $\mu$ PAD and smartphone-based fluorescence microscopy.

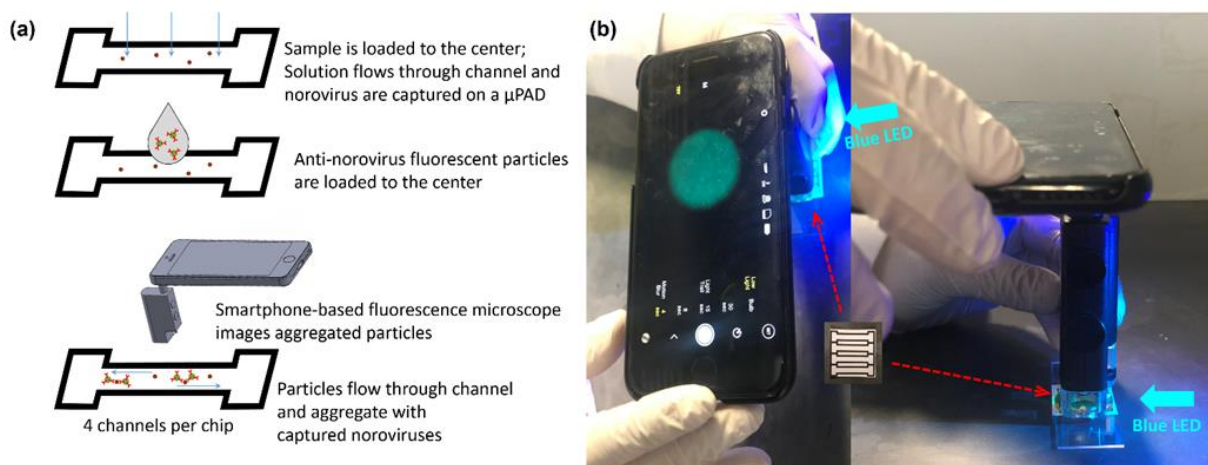


Figure A- 1. Schematic illustration of norovirus assay on  $\mu$ PAD using a smartphone-based fluorescence microscope. (a) 5  $\mu$ L of norovirus solutions are added directly to the main channel of  $\mu$ PAD (made out of nitrocellulose), followed by 2  $\mu$ L of anti-norovirus particle suspension (0.001% w/v). Solutions spread throughout the entire channel by capillary action, which are imaged by a smartphone-based fluorescence microscope. (b) A blue LED (480 nm) is irradiating the  $\mu$ PAD from the side. A smartphone with a microscope attachment and a bandpass filter ( $525 \pm 20$  nm; green emission) captures the fluorescent images of a  $\mu$ PAD.

Photograph courtesy of Soo Chung and Sean Perea. Copyright 2019.

## 2. Results and Discussion

**Benchtop Microscope Assays.** Initially,  $\mu$ PAD assays were conducted for assessing the norovirus capsids, using a benchtop fluorescence microscope and subsequent ImageJ analysis. All serial dilutions were made in 1 mL volume and vortex-mixed to ensure that there were sufficient amounts of norovirus in each dilution even at the lowest concentration. For each assay, 4 different areas of a single channel were imaged. Through

size analysis, the locations of fluorescent particles (both non-aggregated and aggregated) could easily be determined, which showed the pixel intensities of at least 100 (out of 255). Distinction could also be made between non-aggregated and aggregated particles using the pixel area of 50. Therefore, the raw images were processed to eliminate the pixels with < 100 intensity (to remove background) and the pixel area < 50 (to remove non-aggregated particles). From these 4 processed images from a single  $\mu$ PAD channel, the number of pixels were added together to yield a single data point. This number corresponded to the extent of particle aggregation and thus norovirus concentration. Experiments were repeated 3-4 times, each time using a different  $\mu$ PAD. Representative zoomed-in images (raw and processed) are provided in Figure A-2 to the left to better represent the aggregated particles. To confirm whether the pixel area truly represented the particle size and distinguished the aggregated from non-aggregated particles, fluorescence and light microscopic images were obtained for the aggregated particles on a  $\mu$ PAD and processed in the same manner (Figure A-S1). Two different types of particles were observed in fluorescence images, where the smaller ones potentially represent the non-aggregated particles and the bigger ones the aggregated particles. Note that the particle size (0.5  $\mu$ m) is comparable to the emission wavelength (525 nm) of fluorescent particles. With light microscopic images, however, only the bigger particles could be observed, exactly at the same locations of bigger sized particles in the fluorescence microscopic images. As the particle size (0.5  $\mu$ m) is smaller than the upper limit of visible wavelength (400-750 nm), it will be difficult to image the 0.5- $\mu$ m, non-aggregated particles, while the aggregated particles (> 0.8  $\mu$ m) can be imaged relatively easily.

**Norovirus capsids in DI water**  
**Benchtop microscope assay**

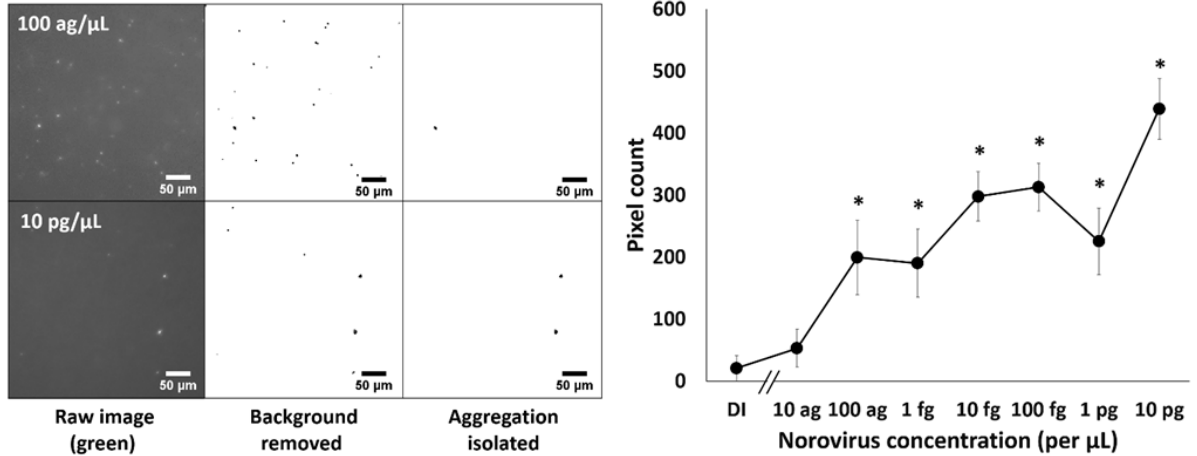


Figure A-2. Benchtop microscope assay results for norovirus capsids. For each assay, 4 different areas of a single channel were imaged and analyzed to obtain the pixel counts of aggregated particles. The pixel counts from 4 different images were added together to yield a single data point. Only green channel images were used. Experiments were repeated 3 times (0 – 1 fg/μL) or 4 times (10 fg/μL – 10 pg/μL), each time using a different μPAD. Error bars represent standard errors of such 3 to 4 assays. \* indicates statistically significant difference (p < 0.05 with Wilcoxon rank sum test) from a negative control sample. Left: representative raw, background-removed, and non-aggregated particles-removed images (captured by a benchtop fluorescence microscope and processed with ImageJ) of a μPAD at given norovirus capsid concentrations. These images are zoomed-in versions (400 μm x 400 μm) to clearly show the particles; the actual images used in the assays are 1.060 mm wide and 0.792 mm long. Right: average pixel counts from μPAD are plotted against norovirus capsid concentrations, using a benchtop fluorescence microscope and ImageJ processing.

The averages and standard errors of these pixel counts from 3-4 independent assays were plotted against the norovirus concentration in Figure A-2 to the right. As sample size is relatively small, it was difficult to assume normal distribution for each data point. Therefore, the nonparametric Wilcoxon rank sum test was conducted for each data point in comparison to the zero-concentration data point (in DI water) as a negative control. The lowest concentration of norovirus capsid that passed the Wilcoxon rank sum test ( $p < 0.05$ ) was 100 ag/ $\mu$ L, which is the LOD of this assay. All concentrations from 100 ag/ $\mu$ L to 10 pg/ $\mu$ L were also significantly different from the zero concentration (negative control), indicating the particle aggregation was highly correlated to the norovirus presence and minimum non-specific aggregation. This LOD is several orders of magnitude lower than 0.25-12.5 pg/ $\mu$ L (= ng/mL) with the commercial lateral flow assays (including immunoCatch-Noro from Eiken Chemical, GE test Noro Nissui from Nissui Pharmaceutical, and Quick Navi-Noro 2 from Denka Seiken) and 10-100 fg/ $\mu$ L as reported in the recent literature utilizing nanostructures as well as laboratory equipment such as a microplate reader<sup>24</sup> or surface plasmon resonance equipment.<sup>25</sup> Since the weight of a single norovirus particle is approximately 10 ag considering its diameter (35-40 nm),<sup>13</sup> this LOD value is close to a single virus particle level within an order of magnitude.

**Specificity Test.** To evaluate the specificity of this assay, Zika virus was assayed using anti-norovirus conjugated particles and compared with the results of norovirus assay. Experimental conditions were identical to those of norovirus assays. As shown in Figure A-3, the pixel counts were much smaller with Zika virus than with norovirus. All Zika virus concentrations were not significantly different from the zero concentration (negative control) using the nonparametric Wilcoxon rank sum test. Taken together these results,

satisfactory specificity was achieved by the assay at least for the given experimental conditions.

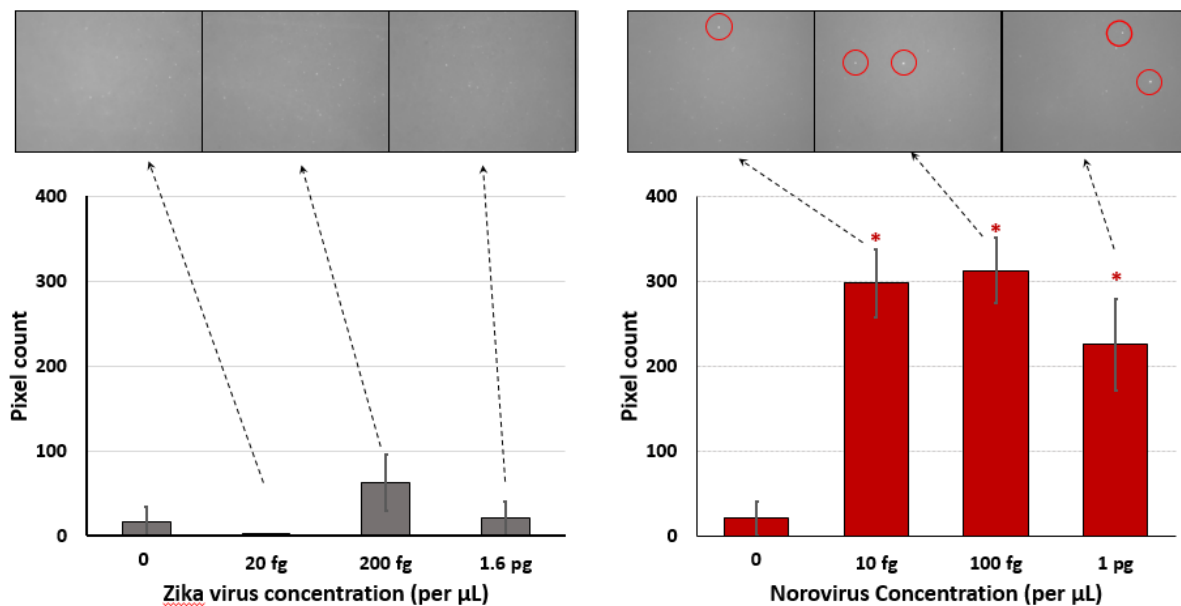


Figure A-3. Specificity test. Three different concentrations of Zika virus and norovirus were tested with anti-norovirus conjugated particles. Benchtop microscope assays and ImageJ analyses were used. Other experimental conditions are identical to those shown in

Figure A-2.

**Smartphone Microscope Assays.** Next, the same experiments were repeated while replacing norovirus capsids with intact noroviruses (refer to the Methods section for the preparation of intact norovirus and RT-qPCR assay). The  $\mu\text{PAD}$  assays were conducted for assessing intact norovirus using a smartphone microscope shown in Figure A-1b and MATLAB Mobile GUI app (Figure A-S2). Intact noroviruses were initially diluted in deionized (DI) water. Again, all serial dilutions were made in 1 mL volume and vortex-mixed to ensure that there were sufficient amounts of norovirus even at the lowest

concentration (1,000 genome copies in 1 copy/ $\mu$ L sample). Since the smartphone constantly attempts to compensate for lighting bias and exposure, and to adjust white balance, the overall brightness of raw images was different from assay to assay. Therefore, the raw images (already square-cropped circumscribing circular field of view) were processed to eliminate the pixels with the intensities smaller than the overall mean + 50 (out of 255; to remove background noise), binarized, and further processed to eliminate the pixel areas smaller than 30 (to remove non-aggregated particles). Refer to the Methods section for details. Similar to the benchtop microscope assays, 4 different areas of a single channel were imaged and analyzed, and the pixel counts were added together to yield a single data point. Experiments are repeated 3 times, each time using a different  $\mu$ PAD. The results are depicted in Figure A-4, showing the representative, zoomed-in images (raw, background removed, and aggregation isolated) for 1 copy/ $\mu$ L (the lowest concentration assayed) and 1000 copies/ $\mu$ L (the highest concentration significantly different from the negative control, i.e., virus-free deionized water) to the left, and the plot of average pixel counts against the norovirus concentration (genome copies per  $\mu$ L) to the right. All final processed images without zoom-in were summarized in Figure A-S3. The lowest concentration that is significantly different ( $p < 0.05$  with Wilcoxon rank sum test) from the control (virus-free DI water) is 1 copy/ $\mu$ L, the LOD of this assay. It corresponds to 10 ag/ $\mu$ L considering the size of a norovirus particle, 35-40 nm,<sup>13</sup> and is one order of magnitude lower than that of assaying norovirus capsids, 100 ag/ $\mu$ L. This can be attributed to the fact that the norovirus capsids were recombinant proteins that might have inferior affinity to the anti-norovirus compared to the intact norovirus samples. Concentrations of 10 and 100 copies/ $\mu$ L are also significantly different from the control ( $p < 0.05$ ). The

average pixel counts at the highest concentration, 1000 copies/ $\mu\text{L}$ , is slightly smaller than that of 100 copies/ $\mu\text{L}$ , indicating that this concentration is outside the linear range of assay. In other words, there were too many virus particles that “consumed” all antibodies, which subsequently failed to connect antibody-conjugated particles together. Despite this, it is still substantially higher than the negative control ( $p < 0.05$ ).

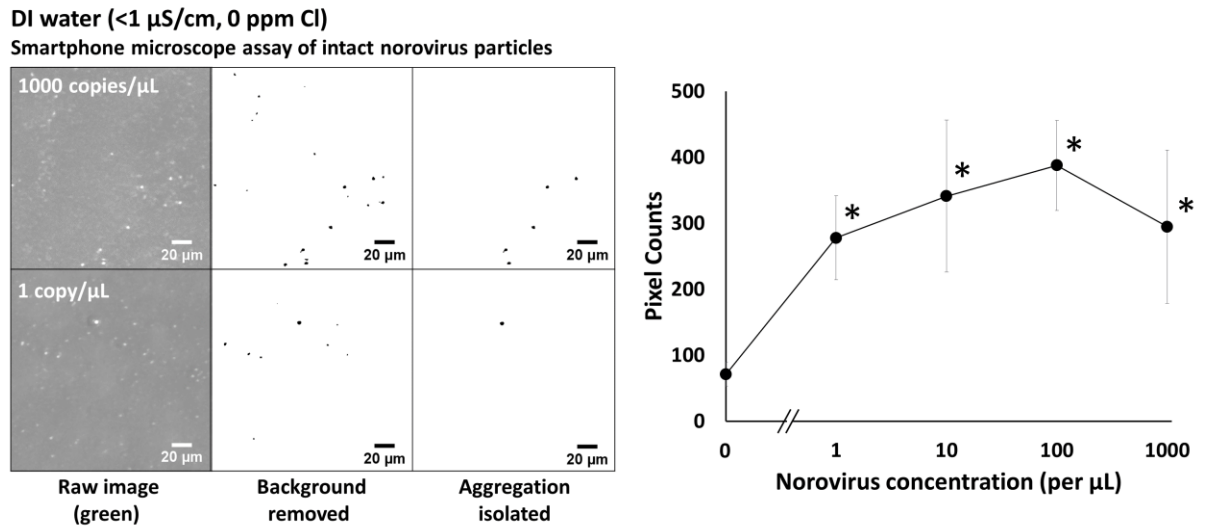


Figure A-4. Smartphone assay results for intact norovirus in DI water. For each assay, 4 different areas of a single channel were imaged and analyzed to obtain the pixel counts of aggregated particles. The pixel counts from 4 different images were added together to yield a single data point. Both green and red channels were combined to maximize pixel intensities. Experiments were repeated 3 times, each time using a different  $\mu\text{PAD}$ . Error bars represent standard errors of such 3 assays. Wilcoxon rank sum test was performed and \* indicates statistically significant difference ( $p < 0.05$ ) from a negative control sample. Left: representative raw and processed images of  $\mu\text{PAD}$  at given intact norovirus concentrations. These images are zoomed-in versions ( $196 \mu\text{m} \times 196 \mu\text{m}$ ) to clearly show

the particles. Right: Average pixel counts from  $\mu$ PAD are plotted against intact norovirus concentrations, using a smartphone-based fluorescent microscope and a MATLAB code.

To further confirm this extremely low LOD of 1 copy/ $\mu$ L, the number of aggregated particle clusters (not the pixel counts) in four different images (from a single  $\mu$ PAD channel) was totaled together. The total average from the three different assays was  $6 \pm 1$ . The volume of loaded sample of 5  $\mu$ L, corresponding to 1 copy/ $\mu$ L  $\times$  5  $\mu$ L = 5 copies, is comparable to the above count of particle clusters. It should be noted that a portion of such clusters may not represent “true” aggregation caused by antibody-antigen binding but rather non-specific aggregation. The result shown in Figure A-4 further corroborate this fact, as the pixel counts with zero concentration is  $\sim 80$ , representing a small extent of non-specific aggregation, while those with 1 copy/ $\mu$ L is  $\sim 280$ . In addition, the genome copy number (evaluated by RT-qPCR) does not truly represent the number of “all” virus particles, which can be higher. It is also possible that the sample contained free antigens and fragments in addition to intact viruses, which could also enable particle immunoagglutination.

**Smartphone Microscope Assays with Field Water Samples.** We then proceeded to further evaluate this method for two different field water samples: intact noroviruses were spiked into tap water and reclaimed wastewater. Water samples were serially diluted using the same tap water or reclaimed wastewater, thus the sample matrices were undiluted. As described in the Methods section, the raw images were processed to remove background noise using the cut-off intensities of the overall mean + 40, + 45 or + 50. These images were then binarized, and further processed to remove non-aggregated particles (isolating

only the aggregated particles) using the cut-off pixel areas of 30. The cut-off intensities (mean + 40, + 45, or +50) were selected that minimized the presence of background noise, represented by single pixels not clustered together. Particles were always represented by clusters of pixels. Experiments were repeated 6 times with both tap water and reclaimed wastewater, each time using a different  $\mu$ PAD.

The assay results with tap water are depicted in Figure A-5. No data points passed the Wilcoxon rank sum test ( $p > 0.05$ ), while the p value was the smallest (0.063) with the highest concentration of 1000 copies/ $\mu$ L. While the overall pixel counts generally increased from the negative control, they were not significantly different. Additionally, the pixel counts are also lower (80 – 160) than those with DI water (270 – 390). These results can be attributed to electrolytes common in tap water (its conductivity was  $920 \pm 10 \mu\text{S/cm}$ ) or its high chlorine content ( $0.5 \pm 0.1 \text{ ppm}$ ).

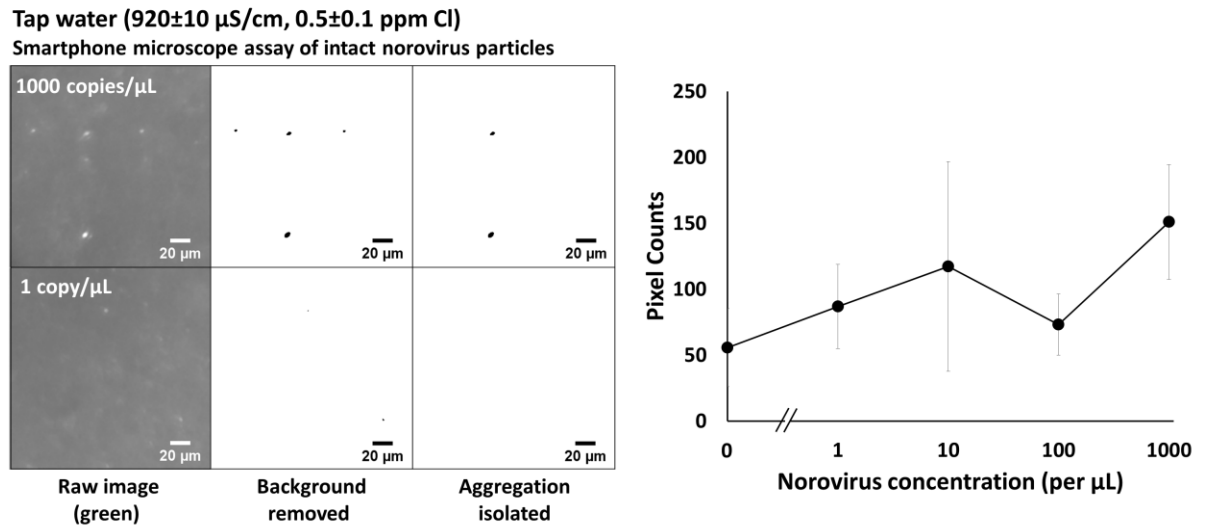


Figure A-5. Smartphone assay results for tap water. Other experimental conditions are identical to those shown in Figure 3, except that the assays were repeated 6 times.

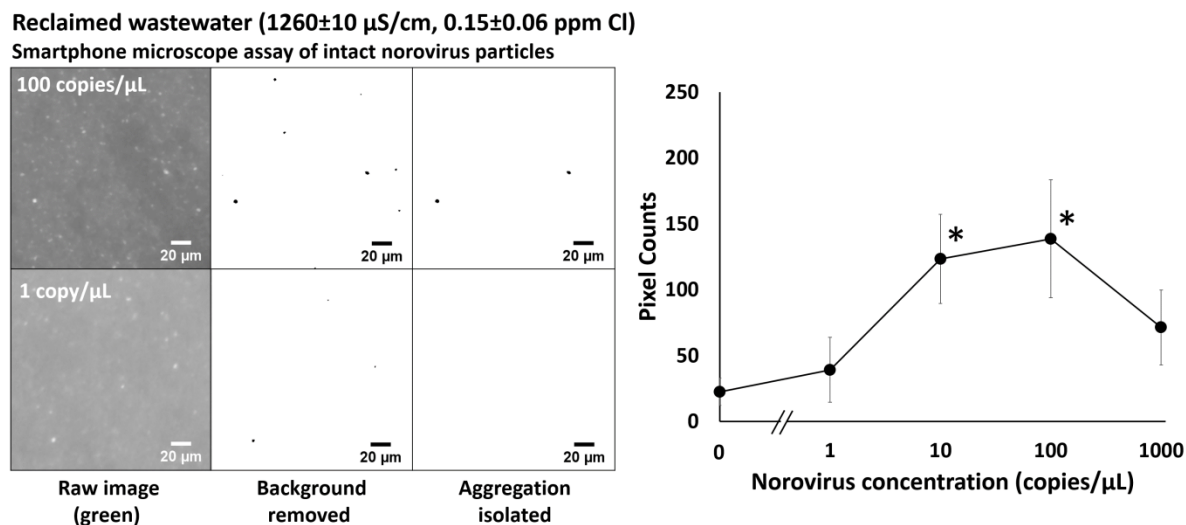


Figure A-6. Smartphone assay results for reclaimed wastewater. Other experimental conditions are identical to those shown in Figure 3, except that the assays were repeated 6 times.

Identical experiments were repeated with reclaimed wastewater. The assay results with reclaimed wastewater are shown in Figure A-6. While the pixel counts (40 – 140) are still lower than those with DI water (270 – 390) and comparable to those of tap water (40 – 140), the lowest concentration that was significantly different (with Wilcoxon rank sum test) from the negative control (unspiked reclaimed wastewater) is 10 copies/μL (corresponding to 100 ag/μL), again close to the single virus copy level. The overall curve also resembles the one with DI water, i.e., an increase up to 100 copies/μL followed by a decrease at 1000 copies/μL. The conductivity of reclaimed wastewater was  $1260 \pm 10 \mu\text{S/cm}$ , which was even higher than that  $920 \pm 10 \mu\text{S/cm}$  of tap water, while its chlorine content was  $0.15 \pm 0.06 \text{ ppm}$ , significantly lower than that  $0.5 \pm 0.1 \text{ ppm}$  of tap water. To confirm the effect of chlorine to our assay, a control experiment was performed by adding

0.5 ppm and 5 ppm chlorine to DI water, and the results are shown in Figure A-S4. Compared to the DI water results (Figure A-4), the error bars were larger and comparable to those with the tap water results (Figure A-5). With 0.5 ppm chlorine, a very narrow linear response up to 10 copies/ $\mu\text{L}$  was observed followed by premature saturation. Such narrow linearity could not be found with 5 ppm chlorine, one order of magnitude higher concentration than that of tap water. Thus, chlorine could be responsible for rendering the assay results less reproducible, although the role of electrolytes in tap water could not be ruled out entirely. In addition, chlorine might have adversely affected the availability of antibody-conjugated particles. (Chlorines can easily be removed by simply letting them to evaporate from water samples.)

The excellent LODs in DI water and reclaimed wastewater can be attributed to many factors. Most importantly, we developed an image processing algorithm that isolated only the immunoagglutinated particles and counted the total number of such pixels. While a large number of fluorescent dyes and/or nanoparticles were necessary to collect sufficiently strong signals in other optical detection methods, only a small number of particles were necessary for individual counting. It also contributed to minimizing non-specific aggregation and facilitating capillary action-driven washing. In addition, most immunoagglutinated particles were retained and quantified in the field of view through direct imaging and counting on a paper substrate, enabling single virus copy level detection.

### 3. Conclusion

To summarize, we demonstrated an easy-to-use, low-cost, and extremely sensitive assay for detecting waterborne virus pathogens that does not require concentration, in vitro cell culture, and/or nucleic acid amplification. A microfluidic paper analytic device ( $\mu$ PAD) was fabricated via wax printing, and noroviruses were captured directly on a  $\mu$ PAD. Antibody-conjugated submicron particles were then loaded to a  $\mu$ PAD and resulting particle aggregation was imaged directly on a  $\mu$ PAD surface. An image analysis algorithm was developed to isolate only the aggregated particles while removing the background, generating visually convincing assay results that were not affected by lighting biases and perturbations. Benchtop fluorescence microscope and subsequent ImageJ analysis were initially performed to identify and quantify norovirus capsids in DI water. Smartphone-based fluorescence microscope and original MATLAB Mobile GUI app were then used to quantify intact norovirus samples in various field water samples. The LODs with smartphone assays were 1 copy/ $\mu$ L in DI water and 10 copies/ $\mu$ L in reclaimed wastewater, at single virus particle level. Due to these extremely low LODs, virus concentration or nucleic acid amplification steps were not necessary. The results with tap water were inferior, presumably due to its high chlorine content. This can be easily resolved by simply letting chlorine to evaporate from water samples. Additionally, a separate “control” channel is not necessary, which is typically required for other optical microfluidic biosensing. This method with extremely low LOD can also be applied for detection of any other viral pathogens in environmental samples such as food, water and fomites.

## 4. Methods

**$\mu$ PAD Fabrication.** A ColorQube wax printer (Xerox Corporation; Norwalk, CT, USA) was used to print the microfluidic design (Figure A-1a) onto a nitrocellulose paper (Hi-Flow<sup>TM</sup> Plus Membrane, catalog number HF07502XSS; Millipore; Billerica, MA, USA). Each chip has four wax-printed channels (21 mm long and 2.4 mm wide). Each chip was heated on a hot plate (Corning; Corning, NY, USA) at 120°C until the surface-printed wax was melted to fill the paper pores underneath.

**Antibody Conjugation to Fluorescent Particles.** Rabbit polyclonal antibody to norovirus capsid protein VP1 (anti-norovirus, catalog number ab92976; Abcam, Inc.; Cambridge, MA, USA) was used for assaying both norovirus capsids and intact noroviruses. Anti-norovirus was covalently conjugated to carboxylated, yellow-green fluorescent, polystyrene particles (particle diameter = 0.5  $\mu$ m; Magsphere, Inc.; Pasadena, CA, USA). The fluorescent characteristics of these particles were reported by the manufacturer: maximum excitation at 480 nm (blue) and maximum emission at 525 nm (green). Prior to antibody conjugation, particles were pre-washed with deionized (DI) water to remove surfactants from the stock solution, through centrifuging at 9.9 g for 13 minutes. The antibody was then conjugated to these fluorescent particles following a protocol described in detail elsewhere.<sup>20</sup>

**Norovirus Sample Preparation.** Initially, recombinant norovirus group-1 capsid (MyBiosource, Inc.; San Diego, CA, USA) was used as a target. Norovirus capsids were serially diluted in DI water from the 1 ng/ $\mu$ L stock solution to make 10 pg/ $\mu$ L, 1 pg/ $\mu$ L, 100 fg/ $\mu$ L, 10 fg/ $\mu$ L, 1 fg/ $\mu$ L, 100 ag/ $\mu$ L, 10 ag/ $\mu$ L, and 1 ag/ $\mu$ L, all in 1 mL volume at 1:10 dilution each (4-10 serial dilutions). The systematic errors of pipettes were  $\pm 0.8\%$  for

a 1,000  $\mu\text{L}$  pipette and  $\pm 0.6\%$  for a 100  $\mu\text{L}$  pipette, resulting in the propagated errors of 2.0%-3.1% for the given range of dilutions. These errors were too small to be represented as the horizontal error bars in the logarithmic scale x-axes in all plots.

Intact norovirus samples were collected from toilet fecal samples during an active norovirus outbreak. These samples were confirmed and quantified by quantitative reverse transcription polymerase chain reaction (RT-qPCR). Fecal samples were suspended in sterile phosphate buffered saline (PBS) solution (pH 7.4) at 10% w/v. These fecal suspensions were centrifuged at 1,455 g for 10 minutes using Centriprep centrifugal filters (50 kDa cutoff; EMD Millipore, Burlington, MA, USA) to purify virus particles. The retentates ( $\sim 0.75$  mL) were divided into aliquots of 200  $\mu\text{L}$  and frozen or subjected to nucleic acid extraction. To confirm and quantify norovirus, virus nucleic acids were extracted using the QIAmp viral RNA extraction kit (Qiagen, Chatsworth, CA, USA) and RT-qPCR assays were performed for three different genogroups of norovirus (GI, GII, and GIV) following previously reported assays.<sup>21-23</sup> GII norovirus RNA was predominantly detected from the fecal suspensions, with a viral load of approximately  $10^7$  virus targets per mL of stool supernatant. These fecal suspensions were serially diluted in various water samples (described in the following section) from the 10000 genome copies/ $\mu\text{L}$  to obtain 1000 genome copies/ $\mu\text{L}$ , 100 copies/ $\mu\text{L}$ , 10 copies/ $\mu\text{L}$ , and 1 copy/ $\mu\text{L}$ , again all in 1 mL volume at 1:10 dilution each (1-4 serial dilutions). Using the same systematic errors of pipettes, the propagated errors were 1.0%-2.0% for the given range of dilutions. Again, these errors were too small to be represented as the horizontal error bars in the logarithmic scale x-axes in all plots.

**Specificity Test.** Zika virus (attenuated virus particles; NATrol Zika Virus Range Verification Panel; ZeptoMetrix Corporation, Buffalo, NY, USA) was used to evaluate the cross-reactivity of anti-norovirus with this assay. Both norovirus and Zika virus are single-stranded RNA viruses, have globular shapes, and are similar in size. Identical experiments were performed by substituting norovirus samples with Zika virus samples. The concentrations of Zika virus samples were 1.6 pg/ $\mu$ L, 200 fg/ $\mu$ L, and 20 fg/ $\mu$ L.

**Water Samples.** Various types of environmental water samples, spiked with known concentrations of norovirus, were tested in this work: deionized (DI) water, drinking tap water, and reclaimed wastewater. The latter was produced in a facility utilizing primary sedimentation dissolved air flotation, four parallel five-stage Bardenpho processes, disk filtration, and chlorination. These water samples were tested for pH, conductivity, and chlorine residual. pH was measured using the pH electrode and pH monitor (Pinpoint American Marine Inc.; Ridgefield, CT, USA). Conductivity was measured using the UltraPen PT1 (Myron L Company; Carlsbad, CA, USA). Free chlorine residual was assayed by the EPA-accepted Thermo Orion Method AC4P72 (using N, N-diethyl-p-phenylenediamine, thus known as DPD method; Thermo Fisher, Waltham, MA, USA) by measuring absorbance at 520 nm using a miniature spectrophotometer (USB4000, Ocean Optics, Inc.; Dunedin, FL, USA).

**Assay Procedure.** Norovirus suspensions (5  $\mu$ L) from spiked environmental water samples were pipetted directly to the center of each  $\mu$ PAD channel made out of nitrocellulose paper, without using any pre-treatments. This norovirus suspension spread through each microfluidic channel, where norovirus particles were captured onto nitrocellulose paper (polarity filter) via electrostatic interactions. After loading norovirus,

2  $\mu\text{L}$  of anti-norovirus conjugated fluorescent polystyrene particle suspension (0.001% w/v for DI water and 0.002% w/v tap water and reclaimed wastewater) were loaded onto the center of each channel on the  $\mu\text{PAD}$  where noroviruses were captured (Figure A-1a). Anti-norovirus conjugated particles flowed through and filled the entire channel by capillary action (or wicking). These particles were aggregated by antibody-antigen binding, i.e., immunoagglutination, which were imaged as described in the following section.

**Imaging Particle Aggregation on  $\mu\text{PADs}$  Using a Benchtop Fluorescence Microscope.** Particle aggregation with norovirus was imaged by taking 4 random images of each channel with a 5-second exposure time, initially using a benchtop fluorescence microscope (Eclipse TS 100; Nikon Corp.; Tokyo, Japan), equipped with a fluorescence filter (AG Heinze B-2E/C; A.G. Heinze, Inc.; Lake Forest, CA, USA) and an imaging software (NIS Elements; Nikon Corp.; Tokyo, Japan). Only green channel images were used. From the processed images, the pixel counts were evaluated, which were added together for 4 different images to yield a single data point. This procedure was repeated 3-4 times, each time using a different  $\mu\text{PAD}$ .

**Imaging Particle Aggregation on  $\mu\text{PADs}$  Using a Smartphone-based Fluorescence Microscope.** The smartphone-based fluorescence microscope (Figure A-1b) consisted of an external microscope (XFox Professional 300X Optical Glass Lenses; X&Y Ind., Shenzhen, China) with magnification  $200\times - 300\times$ , attached to a smartphone (iPhone 7; Apple, Inc.; Cupertino, CA, USA). A blue excitation light source was provided by a secondary smartphone flashlight with a  $480 \pm 10$  nm bandpass filter (catalog number 43-115; Edmund Optics, Barrington, NJ, USA). This can be easily replaced by any blue LED. An unmounted  $525 \pm 20$  nm bandpass filter (catalog number BP525-D25; Midwest Optical

Systems, Inc.; Palatine, IL, USA) was placed in between the  $\mu$ PAD and the objective lens of a microscope to capture green fluorescence emission. All images were taken using the ProCam4 app (Samer Azzam, <http://www.procamapp.com>; downloaded via iTunes), where the exposure time and white balance could be manually adjusted. Light trail exposure time was 4 seconds, white balance was 4000, and ISO was 200. Similar to benchtop fluorescence microscopy, 4 images were taken from each channel to yield a single data point. Experiments were repeated 3-6 times, each time using a different  $\mu$ PAD.

**Image Analysis for Benchtop Fluorescence Microscopic Images.** ImageJ (U.S. National Institutes of Health; Bethesda, MD, USA) was initially processed on a separate desktop computer to analyze the images taken on a benchtop fluorescence microscope. For benchtop fluorescence microscopic images, ‘Find Edges’ option in ImageJ was utilized to outline the image of particles. All pixels with intensity values  $< 100$  (out of 255 for green emission) were considered background noise and eliminated. This threshold value (100) was determined by comparing the images with those measured by a higher magnification fluorescence microscope. All other pixels with intensity values  $\geq 100$  were selected, the interior of the edges were filled, and these selected pixels were binarized. This procedure resulted in binary images of the particles. Once the images were binarized, ‘Analyze Particles’ function was selected in ImageJ, and the pixel area was obtained. The pixel area  $< 50$  was eliminated since they were single particles that were not aggregated by norovirus. This threshold value (50) was determined by comparing the images to those measured by a higher magnification fluorescence microscope. The final data consisted of the following: 1) the number of aggregated particle clusters, and 2) the total accumulated pixel counts of

all aggregated particles, for the given image. This procedure is schematically illustrated in Figure A-7.

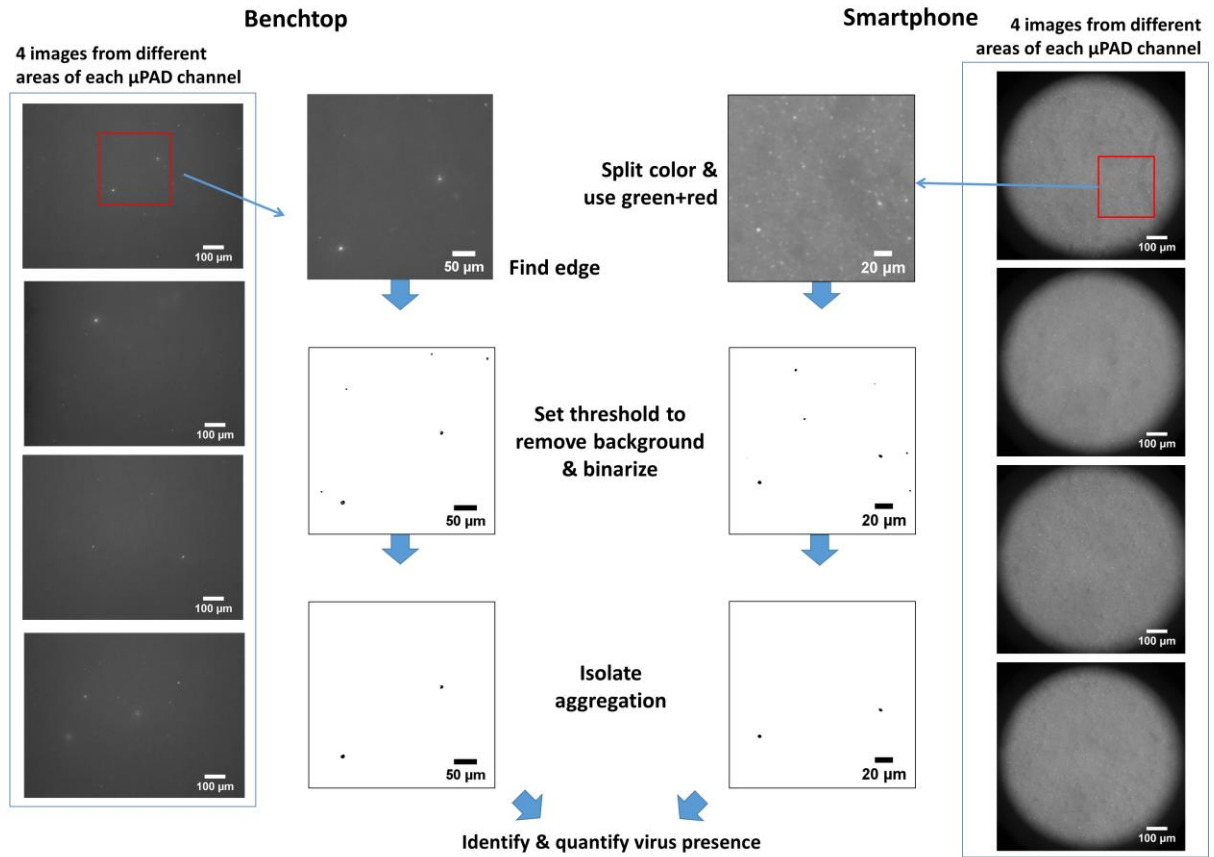


Figure A-7. Image processing algorithm using ImageJ for benchtop fluorescence microscopic images (left) and MATLAB GUI code for smartphone fluorescence microscopic images (right). Using the pre-determined cut-off pixel intensity (to remove background) and pixel area (to isolate aggregated particles), along with binarization, a processed image is generated showing only the aggregated particles. The total pixel counts are added altogether from 4 different images from a single μPAD channel, which makes up a single data point. This experiment is repeated 3-6 times, each time using a different μPAD, to evaluate the average pixel counts. Images in the first and last columns

are raw images; those in the second and third columns are zoomed-in versions to clearly show the particles.

**Image Analysis for Smartphone-based Fluorescence Microscopic Images.** All smartphone-based fluorescence microscopic images were split into red, green, and blue channels. While the maximum emission wavelength of the fluorescent particles was 525 nm, their emission is actually ranged over 550 nm, i.e. boundary of green and red colors (hence they are referred as “yellow-green” particles). Therefore, their fluorescence emission could be captured in not only green but also red channels. Since nitrocellulose paper absorbed and scattered light at most wavelengths (its color is bright white) and the maximum exposure time of a smartphone camera was much shorter than that of a benchtop fluorescence microscope, the pixel intensities were quite low. Therefore, both green and red channels were combined to maximize the pixel intensities. Unlike the benchtop fluorescence microscopy, the mean pixel intensities of combined green and red channel images were evaluated using an original code developed in MATLAB version R2017a (The Mathworks, Inc.; Natick, MA, USA). A graphical user interface (GUI) (Figure A-S1) was created and used to automate the analysis procedure and to provide its user-friendliness.

Smartphone microscopic images were processed using a similar algorithm to the benchtop fluorescence microscopy and ImageJ processing. Since the bright field views of smartphone microscopic images were circular in shape, all images were cropped into squares circumscribing those circles, such that all pixels could be utilized for analyses. Aggregated fluorescent particles always exhibited the combined green and red pixel

intensities substantially higher than the overall mean intensities of the cropped area. To eliminate background noise and isolate only the particles, cut-off intensities were applied to the images set at overall mean intensity + 40 to 50. The resulting images were then binarized. To eliminate the non-aggregated particles, those with a pixel area < 30 were eliminated from the binarized images. This cut-off value of a 30 pixel area was smaller than that of benchtop fluorescence microscopy, 50, due to the lower magnification and narrower dynamic range of smartphone-acquired images. This threshold filtering successfully eliminated all ambient light variations, indicating that the method is appropriate for field use. Again, this procedure is schematically illustrated in Figure A-7. The MATLAB GUI generated the accumulated pixel counts of all aggregated particles, for the given image. The MATLAB code and its GUI were adapted to be executed within MATLAB Mobile (The Mathworks, Inc.; Natick, MA, USA), to enable the image analysis performed within a smartphone (Figure A-S2). Once images were acquired, the total assay time was less than one minute including the time for user input.

**Statistical Analysis.** 4 different images were taken from each  $\mu$ PAD channel (Fig. A-1a) and the sum of pixel counts from these 4 images (representing the extent of particle aggregation) were recorded for the given concentration of norovirus. These experiments were repeated 3-6 times for each concentration of norovirus, each time using different  $\mu$ PAD. Averages of these 3-6  $\mu$ PAD assays were recorded. P values for each norovirus concentration against the negative control sample (unspiked) were calculated using Wilcoxon rank sum test, performed with JMP software version 14.3.0 (SAS Institute, Inc.; Cary, NC, USA) with  $\alpha = 0.05$ .

## Associated content

## Supporting Information

The Supporting Information is available free of charge on the ACS Publications website at DOI: 10.1021/acsomega.9b00772.

**Figure A-S1.** Representative raw (left), background-removed (middle), and non-aggregated particles-removed images (right) of a  $\mu$ PAD. Images were captured by a benchtop fluorescence microscope (top) and a benchtop light microscope, both processed with ImageJ.

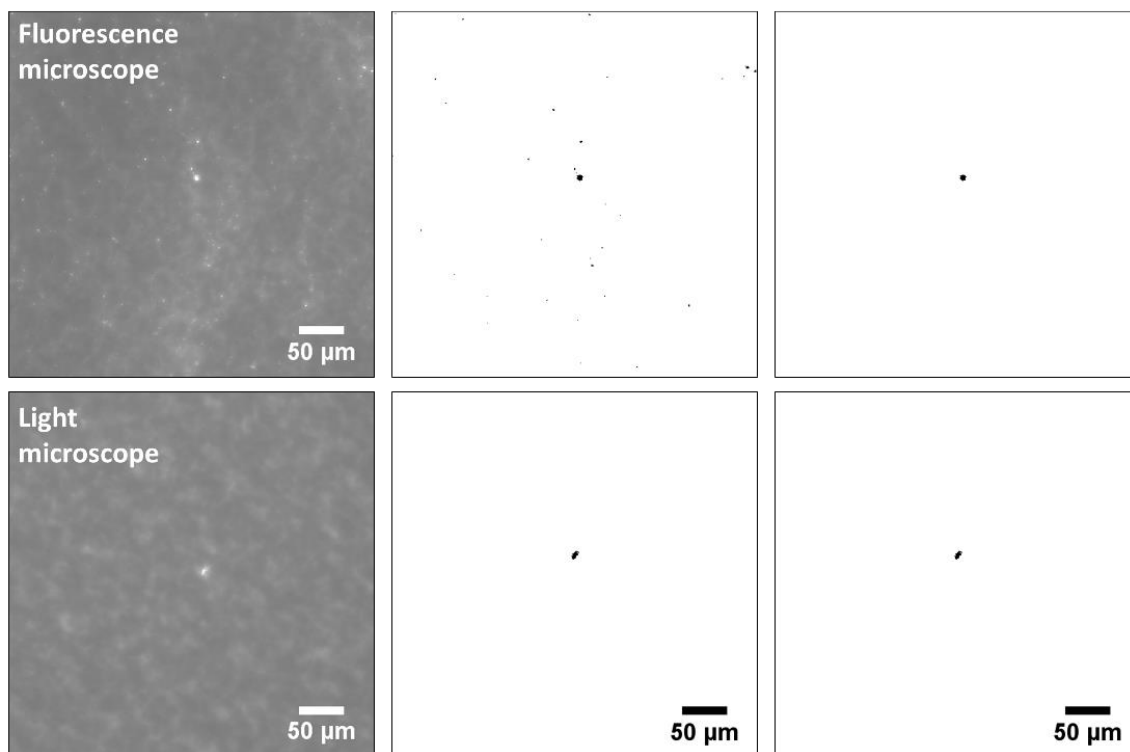


**Figure A-S2.** The user interface of an original, MATLAB GUI app. A raw smartphone image is loaded, and a square crop is applied circumscribing the circular microscopic field of view. Using the pre-determined cut-off pixel intensity and pixel area, along with binarization, a processed image is generated showing only the aggregated particles.

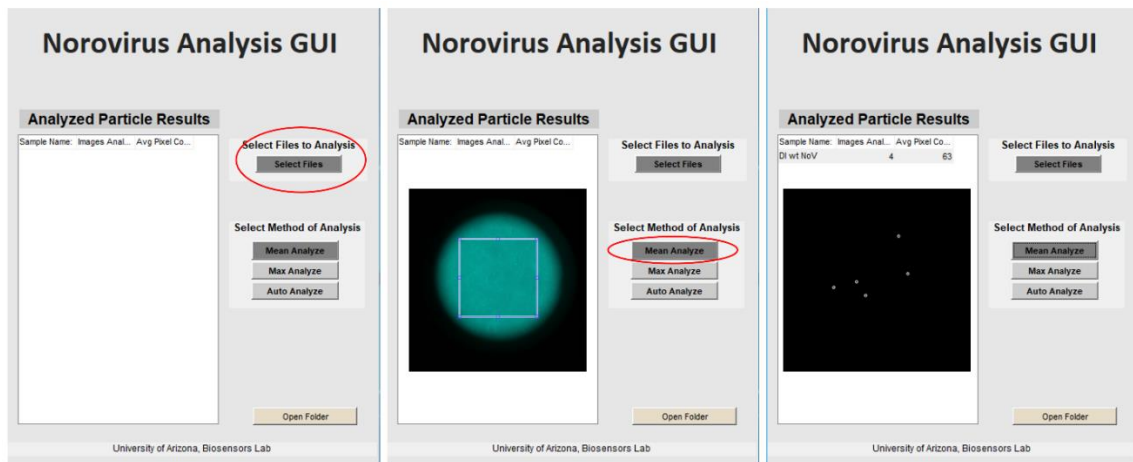
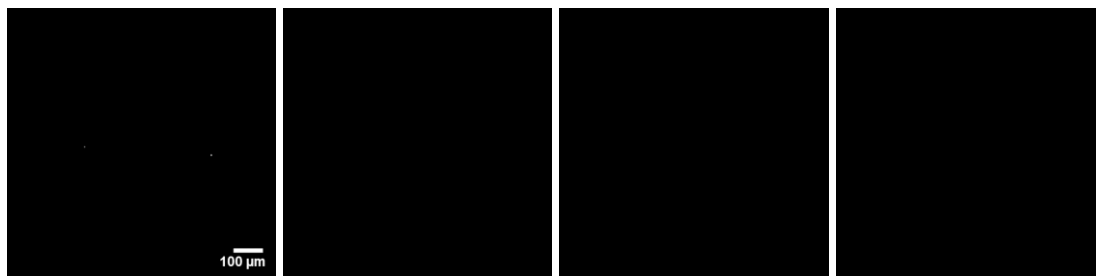
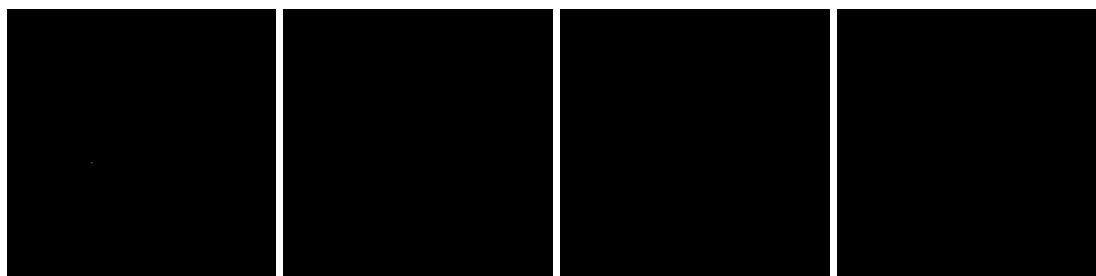


**Figure A-S3.** Processed  $\mu$ PAD channel images using a MATLAB code from smartphone fluorescence microscopic images. Four different areas of a single channel were imaged for each assay. Assays were repeated three to six times, generating 12 to 24 images for each concentration and sample matrix combination.

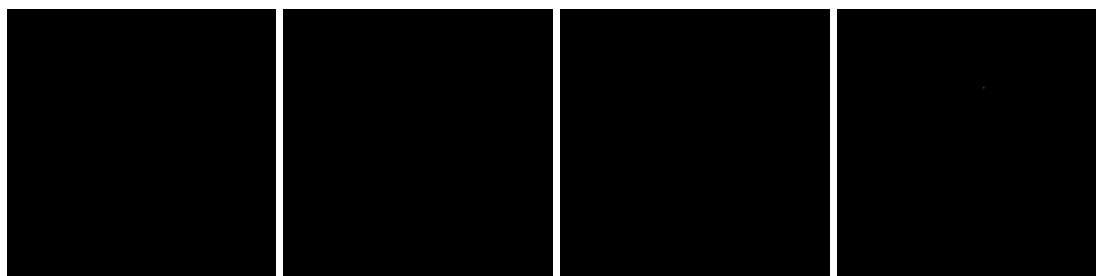
0 copy/ $\mu$ L in DI water assay #1



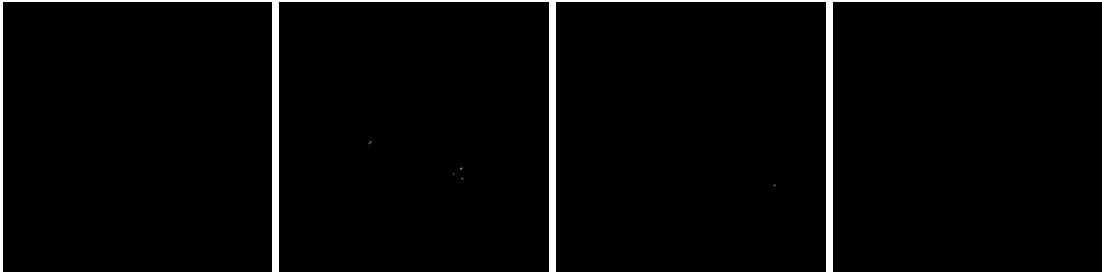
0 copy/ $\mu$ L in DI water assay #2



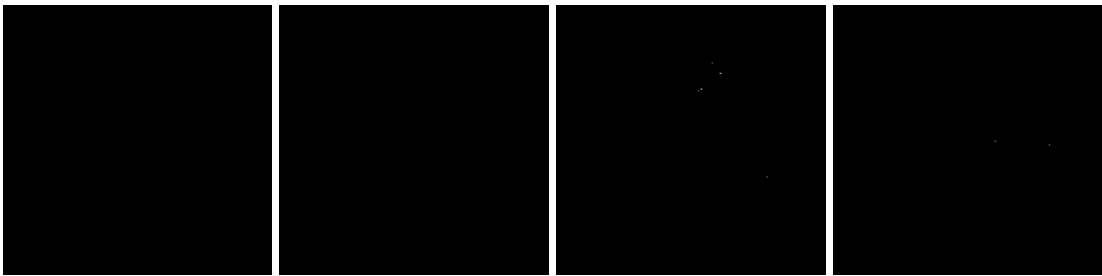
0 copy/ $\mu$ L in DI water assay #3



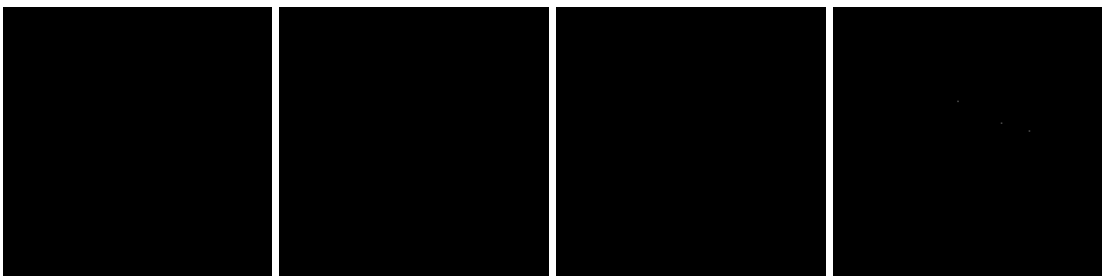
1 copy/ $\mu$ L in DI water assay #1



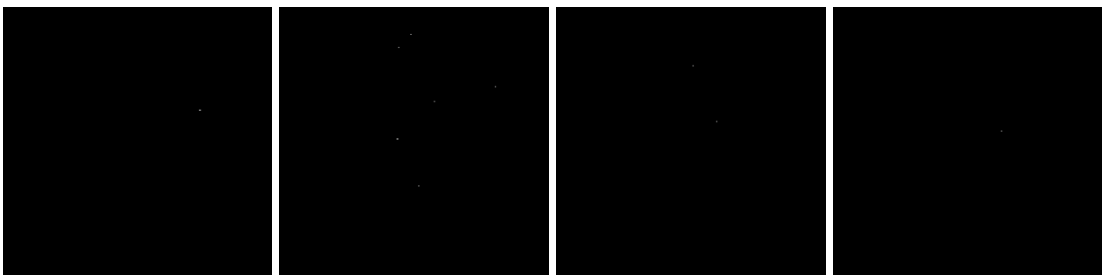
1 copy/ $\mu$ L in DI water assay #2



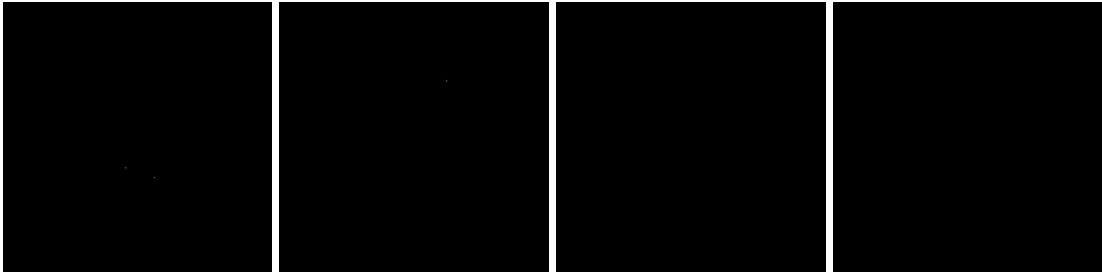
1 copy/ $\mu$ L in DI water assay #3



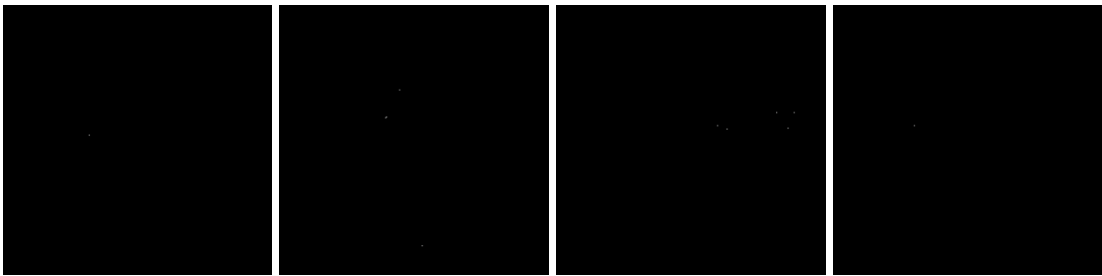
10 copies/ $\mu$ L in DI water assay #1



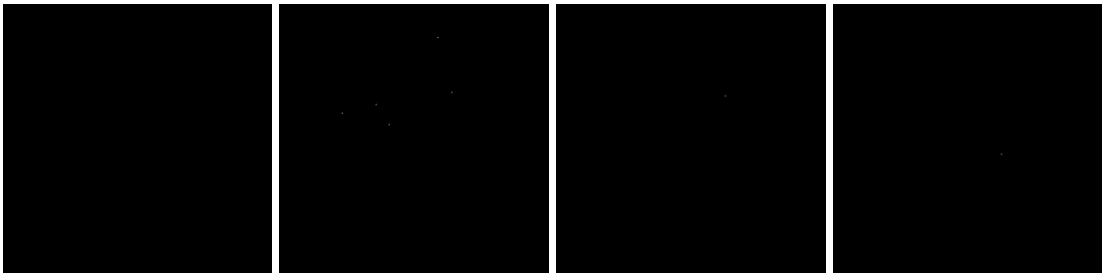
10 copies/ $\mu$ L in DI water assay #2



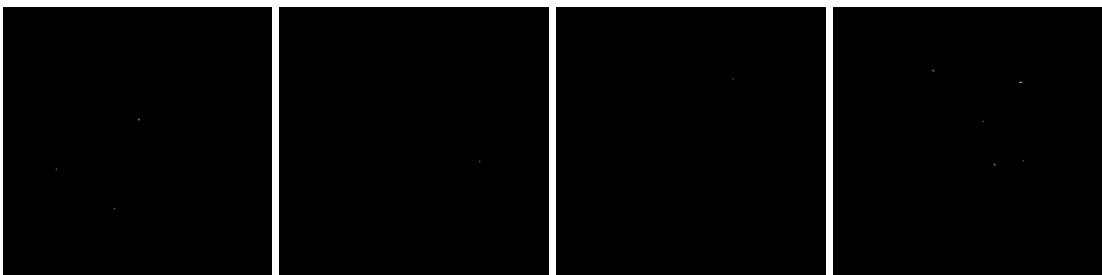
10 copies/ $\mu$ L in DI water assay #3



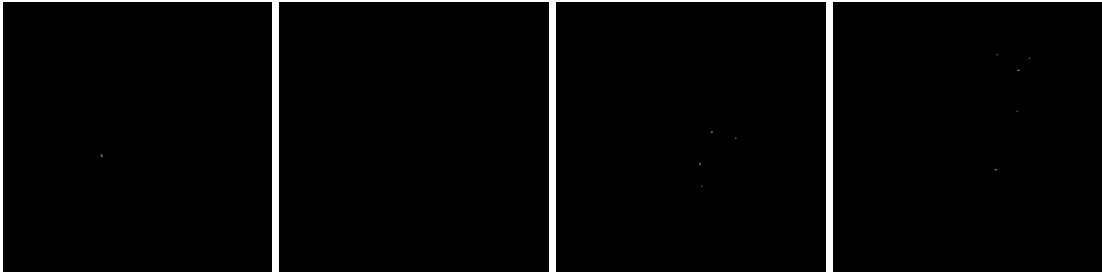
$10^2$  copies/ $\mu$ L in DI water assay #1



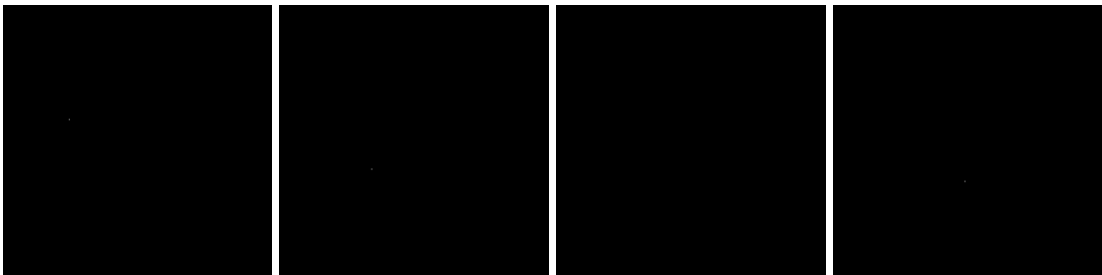
$10^2$  copies/ $\mu$ L in DI water assay #2



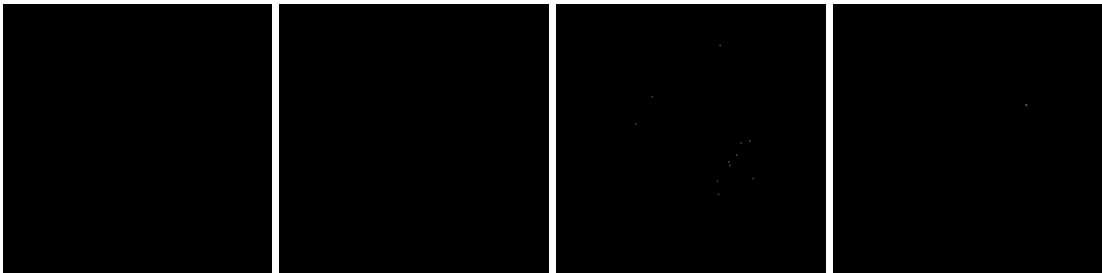
10<sup>2</sup> copies/μL in DI water assay #3



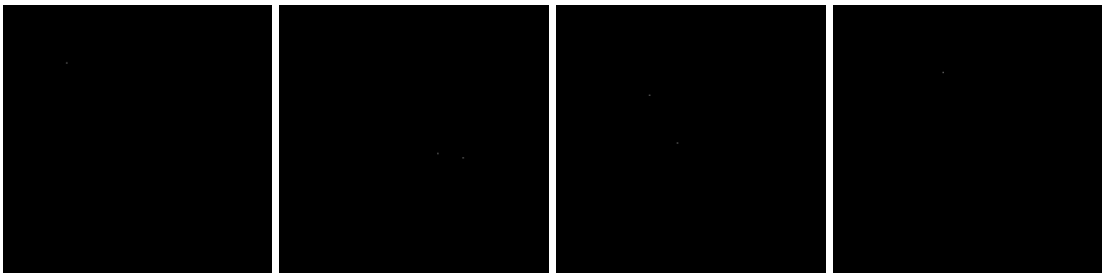
10<sup>3</sup> copies/μL in DI water assay #1



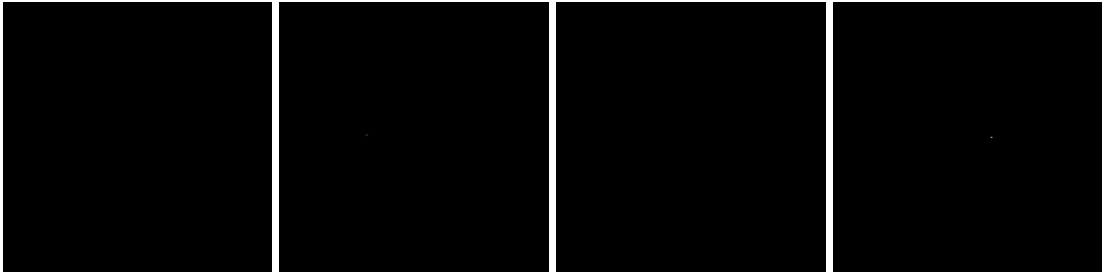
10<sup>3</sup> copies/μL in DI water assay #2



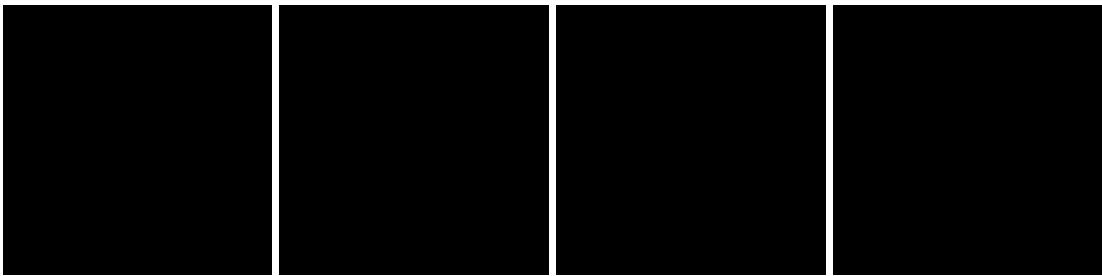
10<sup>3</sup> copies/μL in DI water assay #3



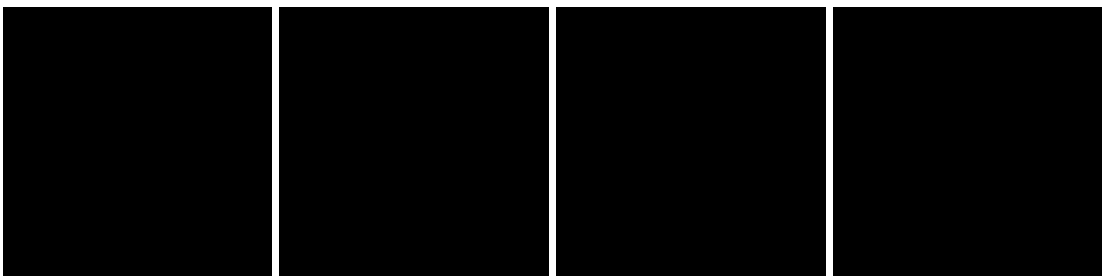
0 copy/ $\mu$ L in tap water assay #1



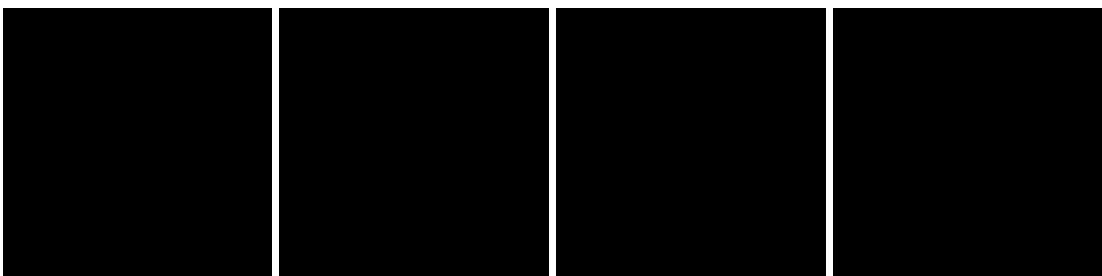
0 copy/ $\mu$ L in tap water assay #2



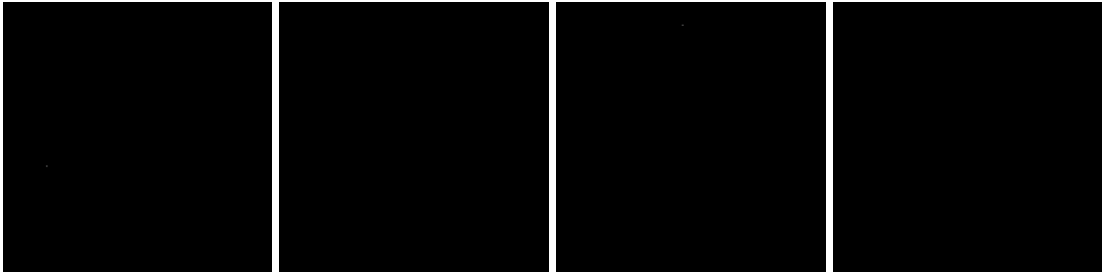
0 copy/ $\mu$ L in tap water assay #3



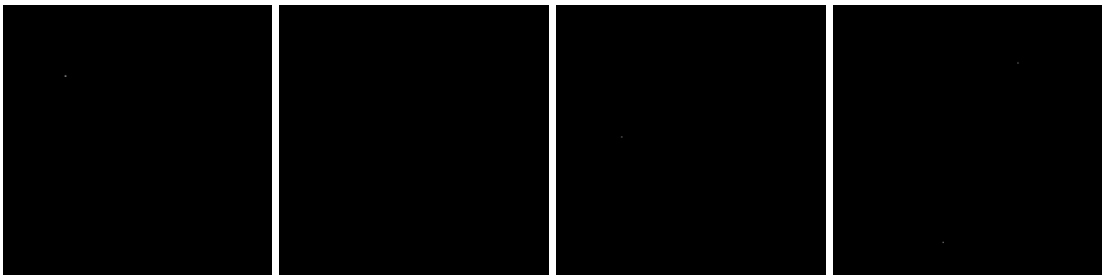
0 copy/ $\mu$ L in tap water assay #4



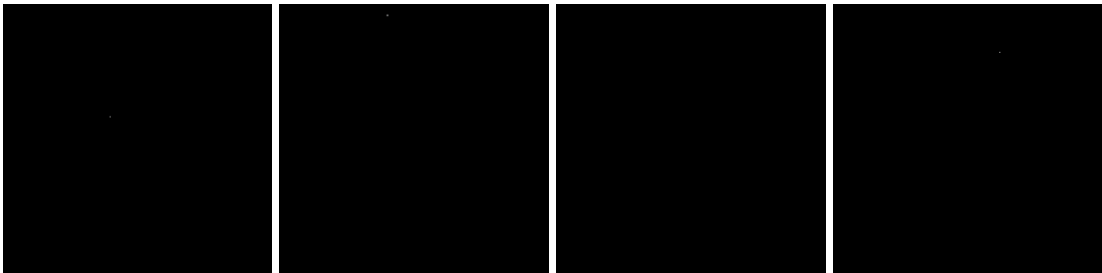
0 copy/ $\mu$ L in tap water assay #5



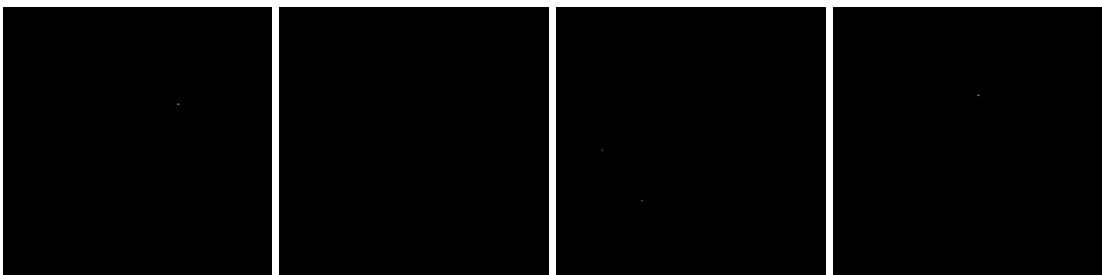
0 copy/ $\mu$ L in tap water assay #6



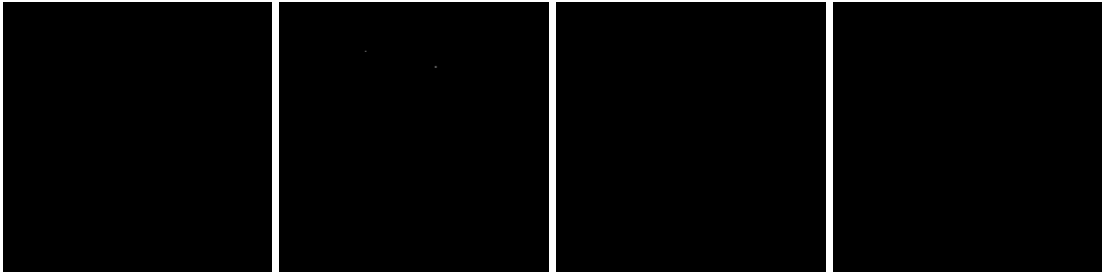
1 copy/ $\mu$ L in tap water assay #1



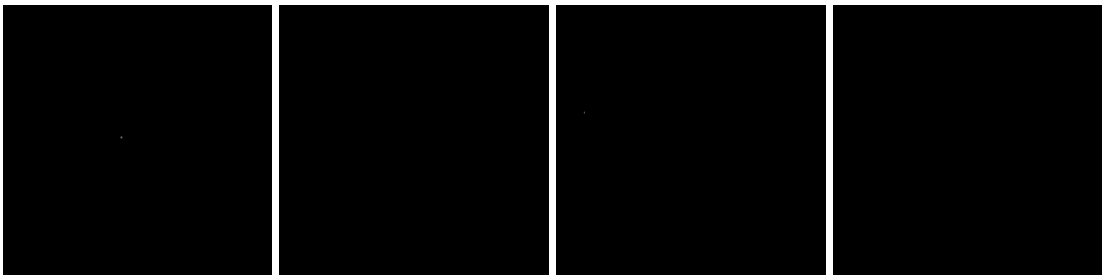
1 copy/ $\mu$ L in tap water assay #2



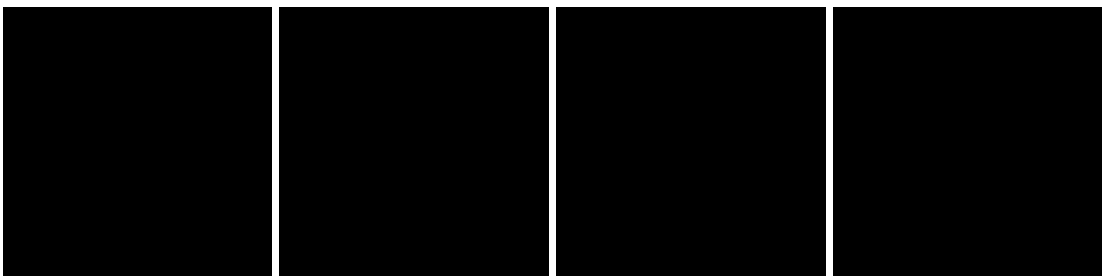
1 copy/ $\mu$ L in tap water assay #3



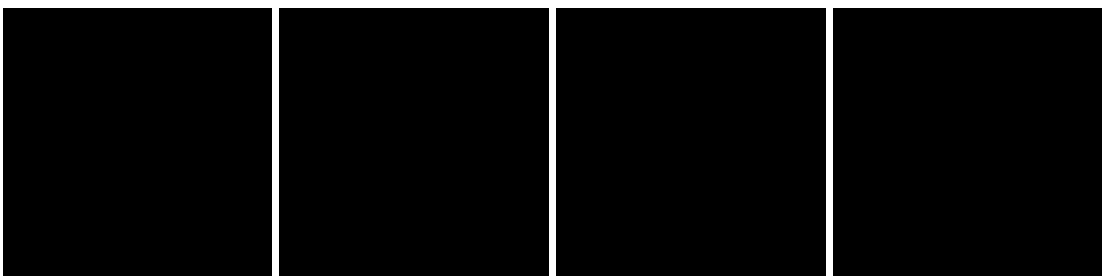
1 copy/ $\mu$ L in tap water assay #4



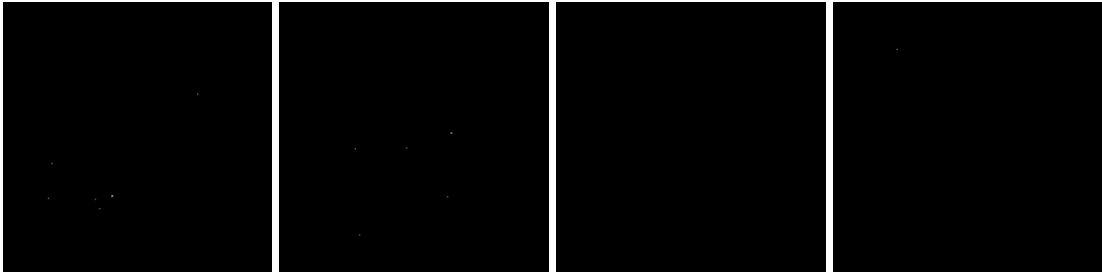
1 copy/ $\mu$ L in tap water assay #5



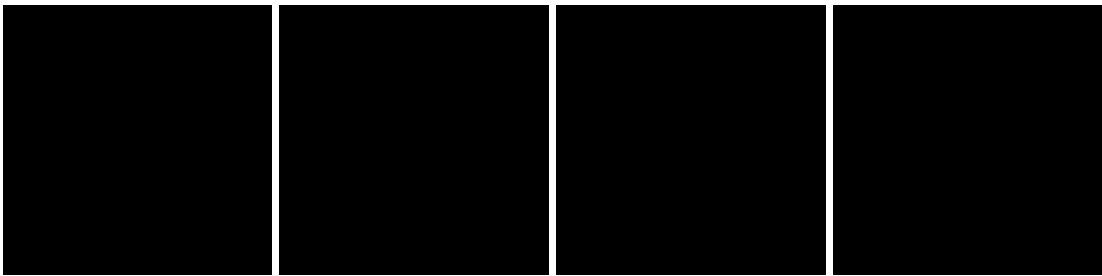
1 copy/ $\mu$ L in tap water assay #6



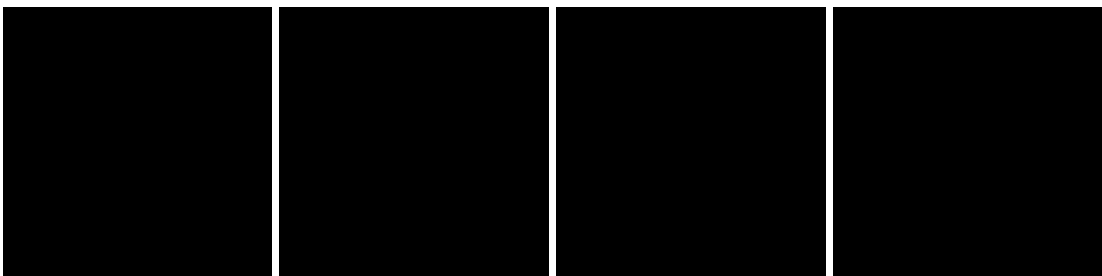
10 copies/ $\mu$ L in tap water assay #1



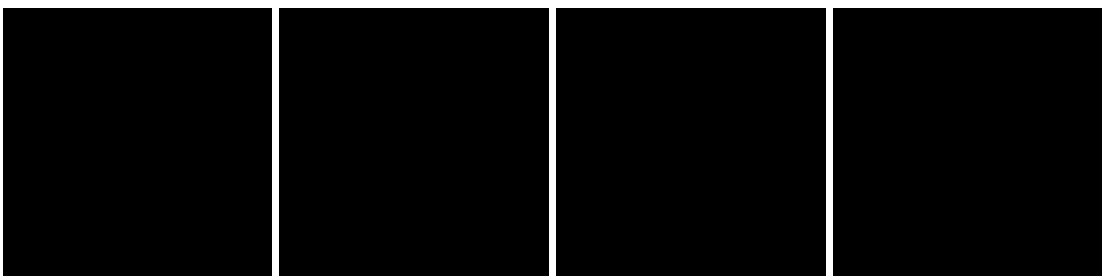
10 copies/ $\mu$ L in tap water assay #2



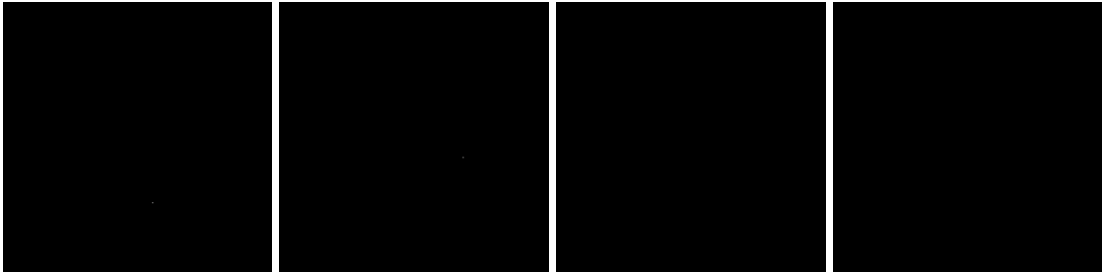
10 copies/ $\mu$ L in tap water assay #3



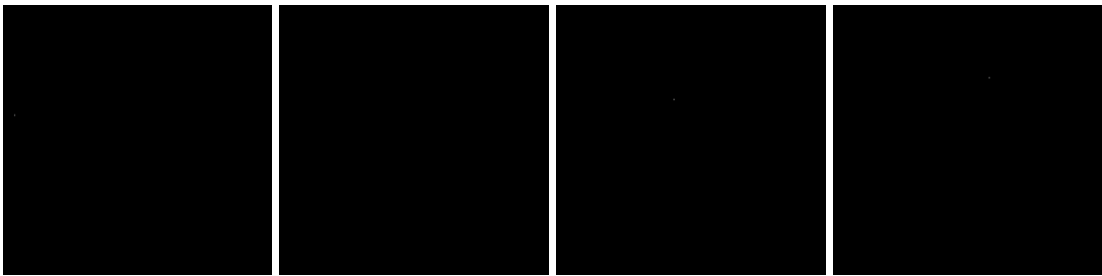
10 copies/ $\mu$ L in tap water assay #4



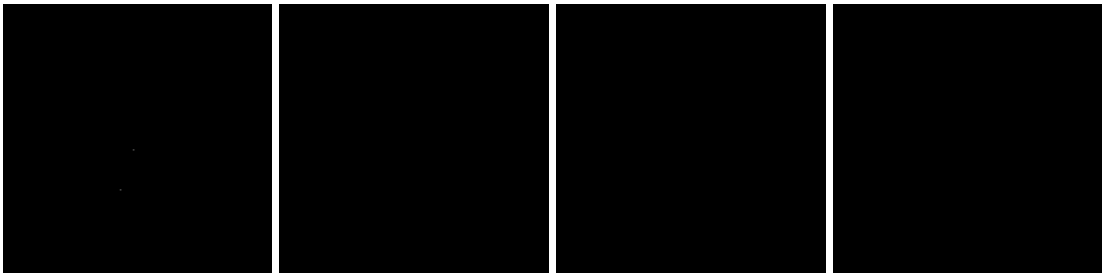
10 copies/ $\mu$ L in tap water assay #5



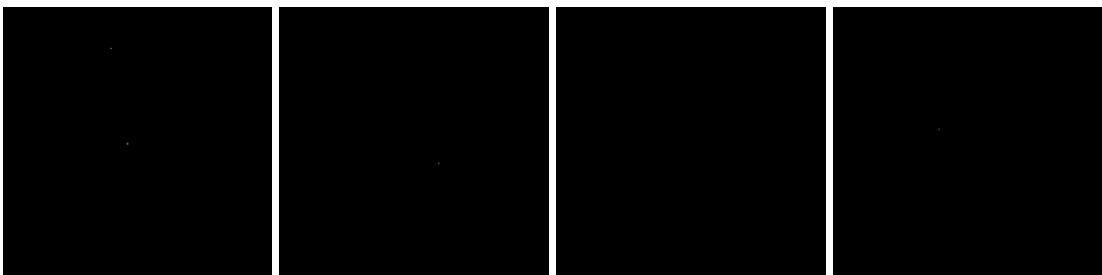
10 copies/ $\mu$ L in tap water assay #6



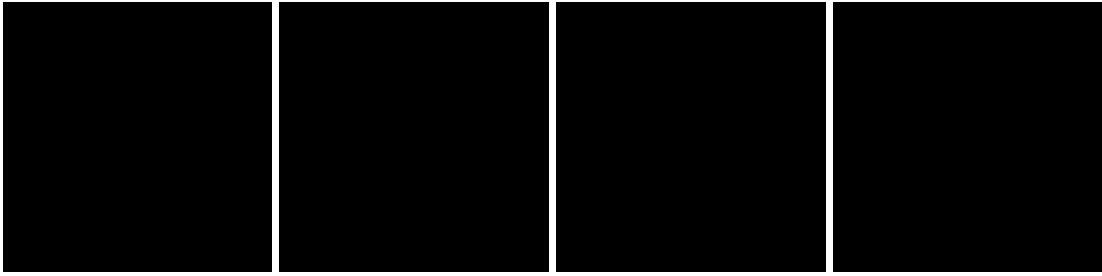
$10^2$  copies/ $\mu$ L in tap water assay #1



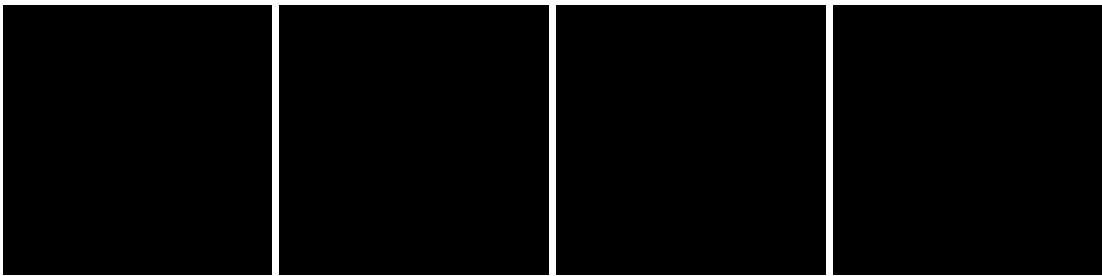
$10^2$  copies/ $\mu$ L in tap water assay #2



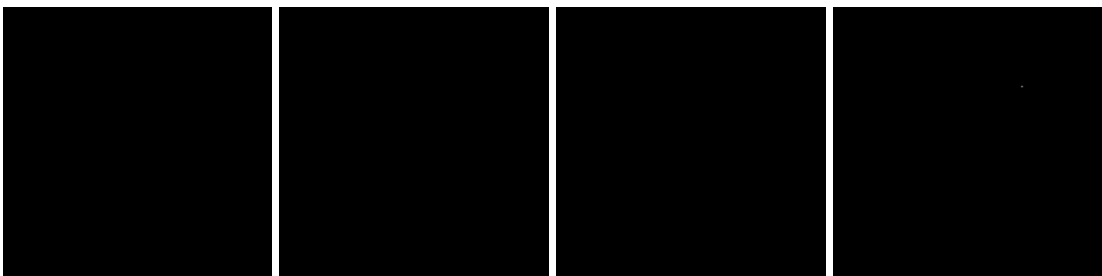
10<sup>2</sup> copies/μL in tap water assay #3



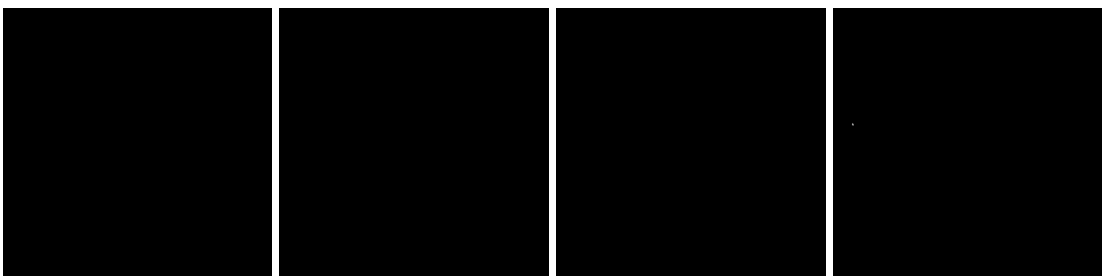
10<sup>2</sup> copies/μL in tap water assay #4



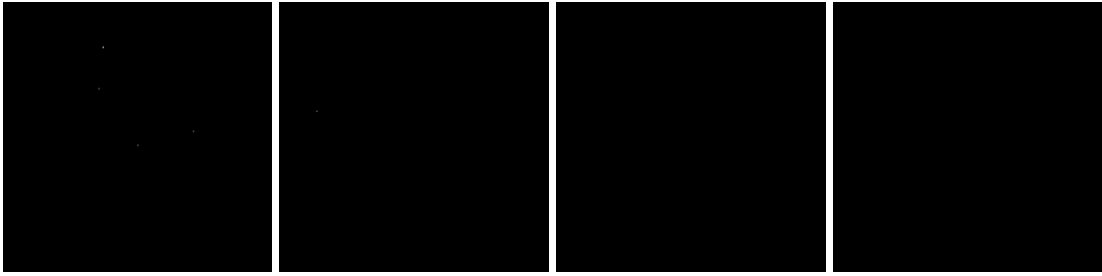
10<sup>2</sup> copies/μL in tap water assay #5



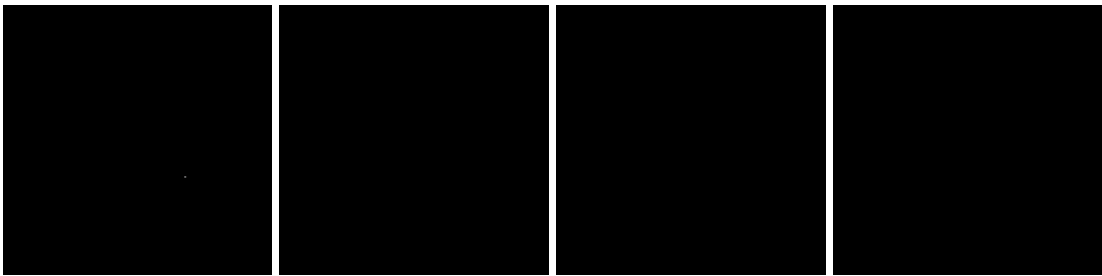
10<sup>2</sup> copies/μL in tap water assay #6



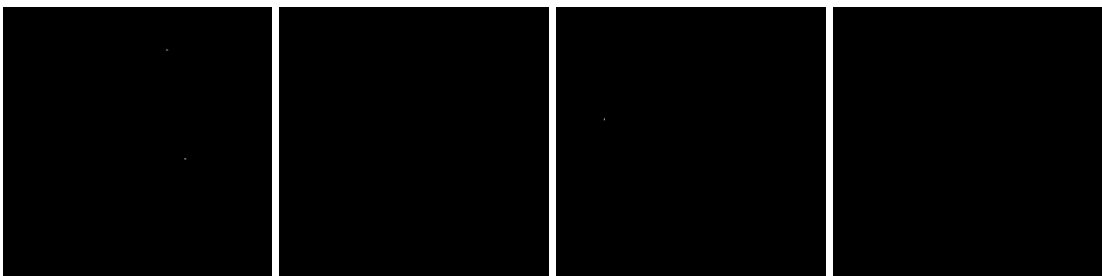
10<sup>3</sup> copies/μL in tap water assay #1



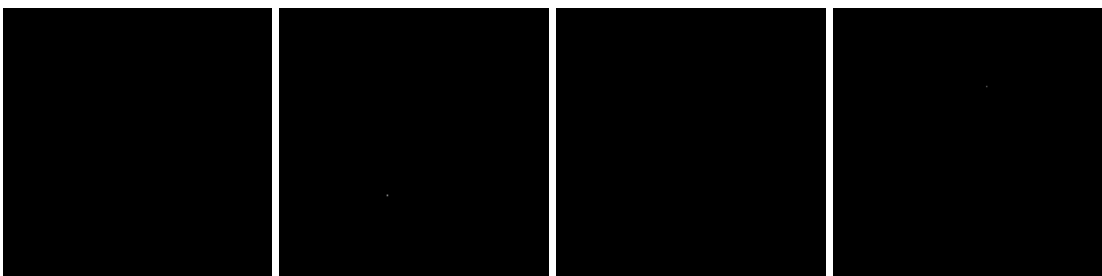
10<sup>3</sup> copies/μL in tap water assay #2



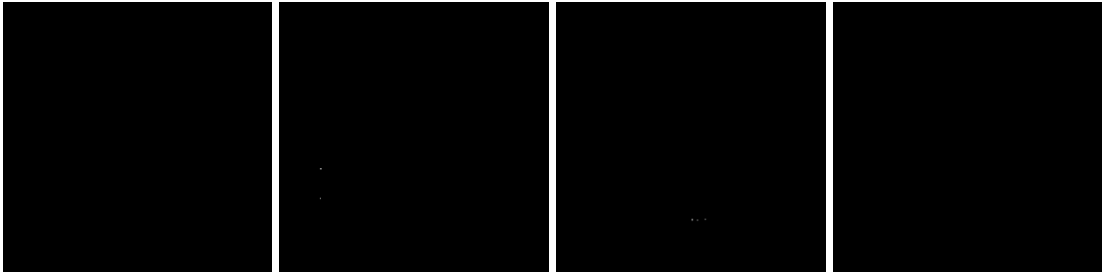
10<sup>3</sup> copies/μL in tap water assay #3



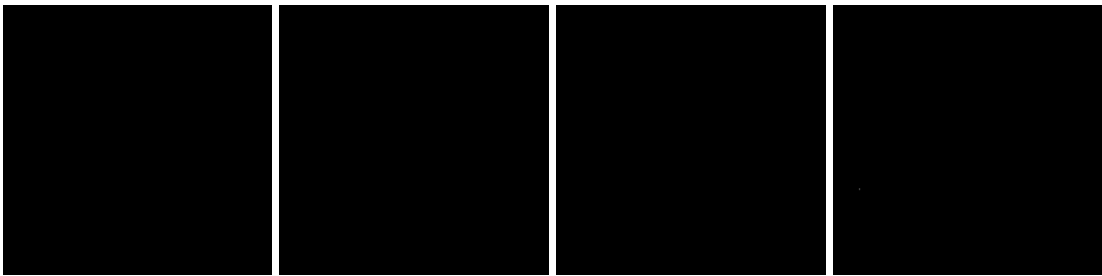
10<sup>3</sup> copies/μL in tap water assay #4



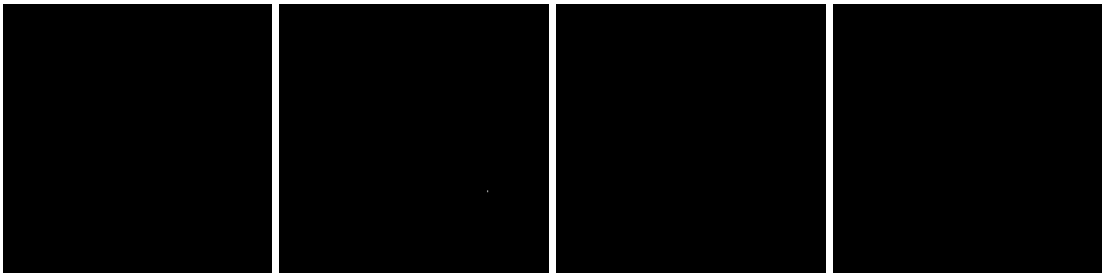
10<sup>3</sup> copies/μL in tap water assay #5



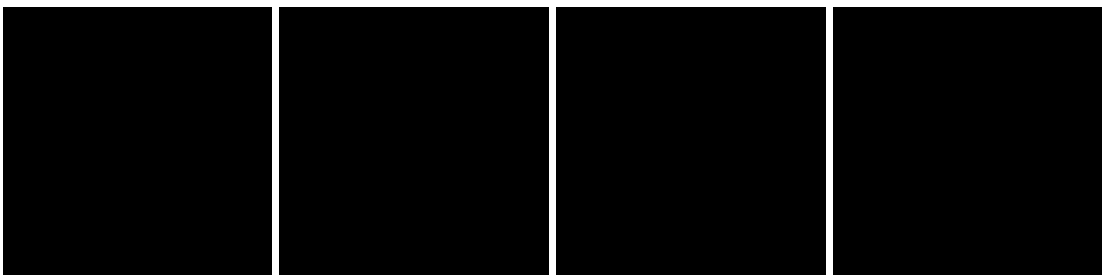
10<sup>3</sup> copies/μL in tap water assay #6



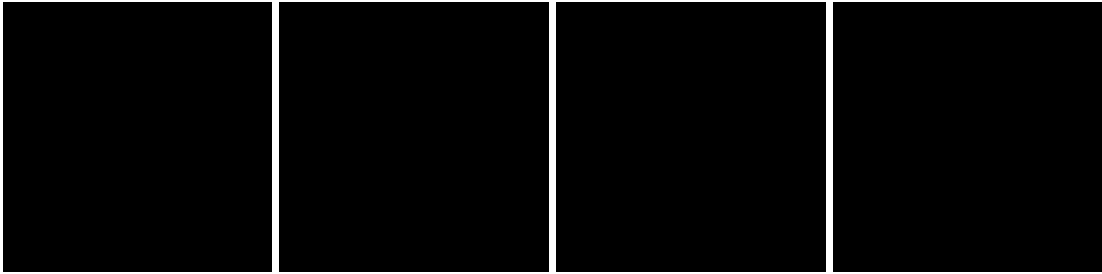
0 copy/μL in reclaimed wastewater assay #1



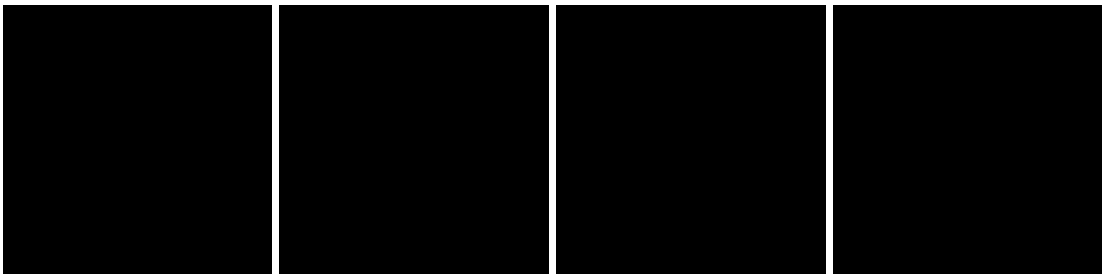
0 copy/μL in reclaimed wastewater assay #2



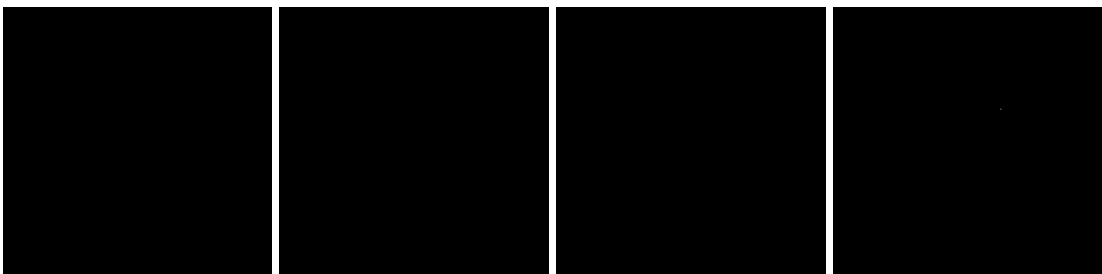
0 copy/ $\mu$ L in reclaimed wastewater assay #3



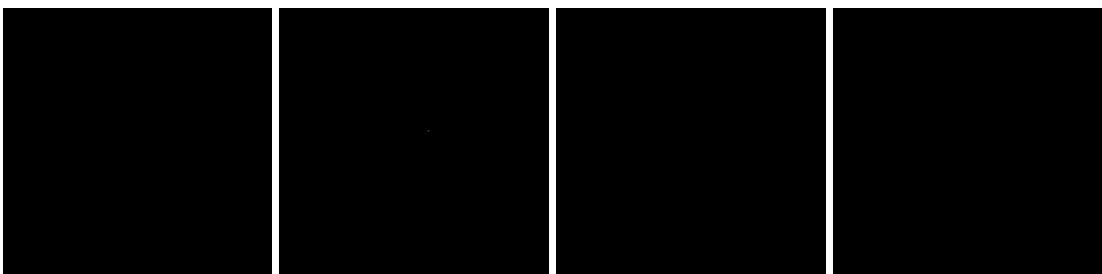
0 copy/ $\mu$ L in reclaimed wastewater assay #4



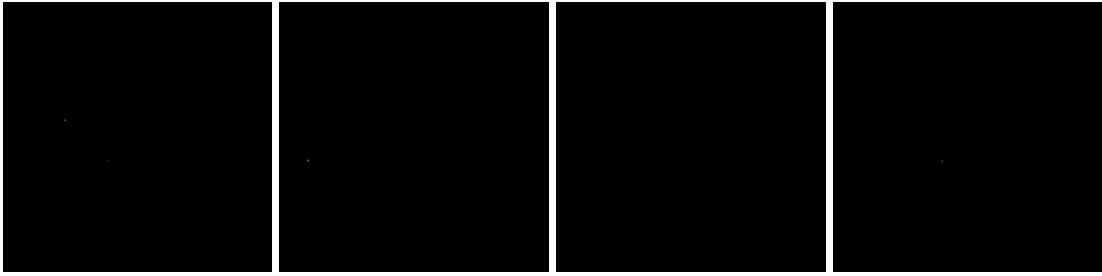
0 copy/ $\mu$ L in reclaimed wastewater assay #5



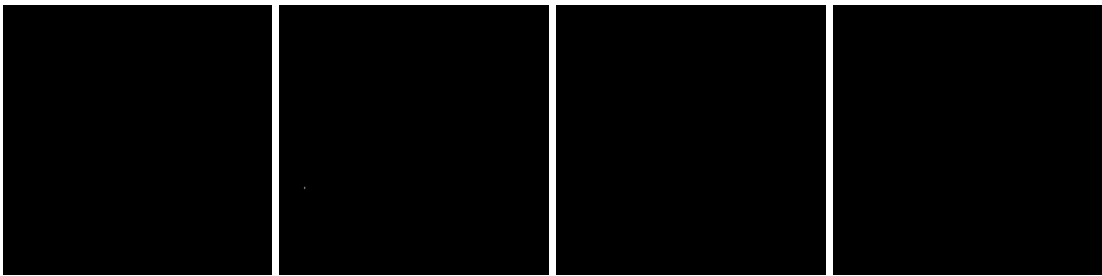
0 copy/ $\mu$ L in reclaimed wastewater assay #6



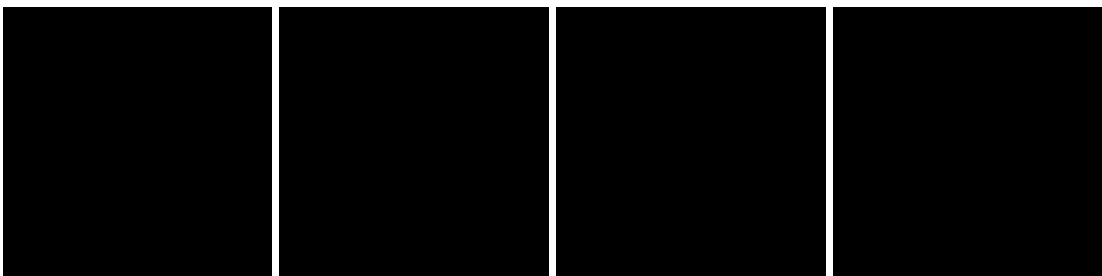
1 copy/ $\mu$ L in reclaimed wastewater assay #1



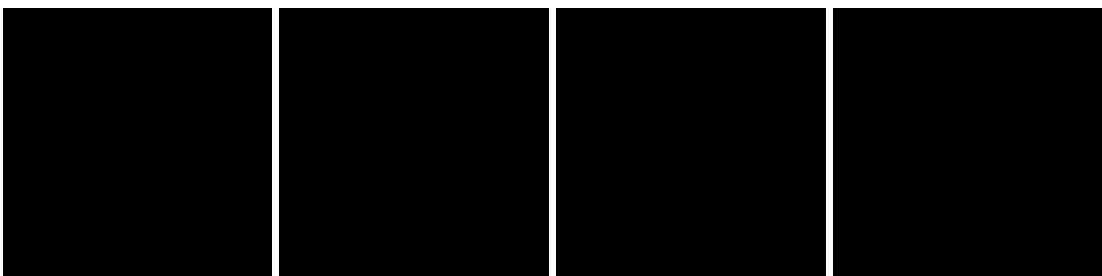
1 copy/ $\mu$ L in reclaimed wastewater assay #2



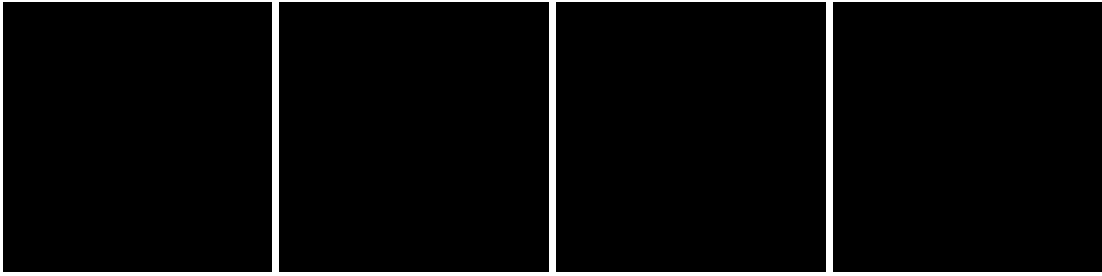
1 copy/ $\mu$ L in reclaimed wastewater assay #3



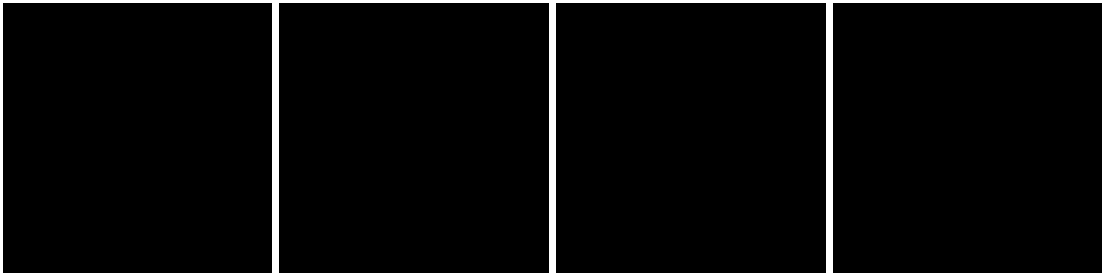
1 copy/ $\mu$ L in reclaimed wastewater assay #4



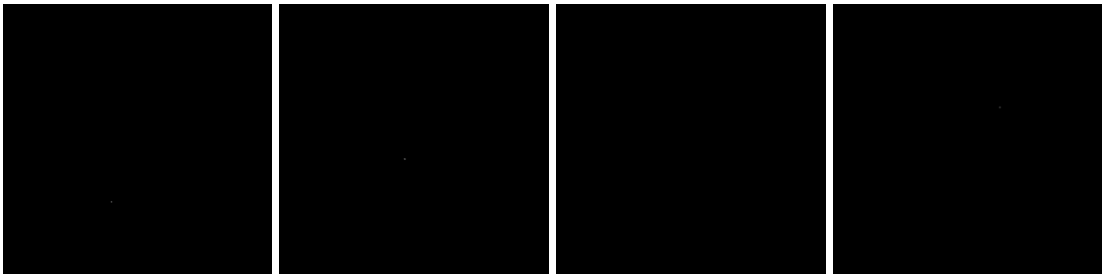
1 copy/ $\mu$ L in reclaimed wastewater assay #5



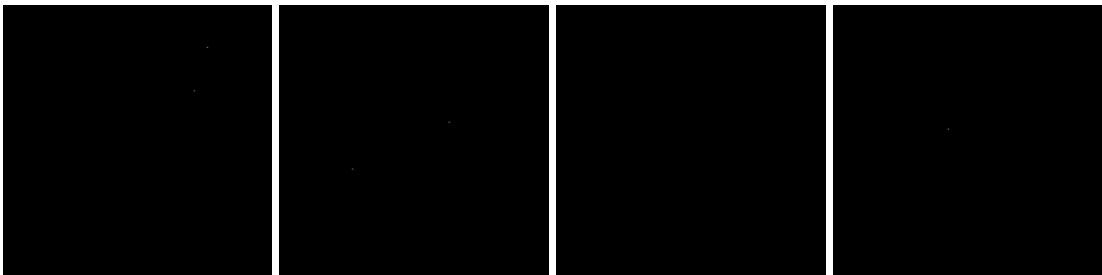
1 copy/ $\mu$ L in reclaimed wastewater assay #6



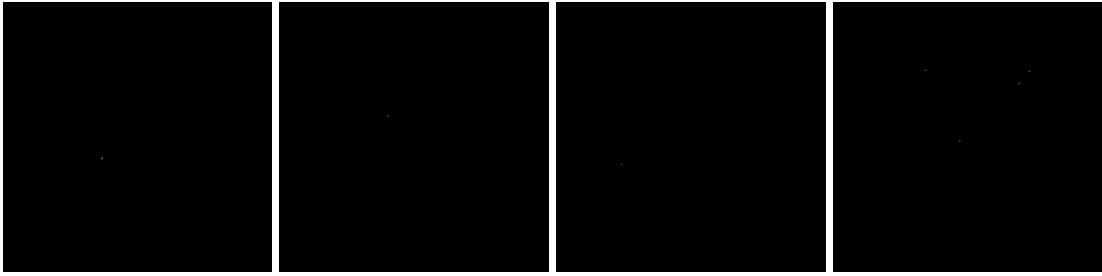
10 copies/ $\mu$ L in reclaimed wastewater assay #1



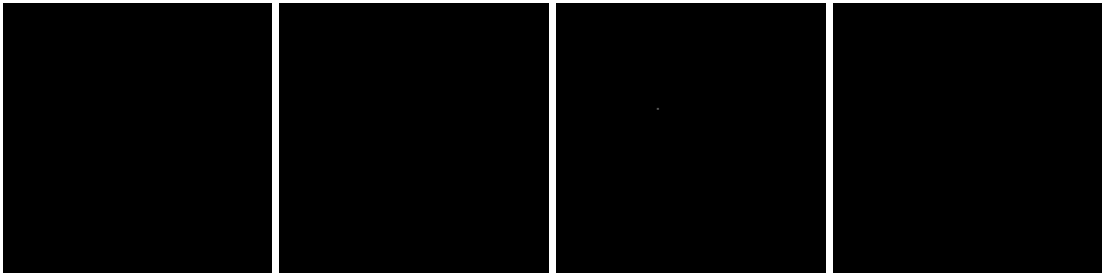
10 copies/ $\mu$ L in reclaimed wastewater assay #2



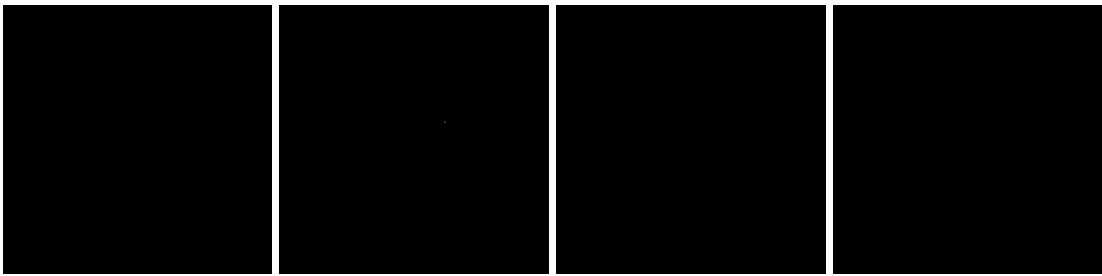
10 copies/ $\mu$ L in reclaimed wastewater assay #3



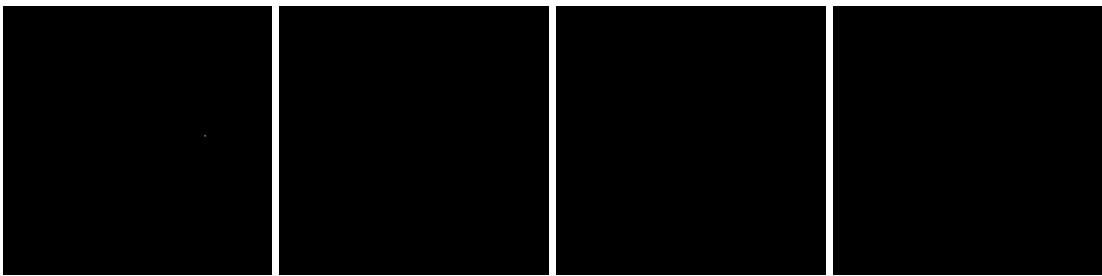
10 copies/ $\mu$ L in reclaimed wastewater assay #4



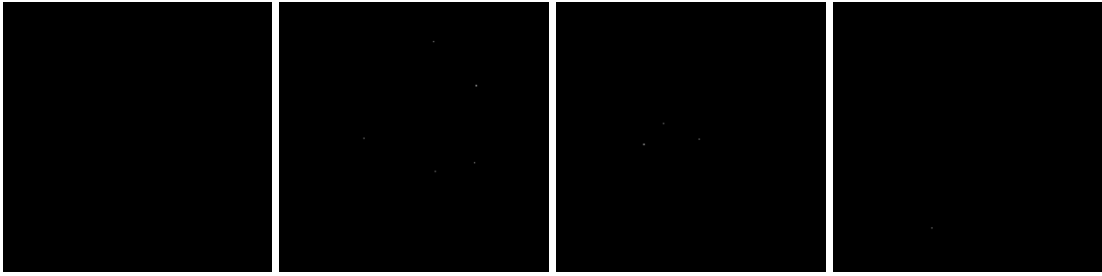
10 copies/ $\mu$ L in reclaimed wastewater assay #5



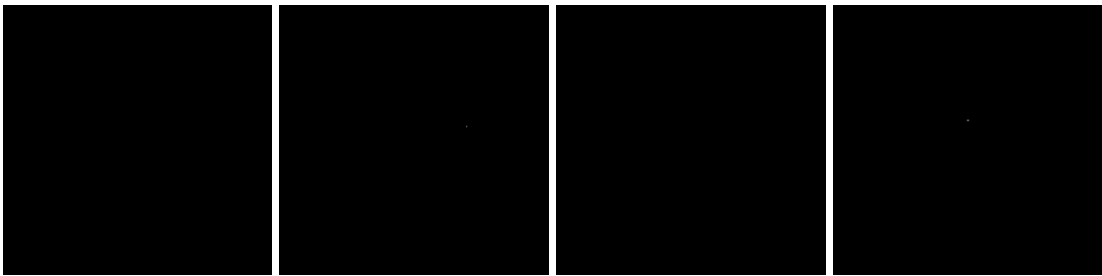
10 copies/ $\mu$ L in reclaimed wastewater assay #6



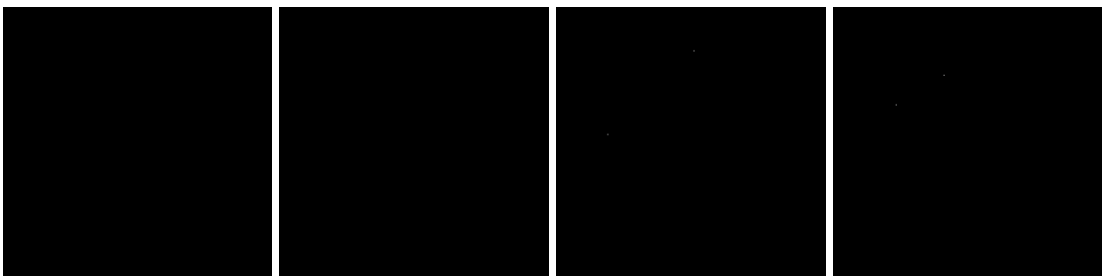
10<sup>2</sup> copies/μL in reclaimed wastewater assay #1



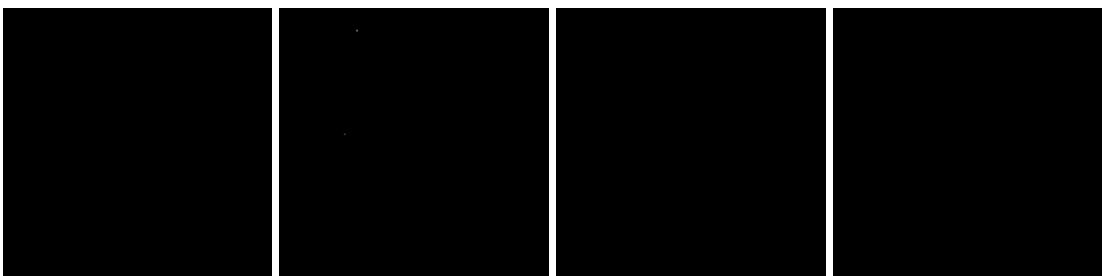
10<sup>2</sup> copies/μL in reclaimed wastewater assay #2



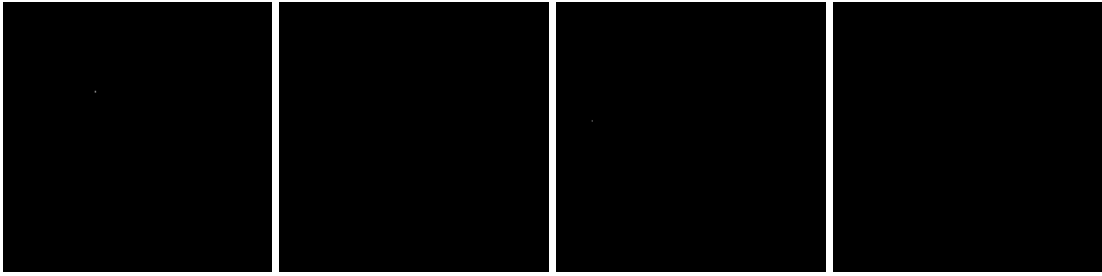
10<sup>2</sup> copies/μL in reclaimed wastewater assay #3



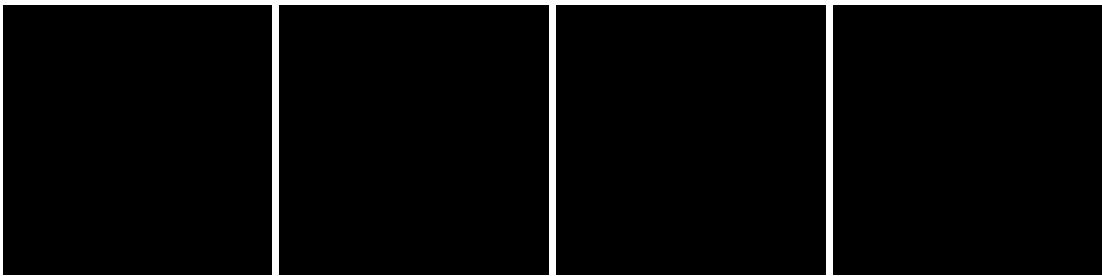
10<sup>2</sup> copies/μL in reclaimed wastewater assay #4



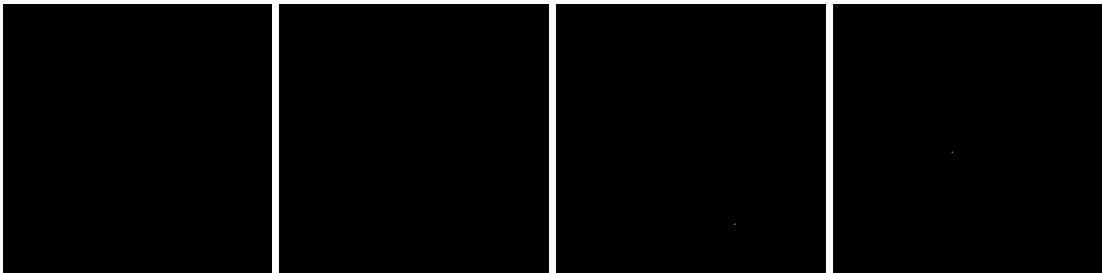
10<sup>2</sup> copies/μL in reclaimed wastewater assay #5



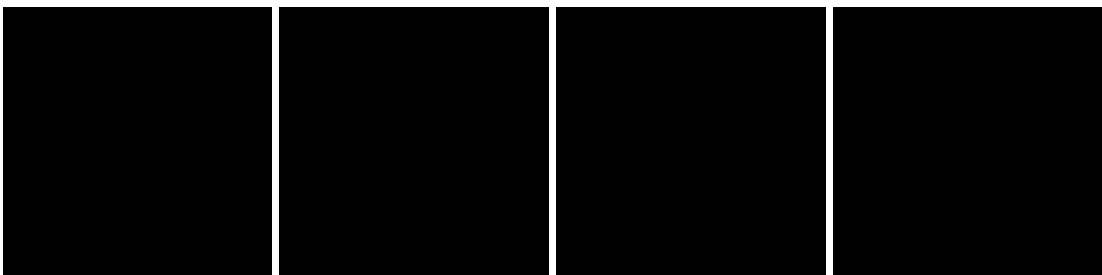
10<sup>2</sup> copies/μL in reclaimed wastewater assay #6



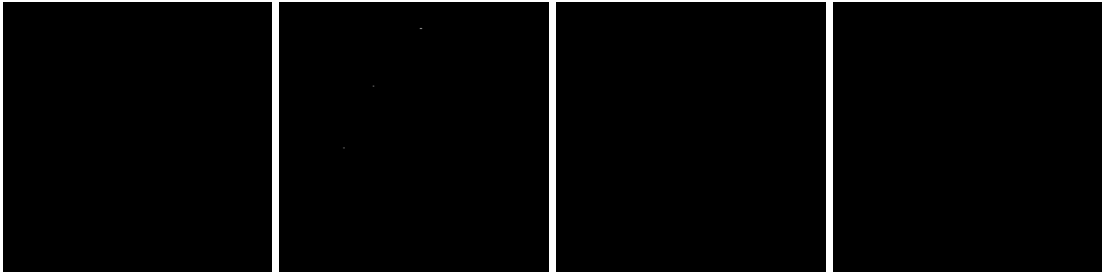
10<sup>3</sup> copies/μL in reclaimed wastewater assay #1



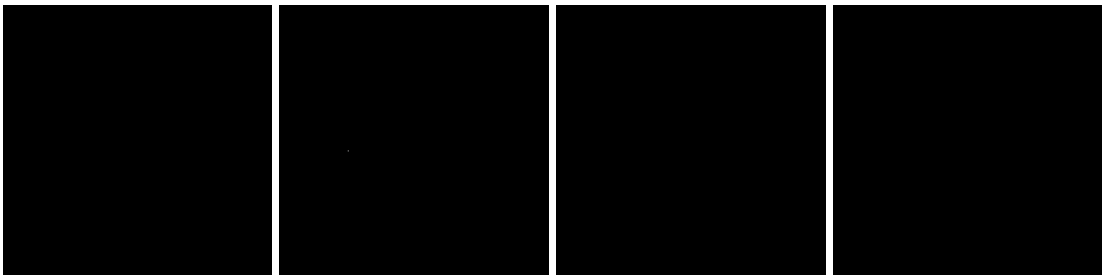
10<sup>3</sup> copies/μL in reclaimed wastewater assay #2



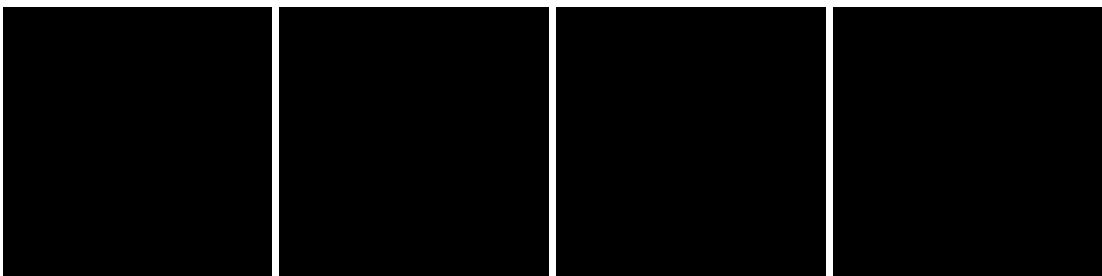
10<sup>3</sup> copies/μL in reclaimed wastewater assay #3



10<sup>3</sup> copies/μL in reclaimed wastewater assay #4



10<sup>3</sup> copies/μL in reclaimed wastewater assay #5



10<sup>3</sup> copies/μL in reclaimed wastewater assay #6

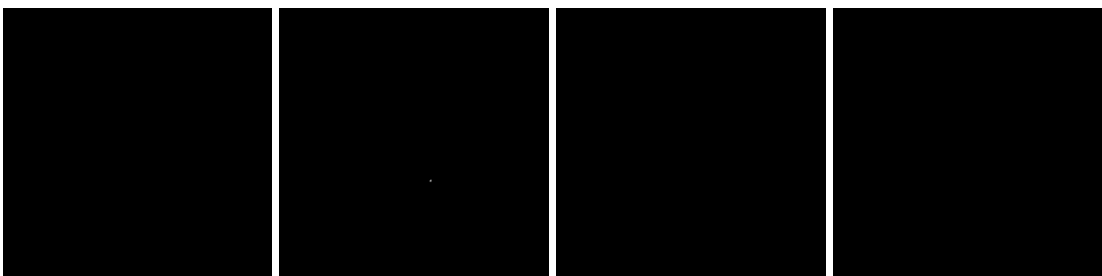
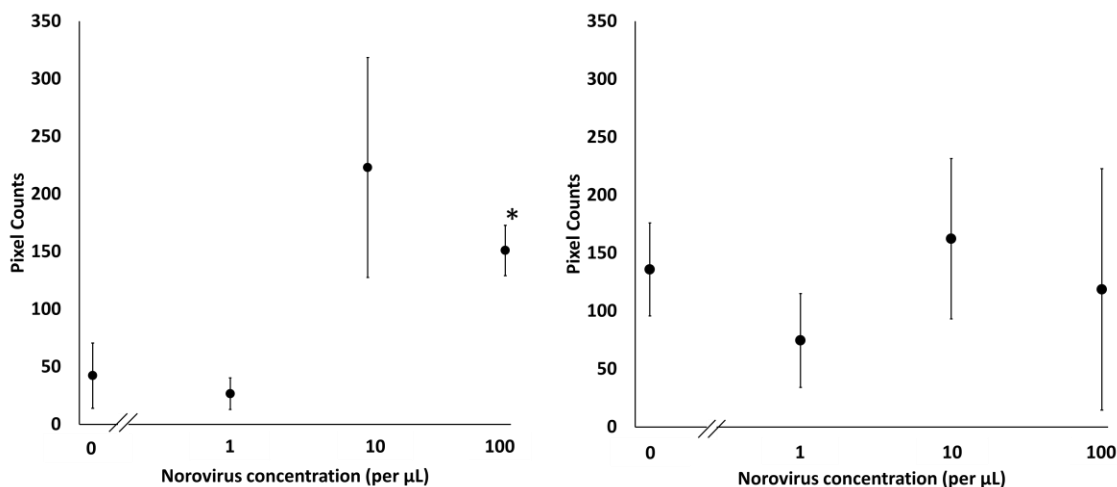


**Figure A-S4.** Smartphone assay results for 0.5 ppm (left) and 5 ppm (right) chlorine added to DI water. Other experimental conditions are identical to those shown in Figure 3.



## Author Information

### Corresponding Author

\*E-mail: [jyyoon@email.arizona.edu](mailto:jyyoon@email.arizona.edu).

### Author Contributions

J.-Y.Y. conceived the overall concept with input from S.C. and K.A.R. S.C. designed, assembled and fabricated  $\mu$ PADs and the smartphone based fluorescence microscope, and conducted all benchtop and smartphone microscope assay experiments, with assistance from L.E.B. and S.P. S.C. and J.-Y.Y. developed an image processing procedure. S.C. analyzed all data, with assistance from L.E.B. and input from J.-Y.Y. and K.A.R. W.Q.B. and C.M. collected water samples from the water reclamation facility and analyzed them by RT-qPCR. J.-Y.Y. and S.C. wrote the manuscript with input from L.E.B., S.P., W.Q.B. and K.A.R. All authors have given approval to the final version of the manuscript.

## **Funding Sources**

Funding for this research was provided by the University of Arizona National Science Foundation Water and Environmental Technology (WET) Center (award number IIP-1361815) and Tucson Water.

## **Notes**

The authors declare no competing financial interests.

## **Acknowledgment**

The authors are grateful to Dr. Ian L. Pepper and Dr. Charles P. Gerba, both at Department of Soil, Water and Environmental Science and Water and Energy Sustainable Technology (WEST) Center at the University of Arizona, as well as Daniel R. Quintanar at Tucson Water, for helpful discussions and suggestions for this project

## **References**

- (1) Katayama, H.; Vinjé, J. Norovirus and other Calicivirus. *Global Water Pathogens Project*. Michigan State University, East Lansing, and UNESCO. 2017.  
<<http://www.waterpathogens.org/book/norovirus-and-other-caliciviruses>>.
- (2) Teunis, P.F.M.; Moe, C.L.; Liu, P.; Miller, S.E.; Lindesmith, L.; Baric, R.S.; Le Pendu, J.; Calderon, R.L. Norwalk virus: how infectious is it? *J. Med. Virol.* **2008**, *80*, 1468-1476.

- (3) Atmar, R.L.; Opekun, A.R.; Gilger, M.A.; Estes, M.K.; Crawford, S.E.; Neill, F.H.; Ramani, S.; Hill, H.; Ferreira, J.; Graham, D.Y. Determination of the 50% human infectious dose for Norwalk virus. *J. Infect. Dis.* **2014**, *209*, 1016-1022.
- (4) Ettayebi, K.; Crawford, S.E.; Murakami, K.; Broughman, J.R.; Karandikar, U.; Tenge, V.R.; Neill, F.H.; Blutt, S.E.; Zeng, X.-L.; Qu, L.; Kou, B.; Opekun, A.R.; Burrin, D.; Graham, D.Y.; Ramani, S.; Atmar, R.L.; Estes, M.K. Replication of human noroviruses in stem cell–derived human enteroids. *Science* **2016**, *353*, 1387-1393.
- (5) Coudray-Meunier, C.; Fraisse, A.; Martin-Latil, S.; Guillier, L.; Delannoy, S.; Fach, P.; Perelle, S. A comparative study of digital RT-PCR and RT-qPCR for quantification of Hepatitis A virus and Norovirus in lettuce and water samples. *Int. J. Food Microbiol.* **2015**, *201*, 17-26.
- (6) de Bruin, E.; Duizer, E.; Vennema, H.; Koopmans, M.P. Diagnosis of Norovirus outbreaks by commercial ELISA or RT-PCR. *J. Virol. Meth.* **2006**, *137*, 259-264.
- (7) Park, J.P.; Cropek, D.M.; Banta, S. High affinity peptides for the recognition of the heart disease biomarker troponin I identified using phage display. *Biotechnol. Bioeng.* **2010**, *105*, 678-686.
- (8) Mu, X.; Zhang, L.; Chang, S.; Cui, W.; Zheng, Z. Multiplex microfluidic paper-based immunoassay for the diagnosis of hepatitis C virus infection. *Anal. Chem.* **2014**, *86*, 5338-5344.
- (9) Hu, J.; Wang, S.; Wang, L.; Li, F.; Pinguan-Murphy, B.; Lu, T.J.; Xu, F. Advances in paper-based point-of-care diagnostics. *Biosens. Bioelectron.* **2014**, *54*, 585-597.

- (10) Du, Y.; Pothukuchy, A.; Gollihar, J. D.; Nourani, A.; Li, B.; Ellington, A. D. Coupling sensitive nucleic acid amplification with commercial pregnancy test strips. *Angew. Chem. Int. Ed.* **2017**, *56*, 992–996.
- (11) Meng, X.-Y.; Gao, Y.; Zhang, H.; Luo, Y.; Sun, Y.; Qiu, H.-J. Cross-priming amplification-based lateral flow strip as a novel tool for rapid on-site detection of wild-type Pseudorabies virus. *Sens. Actuat. B: Chem.* **2018**, *259*, 573–579.
- (12) A. Rohrman, B.; R. Richards-Kortum, R. A Paper and Plastic Device for Performing recombinase polymerase amplification of HIV DNA. *Lab Chip* **2012**, *12*, 3082–3088.
- (13) Greening, G.E.; Cannon, J.L. Human and animal viruses in food (including taxonomy of enteric viruses). In *Viruses in Foods*; Springer: Berlin, 2016.
- (14) Weng, X.; Neethirajan, S. Aptamer-based fluorometric determination of norovirus using a paper-based microfluidic device. *Microchim. Acta* **2017**, *184*, 4545–4552.
- (15) Hagström, A. E. V.; Garvey, G.; Paterson, A. S.; Dhamane, S.; Adhikari, M.; Estes, M. K.; Strych, U.; Kourentzi, K.; Atmar, R. L.; Willson, R. C. Sensitive detection of norovirus using phage nanoparticle reporters in lateral-flow assay. *PLOS ONE* **2015**, *10*, e0126571.
- (16) Han, K. N.; Choi, J.-S.; Kwon, J. Three-dimensional paper-based slip device for one-step point-of-care testing. *Sci. Rep.* **2016**, *6*, 25710.
- (17) Cho, S.; Park, T.S.; Nahapetian, T.G.; Yoon, J.-Y. Smartphone-based, sensitive  $\mu$ PAD detection of urinary tract infection and gonorrhoea. *Biosens. Bioelectron.* **2015**, *74*, 601-611.

- (18) Fujita, M.; Adachi, K.; Nagasawa, M. Development of a homogeneous time-resolved fluorescence assay for detection of viral double-stranded RNA. *Anal. Biochem.* **2019**, *566*, 46–49.
- (19) Costantini, V.; Morantz, E. K.; Browne, H.; Ettayebi, K.; Zeng, X.-L.; Atmar, R. L.; Estes, M. K.; Vinjé, J. Human norovirus replication in human intestinal enteroids as model to evaluate virus inactivation. *Emerg. Infect. Dis.* **2018**, *24*, 1453–1464.
- (20) Park, T. S.; Yoon, J.-Y. Smartphone detection of *Escherichia coli* from field water samples on paper microfluidics. *IEEE Sens. J.* **2015**, *15*, 1902–1907.
- (21) Betancourt, W.Q.; Kitajima, M.; Wing, A.D.; Regnery, J.; Drewes, J.E.; Pepper, I.L.; Gerba, C.P. Assessment of virus removal by managed aquifer recharge at three full-scale operations. *J. Environ. Sci. Health A* **2014**, *49*, 1685-1692.
- (22) Kageyama, T.; Kojima, S.; Shinohara, M.; Uchida, K.; Fukushi, S.; Hoshino, F.B.; Takeda, N.; Katayama, K. Broadly reactive and highly sensitive assay for Norwalk-like viruses based on real-time quantitative reverse transcription-PCR. *J. Clin. Microbiol.* **2003**, *41*, 1548-1557.
- (23) Kitajima, M.; Oka, T.; Haramoto, E.; Takeda, N.; Katayama, K.; Katayama, H. Seasonal distribution and genetic diversity of genogroups I, II, and IV noroviruses in the Tamagawa River, Japan. *Environ. Sci. Technol.* **2010**, *44*, 7116-7122.
- (24) Ahmed, S.R.; Takemeura, K.; Li, T.C.; Kitamoto, N.; Tanaka, T.; Suzuki, T.; Park, E.Y. Size-controlled preparation of peroxidase-like graphene-gold nanoparticle hybrids for the visible detection of norovirus-like particles. *Biosens. Bioelectron.* **2017**, *87*, 558-565.

- (25) Ashiba, H.; Sugiyama, Y.; Wang, X.; Shirato, H.; Higo-Moriguchi, K.; Taniguchi, K.; Ohki, Y.; Fujimaki, M. Detection of norovirus virus-like particles using a surface plasmon resonance-assisted fluoroimmunosensor optimized for quantum dot fluorescent labels. *Biosens. Bioelectron.* **2017**, *93*, 260-266.

## Appendix B

### Smartphone near infrared monitoring of plant stress

Soo Chung<sup>1</sup>, Lane E. Breshears<sup>2</sup>, and Jeong-Yeol Yoon<sup>1,2\*</sup>

<sup>1</sup>Department of Biosystems Engineering, and <sup>2</sup>Department of Biomedical Engineering,  
The University of Arizona, Tucson, Arizona 85721, United States

\*Corresponding author.

\*Corresponding author E-mail address: [jyyoon@email.arizona.edu](mailto:jyyoon@email.arizona.edu)

Received 11 April 2018; Received in revised form 28 August 2018; Accepted 30 August  
2018

Available online 08 September 2018

<https://doi.org/10.1016/j.compag.2018.08.046>

0168-1699/© 2018 Elsevier B.V. All rights reserved.

## **Abstract**

The most widely used method for monitoring plant stress is the use of near infrared (NIR) spectrophotometry to calculate normalized difference vegetation index (NDVI), as defined by  $[\text{NIR reflectance} - \text{red reflectance}] / [\text{NIR reflectance} + \text{red reflectance}]$ . NDVI measures the chlorophyll absorption in the red spectrum relative to the scattering by cellular structure in NIR, and has been used to monitor vegetation health and subsequently its stress from aerial or satellite images. Rather than using an NIR spectrophotometer or an NIR camera that is rather expensive, we attempted to use a commercial smartphone, utilizing its (potentially unintended) ability in recognizing near infrared (NIR) color. Some of the most recent versions of smartphones have eliminated the NIR block filters on their cameras, and are able to recognize NIR in their red pixels of CMOS array. Through attaching an inexpensive high pass filter at 800 nm to a smartphone camera, we were able to collect the NIR reflectance (with a high pass optical filter) and the red reflectance (without a filter), enabling NDVI assessments. This method was verified by measuring the NDVI values from a series of chlorophyll solutions, and showed a strong linear correlation with  $R^2 = 0.948$ , corroborating the smartphone's ability in evaluating NDVI. Using the leaves from three different plant species, the NDVI values were evaluated using the smartphone and compared with the plants' chlorophyll contents using acetone extraction and subsequent spectrophotometry. A good linear relationship was found with  $R^2 = 0.88 - 0.92$ . We further evaluated the NDVI values against the plants' water contents (measured by oven-drying), showing the non-linear relationship with the NDVI saturation above 50% water content. The assay time was almost instantaneous, requiring only a smartphone and a high pass

filter, thus allowing inexpensive, easy-to-use, rapid, and early prediction of plant stress that can be used for field and household applications.

*Keywords:* Near infrared (NIR); Normalized difference vegetation index (NDVI); Plant health; Smartphone imaging; Real-time monitoring.

## 1. Introduction

Chlorophyll is a pigment that exists in the chloroplasts and plays an essential role for photosynthesis, a well-known growth method for plants. Chlorophyll content per leaf area can serve as an indicator for plant health and subsequently plant stress (Steele et al., 2008). One of the majority of plant stress is attributed to water stress (Blum, 2018).

Diverse research has been conducted to evaluate the health and stress in plants. Early attempts include automated machine vision (Kacira et al., 2002), focusing on green coloration under controlled environments. However, green reflectance is much weaker than near infrared (NIR) or infrared (IR) reflectance and can vary significantly by ambient conditions, thus may not provide accurate information on the plant stress. IR based thermal imaging has also been attempted to monitor plant water stress. Originally developed for mapping temperature distribution of an object, it can also be used to evaluate the plants' water content due to the strong IR absorption by water (Meron et al., 2010). However, IR thermal imaging cameras are still expensive (although their price has dropped significantly in the last decade), and the results are greatly affected by environmental temperature and humidity. Hyperspectral imaging has also been used to better quantify plant stress (Kim et al., 2011), but this method requires integration of multiple cameras and sensors (or an expensive ready-to-use equipment) to acquire sufficient amount of data.

As mentioned above, green color is reflected the most by plant leaves, providing characteristic green color for healthy plants, due to the chlorophyll's absorption in blue and red color. While green reflectance is usable, NIR and IR based methods provide much better results in monitoring plant health and stress (especially by water) (Peñuelas and Filella, 1998). In recent decades, normalized difference vegetation index (NDVI) has been

utilized as a major indicator for the health status of plants and green biomass (e.g. algae), and indirectly their water contents (Rouse, 1973). It is based on the difference between the plant's red reflectance (*Red*) due to the pigment absorption by chlorophyll and the NIR reflectance (*NIR*) due to the scattering by cellular (spongy mesophyll) structure, which is defined as  $NDVI = (NIR - Red) / (NIR + Red)$  (Tucker, 1979). There are many studies reporting that NDVI has a linear relation with rainfall (Aguilar et al., 2012), with temperature (Wang et al., 2003), and with evapotranspiration (Groeneveld, 2008), as well as with water stresses (Kim et al., 2011; Zhao et al., 2015).

Despite these merits of NDVI spectrophotometry and imaging, it still requires an NIR spectrophotometer or an NIR camera, which can be expensive. If a smartphone camera can be used, it will provide a simple and low-cost alternative to an NIR camera, for use in small farms or residential homes. However, no such study has been demonstrated until now, due to the difficulty in capturing NIR using a smartphone camera. Even if a smartphone can recognize NIR, these intensities will be added to those considered red intensity (closest wavelength). This makes it difficult to differentiate NIR reflectance from red reflectance in smartphone images. Recent smartphones, e.g. iPhone 5 through 7, used an NIR block filter to eliminate the NIR influence. However, the most recent smartphones, such as iPhone 8 or Galaxy S8, do not use such NIR block filter (experimentally confirmed in this study), presumably to lower the unit price, or potentially to use in conjunction with facial recognition feature. This elimination of an NIR block filter can be exploited as an advantage towards NDVI measurement. While both NIR and red reflectance are recognized by the red pixels in a smartphone camera, it is possible to make a distinction by capturing two images, one with an 800 nm high pass filter (for NIR reflectance) and the

other without (for red reflectance). A high pass filter at 800 nm will eliminate all wavelengths below NIR and the resulting smartphone images should represent only the NIR reflectance.

The aim of this study is to demonstrate the use of a smartphone for NDVI acquisition for rapid diagnosis of leaf health and stress. Three different species of plants, Japanese mock-orange cheesewood, Red gum eucalyptus, and Tea rose, were tested, which are very popular shrubs for landscaping in southern Arizona. They can resist heat and drought to a certain extent while requiring constant supply of drip irrigation, serving as optimum models for monitoring plant health and stress. The smartphone acquired NDVI values were compared to a standard analysis of the chlorophyll solutions and the extracted chlorophylls from plant leaves.

## **2. Materials and Method**

### **2.1. Various smartphones' abilities in recognizing NIR**

Eight different smartphones were tested in this experiment to find the most appropriate model: Galaxy S7 and S8 (Samsung Electronics, Co., Ltd., Seoul, South Korea), Nexus 5X (Google LLC, Mountain View, CA, USA), iPhone 5, 6S, SE, 7 and 8 (Apple Inc., Cupertino, CA, USA). Each smartphone's ability to capture NIR was tested using an 850 nm LED (L3-0-IR5TH50-1, LEDSupply, Randolph, VT, USA) as well as a 940 nm LED (L2-0-IR5TH30-1, LEDSupply). Both LEDs were powered with 5.75 V, using a 200  $\Omega$  protective resistor. The voltage drops were 1.39 V for 850 nm LED and 1.23 V for 940 nm LED, and currents were 21.8 mA for 850 nm LED and 22.6 mA for 940 nm,

all of which are within normal operating conditions as specified by the manufacturer. These smartphones captured the images 10 cm away (the closest distance with optimum focusing) from these NIR LEDs in a dark room, using shutter time = 1/8 s, white balance = 4500 K, and ISO = 400.

## **2.2. Chlorophyll solutions**

Chlorophyll a (479-61-8, Sigma-Aldrich Corp., St. Louis, MO, USA) was dissolved into 96% ethanol to make 10, 20, 40, 60 and 80  $\mu\text{g}/\text{mL}$  solutions. These solutions were placed in plastic containers, on top of a white paper as a consistent background, for the smartphone based NDVI measurements.

## **2.3. Chlorophyll extraction and spectrophotometric quantification from plant leaves**

Three different plant leaves were tested in this experiment: Japanese mock-orange cheesewood (*Pittosporum tobira*), red gum eucalyptus (*Eucalyptus camaldulensis*), and hybrid tea rose (*Rosa* sp.). Plants were obtained from the University of Arizona main campus. 9 to 11 leaves were acquired for each plant; roughly three healthy (green), three half-dried (yellow-green), and three dried (yellow) leaves. After measuring the NDVI values using a smartphone, 100% acetone was applied to these leaves to extract chlorophyll. The solutions were analyzed using a miniature spectrophotometer (USB4000, Ocean Optics, Inc., Dunedin, FL, USA) following the equation by Lichtenthaler (Lichtenthaler, 1987).

## **2.4. Water contents of plant leaves**

42 leaves were acquired for each plant species. To calculate their water content, the weights of all leaves were measured using an electronic balance (0.1 mg accuracy; model number AR2140; Ohaus Corp., Pine Brook, NJ, USA), followed by drying them in full in an oven (model number 1321F; Sheldon Manufacturing, Inc., Cornelius, OR, USA) at 100°C and re-measuring their weights. To ensure all leaves are fully dried, dried weights were also measured after 15 minutes, 30 minutes, 1 hour, 2 hours, 3 hours, and 4 hours. Dried weights did not change by two times the balance' accuracy, i.e.  $< 0.2 \pm 0.1$  mg, corresponding to 95% confidence interval, after 3 hours for all leaves tested, which were used as bases for calculating their water contents.

## **2.5. NDVI measurements using a smartphone and an NIR filter**

Leaf images (or the images of chlorophyll solutions in container) were taken with the Galaxy S8 smartphone camera with and without an 800 nm high pass filter (catalog number FEL0800; Thor Labs, Newton, NJ, USA). Leaves (or chlorophyll solutions) were placed on a white paper, providing a consistent background. The images without the filter were used to measure the red color reflectance (*Red*) and the images with the filter were used to measure the NIR reflectance (*NIR*), as illustrated in Figure B-1. The smartphone was positioned 10 cm away from the leaf to allow optimum focusing, and at 45° from the leaf that minimized the non-specific reflection and the shadow of the smartphone itself.

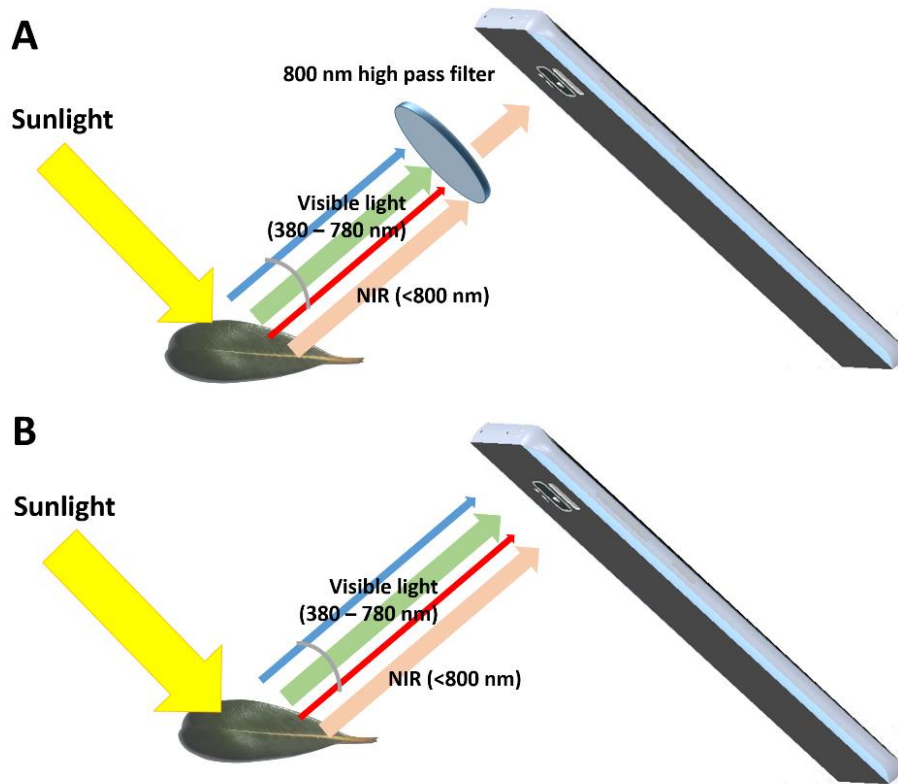


Figure B- 1. Schematic illustration of smartphone based NDVI measurement. (A) An 800 nm high pass filter is used to obtain the NIR reflectance (NIR). (B) Without the high pass filter, all visible lights are captured in a smartphone camera, which is used to measure the red reflectance (Red).

## 2.6. Image analysis

ImageJ (US National Institutes of Health; Bethesda, MD, USA) was used to process the images taken by a smartphone. All images were split into red, green, and blue channels and the split images were converted to gray scale images. Only the red channel images were used to measure the red and NIR reflectance as shown in Figure B-2 (refer to Introduction and Results and Discussion for further explanations). Images were cropped to

isolate the image of a leaf (or a chlorophyll solution in a container) and average red pixel intensities were evaluated from the cropped images. These intensities were divided with the background intensity to obtain red or NIR reflectance. These values were used to calculate  $NDVI = (NIR - Red) / (NIR + Red)$ .

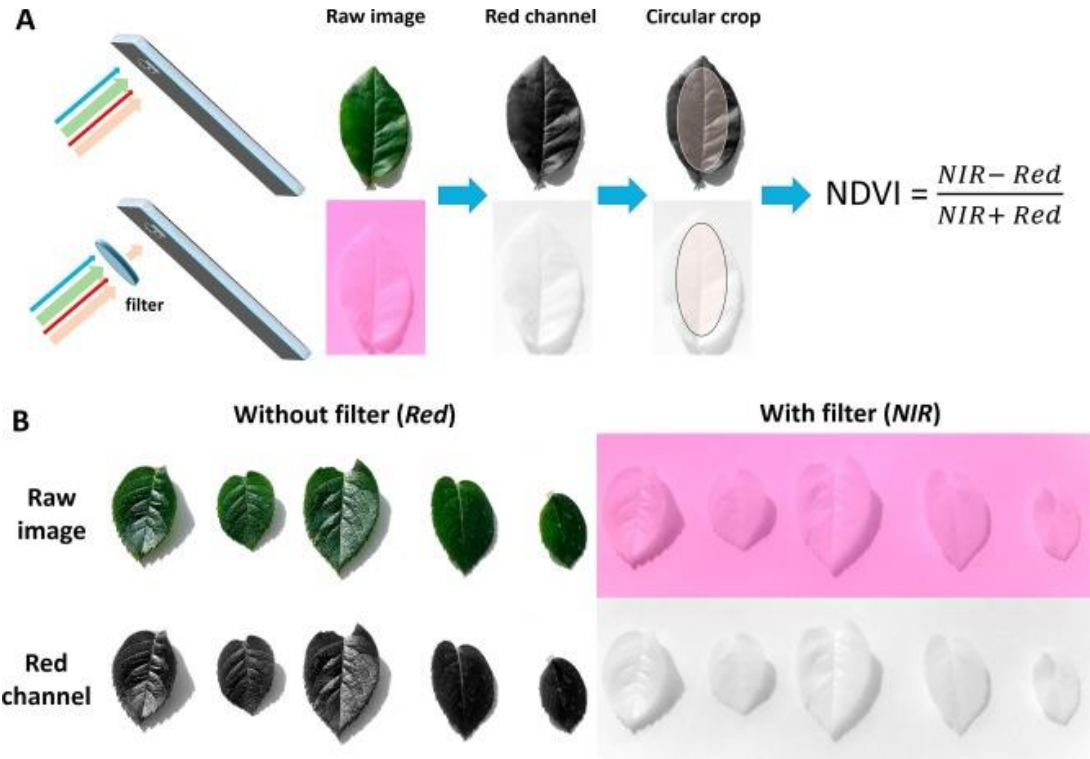


Figure B- 2. Image analysis. (A) Schematic illustration of calculating the NDVI values through image analysis.  $NDVI = (NIR - Red)/(NIR + Red)$ . (B) Smartphone images without the 800 nm high pass filter (left) and with the filter (right). Both raw images (above) are split to red channel (below) to measure the NIR and red reflectance.

### **3. Results and discussion**

#### **3.1. Various smartphones' abilities in recognizing NIR**

Several models and brands of commercial smartphones have been tested for their abilities in recognizing NIR color (Figure A-3). All of the Android smartphones (Galaxy S8, Galaxy S7, and Nexus 5X) and the very recent iOS smartphone (iPhone 8) were able to image the 850 nm LED. All other iOS smartphones (iPhone 7, SE, 6S and 5) were not able to recognize both 850 nm and 940 nm LEDs. Among the four models that recognized an 840 nm LED, the most clear and brightest image could be obtained using Galaxy S8. Since it is desirable not to recognize longer wavelength NIR for the optimum NDVI measurement (Lorenzen and Jensen, 1988, Adamsen et al., 1999, Nagler et al., 2000), the images of a 940 nm LED should appear black, which was the case with Galaxy S8 and iPhone 8, i.e., the most recent versions of smartphones. Considering the clearness and brightness of an 840 nm LED image and the inability of recognizing a 940 nm LED, Galaxy S8 was chosen as the optimum smartphone for NDVI measurements.

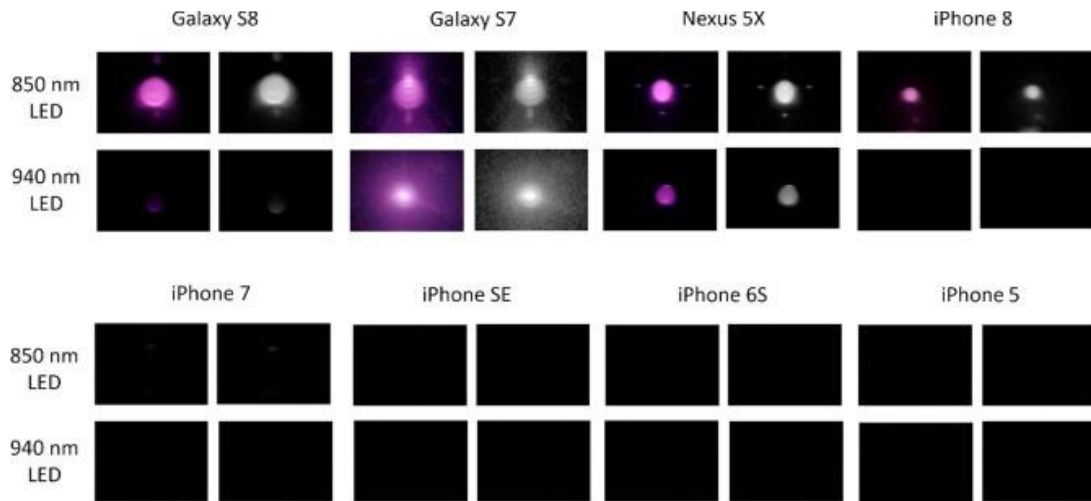


Figure B- 3. NIR LED images using various smartphones. VLED = 1.39 V (850 nm LED) and 1.23 V (940 nm LED); Distance between a smartphone and an LED = 10 cm; Shutter time = 1/8 s; White balance = 4500 K; ISO = 400.

### 3.2. Smartphone-acquired NDVI values of chlorophyll solutions

A series of chlorophyll a solutions were prepared to evaluate the smartphone's ability to quantify them. Chlorophyll a is the major form of chlorophylls in plant leaves and it is the most sensitive to NDVI measurements, showing the strongest absorbance in red color. Smartphone images of chlorophyll a solutions were captured with or without an 800 nm high pass filter (Figure B-1b), and split into three color channels (RGB) using ImageJ. Each split image was 8 bit with pixel intensities ranging from 0 to 255. As described in Introduction and Materials and Method, only the red channel images (converted to gray scale images) were used for both images with and without an 800 nm high pass filter. Square crops were used at the center of the container, to extract the average NIR reflectance (NIR) with an 800 nm high pass filter, and the average red reflectance (Red) without an 800 nm high pass filter.

Since smartphones are less sensitive to NIR than red color, different shutter speeds have been used by using camera application (ProShot, Rise Up Games, LLC, Los Angeles, CA, USA): 1/8 s for the images with an 800 nm high pass filter and 1/2000 s without the filter. While the images with the high pass filter showed only the NIR reflectance, those without the filter should show the sum of both NIR and red reflectance in principle. The NIR reflectance, however, should be noticeably weaker than the red reflectance when measured at the same time, and is virtually negligible at shorter shutter speed (1/2000 s used for measuring the red reflectance). In fact, there was no statistical difference ( $p < 0.05$ ) in the red pixel intensities with a 800 nm low pass filter (capturing only visible light) and without (capturing both visible and NIR light) at the short shutter speed of 1/2000 s. Therefore, for the sake of simplicity, only the 800 nm high pass filter has been used throughout this study.

NDVI values were evaluated using these data and plotted against the chlorophyll a concentration, as shown in Figure B-4. The plot showed strong linear correlation with  $R^2$  value of 0.948, indicating that the smartphone-acquired NDVI values are highly and accurately correlated to the chlorophyll concentration.

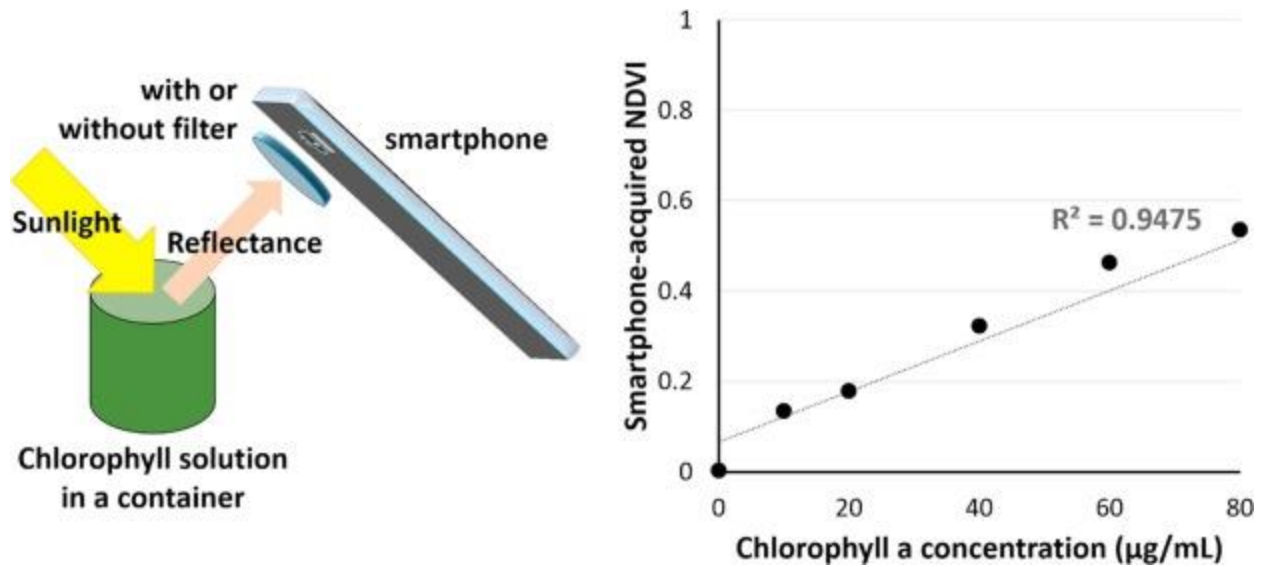


Figure B- 4. Plot of smartphone-acquired NDVI values of chlorophyll a solutions.

### 3.3. Smartphone-acquired NDVI vs. The leaf chlorophyll content

Three different species of plants were used for this experiment: Japanese mock-orange cheesewood, red gum eucalyptus, and tea rose. 9 to 11 leaves from each plant species were collected, with varied colorations (and thus varied healthiness), and the NDVI values were measured using the smartphone with or without the 800 nm high pass filter. After these measurements, chlorophylls were extracted using acetone and quantified by a separate spectrophotometry as described in the Section 2.3. The extracted chlorophylls were quantified by measuring the absorbance at 665 nm, the absorption peak of chlorophyll a, the major form of chlorophyll in plant leaves. Chlorophyll b's absorption peak is at 726 nm, which is close to the upper wavelength limit of the smartphone's red pixels (750 nm) and therefore insensitive to the NDVI measurements. The smartphone-acquired NDVI values were plotted against the extracted chlorophyll amounts, as shown in Figure

B-5. For all three species, strong linear correlations could be observed with R<sup>2</sup> values of 0.884–0.947, indicating the smartphone-acquired NDVI values are highly and accurately correlated to the chlorophyll amounts within plant leaves.

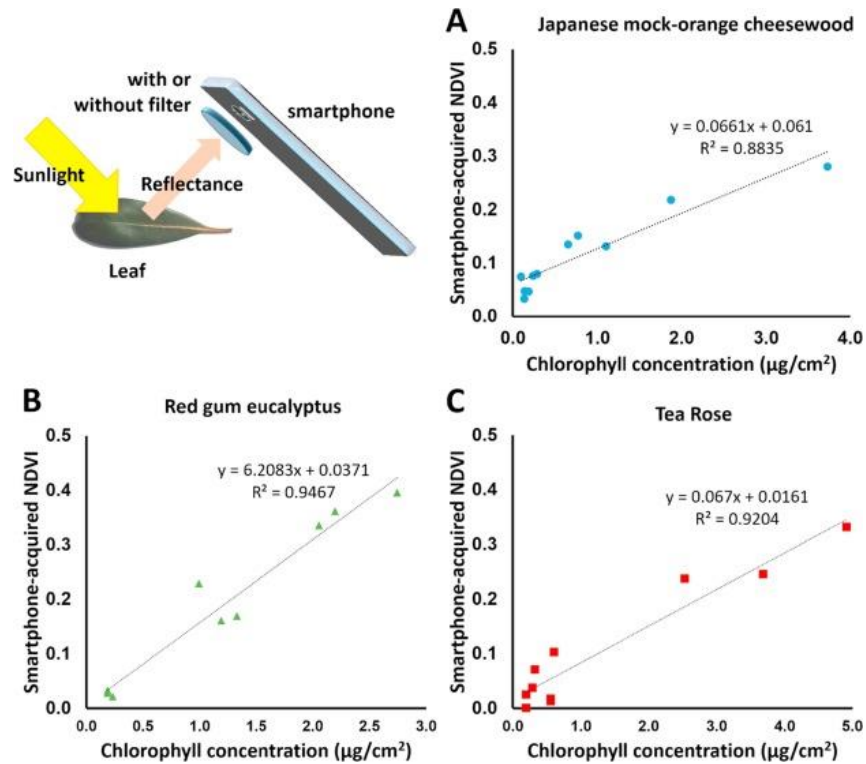


Figure B- 5. Correlation between the smartphone-acquired NDVI values and the leaf chlorophyll content. (A) Japanese mock-orange cheesewood. (B) Red gum eucalyptus.

(C) Tea rose.

### 3.4. Smartphone-acquired NDVI values vs. Water contents of plant leaves

All plant leaves were exposed to different environmental conditions and their water contents were varied substantially, from close to 0% to 60–80%, as measured by drying the leaves in an oven (described in Materials and Method).

The smartphone-acquired NVDI values were plotted against the water contents of leaves (measured by oven-drying), for three different plant species (Figure A-6). The best curve fit for these plots were Langmuir-like equation, as shown in each plot, with  $R^2$  values of 0.674, 0.974, and 0.835. This means that the NDVI values initially increased as the water content increased while they were saturated at 0.6–0.7 with 50% water content. Considering that the chlorophyll content is not directly related to the water content, these relationship and  $R^2$  values are promising in (indirectly) quantifying leaf health in association with water stress.

#### **4. Conclusion**

As described in Introduction, existing literature has found that the plant healthiness and water stress has been quantified using expensive equipment such as a NIR camera, an IR thermal imaging camera, or a hyperspectral imaging system. In addition, IR thermal imaging showed limitations in evaluating water content due to environmental temperature and humidity variations.

Our new smartphone based method does not require any additional instrumentation other than a single 800 nm high pass filter. It utilizes the smartphone's (perhaps unintended) ability in recognizing NIR, as well as the use of NVDI commonly used in monitoring vegetation index from aerial or satellite images. The presence of a linear relationship between the chlorophyll content and the NDVI values suggests that this simple method can be used as a predictor of healthiness or stress of leaves. The assay time was almost instantaneous, thus allowing inexpensive, easy-to-use, rapid, and early prediction of plant water stress that can be used for field and household applications.

## **Acknowledgements**

Funding for this work was provided by the BIO5 Institute at the University of Arizona. The authors would like to thank Mr. Austin S. Vedder, Mr. Christian M. Jennings, and Mr. Sean Perea at the University of Arizona for experimental assistance.

## **References**

- Adamsen, F. G., Pinter, P. J., Barnes, E. M., LaMorte, R. L., Wall, G. W., Leavitt, S. W., & Kimball, B. A. (1999). Measuring wheat senescence with a digital camera. *Crop Science*, 39(3), 719-724.
- Aguilar, C., Zinnert, J. C., Polo, M. J., & Young, D. R. (2012). NDVI as an indicator for changes in water availability to woody vegetation. *Ecological Indicators*, 23, 290-300.
- Blum, A. (2018). *Plant breeding for stress environments*. CRC Press: Boca Raton, FL.
- Groeneveld, D. P. (2008). Remotely-sensed groundwater evapotranspiration from alkali scrub affected by declining water table. *Journal of Hydrology*, 358(3-4), 294-303.
- Kacira, M., Ling, P. P., & Short, T. H. (2002). Machine vision extracted plant movement for early detection of plant water stress. *Transactions of the ASAE*, 45(4), 1147-1153.
- Kim, Y., Glenn, D. M., Park, J., Ngugi, H. K., & Lehman, B. L. (2011). Hyperspectral image analysis for water stress detection of apple trees. *Computers and Electronics in Agriculture*, 77(2), 155-160.
- Lichtenthaler, H. K. (1987). [34] Chlorophylls and carotenoids: pigments of photosynthetic biomembranes. *Methods in Enzymology*, 148, 350-382.

- Lorenzen, B., & Jensen, A. (1988). Reflectance of blue, green, red and near infrared radiation from wetland vegetation used in a model discriminating live and dead above ground biomass. *New Phytologist*, 108(3), 345-355.
- Meron, M., Tsipris, J., Orlov, V., Alchanatis, V., & Cohen, Y. (2010). Crop water stress mapping for site-specific irrigation by thermal imagery and artificial reference surfaces. *Precision Agriculture*, 11(2), 148-162.
- Nagler, P. L., Daughtry, C. S. T., & Goward, S. N. (2000). Plant litter and soil reflectance. *Remote Sensing of Environment*, 71(2), 207-215.
- Peñuelas, J., & Filella, I. (1998). Visible and near-infrared reflectance techniques for diagnosing plant physiological status. *Trends in Plant Science*, 3(4), 151-156.
- Rouse Jr., J. W. (1973). Monitoring the vernal advancement and retrogradation (green wave effect) of natural vegetation, Type I Progress Report – Number 7, March 28, 1974 – May 27 1973, NASA, Washington, DC. Available at: <https://ntrs.nasa.gov/archive/nasa/casi.ntrs.nasa.gov/19740022555.pdf> (accessed 2/14/2018).
- Steele, M., Gitelson, A. A., & Rundquist, D. (2008). Nondestructive estimation of leaf chlorophyll content in grapes. *American Journal of Enology and Viticulture*, 59(3), 299-305.
- Tucker, C. J. (1979). Red and photographic infrared linear combinations for monitoring vegetation. *Remote Sensing of Environment*, 8(2), 127-150.
- Wang, J., Rich, P. M., & Price, K. P. (2003). Temporal responses of NDVI to precipitation and temperature in the central Great Plains, USA. *International Journal of Remote Sensing*, 24(11), 2345-2364.

Zhao, T., Stark, B., Chen, Y., Ray, A. L., & Doll, D. (2015). A detailed field study of direct correlations between ground truth crop water stress and normalized difference vegetation index (NDVI) from small unmanned aerial system (sUAS). In: 2015 IEEE International Conference on Unmanned Aircraft Systems (ICUAS), IEEE, pp. 520-525.

## Appendix C

### Distance vs. capillary flow dynamics-based detection methods on microfluidic paper-based analytic device ( $\mu$ PAD)

Soo Chung,<sup>[a]</sup> Christian M. Jennings,<sup>[b]</sup> and Jeong-Yeol Yoon\*<sup>[a,b]</sup>

[a]Department of Biosystems Engineering The University of Arizona  
Tucson, Arizona 85721 (United States)

\*E-mail: [jyyoon@email.arizona.edu](mailto:jyyoon@email.arizona.edu)

[b] Department of Biomedical Engineering The University of Arizona  
Tucson, Arizona 85721 (United States)

Manuscript received: 01 April 2019; Manuscript revised: 27 May 2019; Manuscript  
accepted online: 03 June 2019

<https://doi.org/10.1002/chem.201901514>

© 2019 WILEY-VCH Verlag GmbH & Co. KGaA, Weinheim

## **Abstract**

In recent years, there has been a high interest in paper-based microfluidic sensors or microfluidic paper-based analytic devices ( $\mu$ PADs) towards low-cost, portable and easy-to-use sensing for chemical and biological targets.  $\mu$ PAD allows spontaneous liquid flow without any external or internal pumping as well as innate filtration capability. While both optical (colorimetric and fluorescent) and electrochemical detection have been demonstrated on  $\mu$ PADs, several limitations still remain such as the need for additional equipment, vulnerability to ambient lighting perturbation, and inferior sensitivity. In this minireview, alternative detection methods on  $\mu$ PADs are covered to resolve these issues, including the relatively well studied distance-based measurements as well as the newer capillary flow dynamics-based method. Detection principles, assay performance, strengths, and weaknesses are explained for these methods, along with their potential future applications towards point-of-care medical diagnostics and other field-based applications.

Keywords: capillary flow dynamics; machine learning; paper microfluidic; point-of-care diagnostics

## 1. Introduction

Demand for point-of-care (POC) diagnostics has steadily increased over the past couple of decades. Specifically, there is a need for POC diagnostics that is easy to fabricate, low-cost (no need for large and expensive equipment), user-friendly (no need for experienced labor), and often sufficiently sensitive, allowing early diagnosis and appropriate treatment in a timely manner.<sup>[1-4]</sup> Microfluidics can be integrated into POC diagnostic platforms to reduce reagent/sample consumption, to miniaturize the device, and to decrease the assay time.<sup>[5]</sup> Recently, paper (cellulose fibers) has become a popular substrate for microfluidic POC platforms, referred to as microfluidic paper-based analytic device ( $\mu$ PAD). Its main advantage arises from the fibrous structure of paper, allowing liquid to flow spontaneously without using external or internal pumping system.<sup>[6]</sup> The paper's fibrous structure also provides a built-in filtering capability, which is appropriate for processing complex samples such as blood. Recently, microfluidic channel layouts can be easily "printed" on paper using a commercial wax printer. A hot plate is additionally used to melt the printed wax, fill the entire thickness of the paper, and form a hydrophobic barrier.<sup>[7]</sup> In addition, paper substrate is inexpensive, easy to store, and lightweight for easy transportation.<sup>[8,9]</sup> Due to these advantages, it has recently gained popularity in many analytical and clinical assays and diagnostics.<sup>[10,11]</sup>

Lateral flow immunochromatographic assay, or simply lateral flow assay (LFA) is considered a precursor to  $\mu$ PAD. On an LFA, a biological specimen flows through a paper substrate where antibody-antigen reactions occur (i.e., immunoassays). A well-known example of LFA is a colorimetric pregnancy test.<sup>[12]</sup> In LFA, a biological specimen (e.g. urine or blood) is loaded to its sample loading area (inlet). The target protein (antigen) first

binds to an antibody that is typically conjugated with gold nanoparticles. This antigen-antibody-gold nanoparticle conjugate flows through the paper strips by capillary action and then reaches the detection area where “capture” antibodies (the same antibody to the target) are immobilized. Antigen-antibody-gold nanoparticle conjugates are captured on the detection area and generate a characteristic pink band (arising from gold nanoparticles), indicating a positive target presence in the sample. While this method generally provides qualitative result, i.e., yes/no assay,<sup>[13]</sup> there have been attempts to quantify the color intensity of these pink bands through colorimetric detection.<sup>[14–17]</sup> However, it is not an easy task to obtain reproducible signals from such attempts since they are sensitive to the surrounding environment, including ambient light, humidity, and/or temperature.<sup>[18–20]</sup> LFAs, in general, can detect only high concentrations of target due to this environmental perturbation, as well as the opaque and optically non-homogeneous nature of paper fibers. Fluorescence detection has been suggested to resolve these issues, especially to lower the limit of detection.<sup>[21–25]</sup> However, it requires a special optical detection setup, including optical filters, a monochromatic light source such as a laser, detection at a specific angle to pick up only fluorescent emission, etc. While fluorescence detection, when compared to colorimetric detection, offers a lower limit of detection, it is still sensitive to the surrounding environment especially lighting perturbations.<sup>[26,27]</sup>

Electrochemical detection has been also suggested as an alternative to colorimetric and fluorescence detection, where the change in voltage (potentiometric), current (amperometric), or conductance (conductometric) is measured for detecting electrolyte ions ( $\text{Cl}^-$ ,  $\text{K}^+$ ,  $\text{Na}^+$  and  $\text{Ca}^{2+}$ )<sup>[28]</sup> or enzyme – target substrate binding such as glucose, lactate, ethanol, and uric acid.<sup>[29,30]</sup> Since their changes can be related to the target concentration,

it is necessary to pattern three electrodes (counter, reference, and working) onto the paper substrate, which can be printed using conductive inks.<sup>[29,30]</sup> While small electrochemical detectors are available, their accuracy and sensitivity are inferior to the optical detectors of comparable sizes.<sup>[28]</sup> Therefore, a potentiostat is necessary to generate sufficiently sensitive assay results, which is often bulky and very expensive.

The most promising method appropriate for POC diagnostics and field-based assays is the distance-based measurement on LFA or  $\mu$ PAD. In this method, the length of color development or final flow distance on a paper strip is measured to correlate it to the target concentration.<sup>[31-51]</sup> In the distance-based methods, it is possible to implement different sensing modalities over multiple channels since only the distance is measured. Ambient lighting perturbation is no longer an issue as it measures neither colorimetric nor fluorescence intensities. Additionally, complicated patterning of electrodes is unnecessary. For these reasons, distance-based methods have become increasingly popular in paper-based platforms (LFA and  $\mu$ PAD).

In this mini-review, we briefly summarize various distance-based methods on LFA or  $\mu$ PAD, classified by the type of target molecules and subsequent detection methods. Most distance-based methods measure the final length of color development or the final distance of flow. However, more information on samples can be obtained through acquiring the real-time profile of flow rate changes, as capillary action through paper pores induces chromatographic separation of molecules. In addition, there is no need to wait until the capillary action-driven flow is finished, which may also decrease the assay time significantly. We will highlight the strength of this capillary flow dynamics-based method as an alternative to the distance-based methods to improve the assay performance.

## 2. Distance-based detection on LFA or $\mu$ PAD

In distance-based methods, the final length of color development or the final flow distance is measured and is correlated to the target concentration. Liquid sample flows through the paper pore spontaneously via capillary action once it is introduced onto the inlet of LFA or  $\mu$ PAD. Measurement of the final length of color development is the simplest and the most popular method. In such methods, paper substrate is pre-deposited with reagents, including bioreceptor (antibody, enzyme, nucleic acid, etc.) and colorimetric dye. As a sample solution flows through a paper strip, target molecules react with the pre-deposited reagents and develop coloration as shown in Figure C-1. Once all target molecules are consumed, there is no further coloration development while the sample continues to flow to the end. The length of such coloration is then correlated to the target concentration.

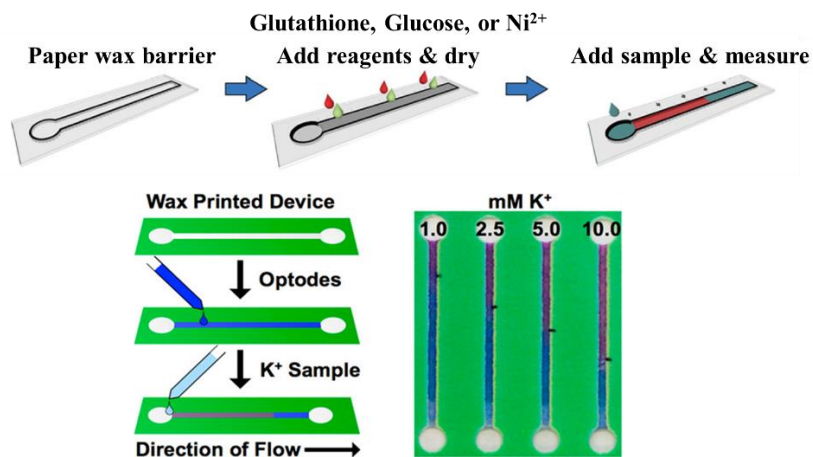


Figure C-1. The length of color development on  $\mu$ PAD is correlated to the target concentration of small chemicals such as glutathione, glucose, or  $\text{Ni}^{2+}$  (top) and  $\text{K}^{+}$  (bottom). Reprinted from [31] with permission. (C) 2013 Royal Society of Chemistry.

Reprinted from [39] with permission. (C) 2018 American Chemical Society.

For example, Cate et al.<sup>[31]</sup> utilized a distance-based  $\mu$ PAD to quantify glucose. In this study, glucose oxidase, 3,3'-diaminobenzidine (DAB), and peroxidase were pre-deposited onto the paper substrate to allow for color development. As glucose flowed through the paper substrate, the glucose reacted with glucose oxidase to form hydrogen peroxide, which reacted with DAB and peroxidase. This reaction generated a brown, insoluble product, allowing for quantification of glucose with a limit of detection of 11 mg/dL and an assay time of 5 minutes. Such coloration-distance measurements have been demonstrated for many different targets, as summarized in Table 1.

Table C-1. Summary of distance-based assays on  $\mu$ PADs.

Target	Detects:	LOD	Assay time	Ref.
<u>Heavy metals:</u>				
Ni	Color	40 mM	15 min	[31]
Cl	Color	2 ppm	30 min	[32]
Cu <sup>2+</sup>	Color	1 ppm	30 min	[33]
Cu <sup>2+</sup>	Color	1 ppm	Not stated	[34]
Cu	Color	20 ppb	30 min	[35]
Fe <sup>3+</sup>	Color	20 ppb	570 min	[36]
Ni <sup>2+</sup> , Cu <sup>2+</sup> , Fe <sup>2+</sup>	Color	1-5 $\mu$ g	40 min	[37]
Cu <sup>2+</sup> , Fe <sup>2+</sup> , Fe <sup>3+</sup> , Zn <sup>2+</sup>	Color	0.1 ppm	3 min	[38]
K <sup>+</sup>	Color	1.0-4.3 mM	5 min	[39]
Hg	Color	0.93 $\mu$ g/mL	10 min	[40]
Co	Color	0.5 mg/L	Not stated	[41]
<u>Small chemicals:</u>				
Glucose	Color	11 mg/dL	5 min	[31]
Cocaine	Color	3.8 $\mu$ M	30 min	[42]
Cocaine	Color	1.8 $\mu$ M	30 min	[43]
<u>Nucleic acids:</u>				
DNA	Flow dist.	10 $\mu$ M	<5 min	[44]
ssDNA oligomer	Flow dist.	10 nM	15 min	[45]

dsDNA	Color	4 nM	6 min	[46]
E. coli DNA	Color	4x10 <sup>3</sup> /μL	5 min	[47]
Adenosine	Color	20 μM	30 min	[43]
<u>Proteins &amp; others:</u>				
Albumin, lipoprotein	Flow dist.	100 mg/dL	<5 min	[44]
CEA	Color	5 ng/mL	15 min	[48]
Lactoferrin	Color	0.1 mg/mL	<10 min	[49]
Alkaline phosphatase	Flow dist.	0.075 U/mL	Not stated	[50]
Hematocrit	Flow dist.	<57%	30 min	[51]
Glutathione	Color	0.012 nM	10 min	[31]

Instead of quantifying the length of coloration, the flow distance has been recently utilized. Chen et al.<sup>[44]</sup> used amphiphilic property of target. In this study, a sample solution containing amphiphilic target was placed into the hydrophilic channel. As the target flowed through the channel, its hydrophobic tail adsorbed to the wax barrier while the hydrophilic head faced towards water in the hydrophilic channel. A higher concentration of amphiphilic target resulted in more adsorption to the wax barrier and a reduced final flow distance. Additionally, high amphiphilic target concentration caused a part of the solution to leak to the wax barrier and resulted in a decrease in flow distance (Figure C-2 in the top). DNA, bovine serum albumin (BSA), human albumin, and low-density lipoprotein were detected with this method, with the limits of detection of 10 μM, 100 mg/dL, 100 mg/dL, and 125 mg/dL, respectively. The assay time was 5 minutes.

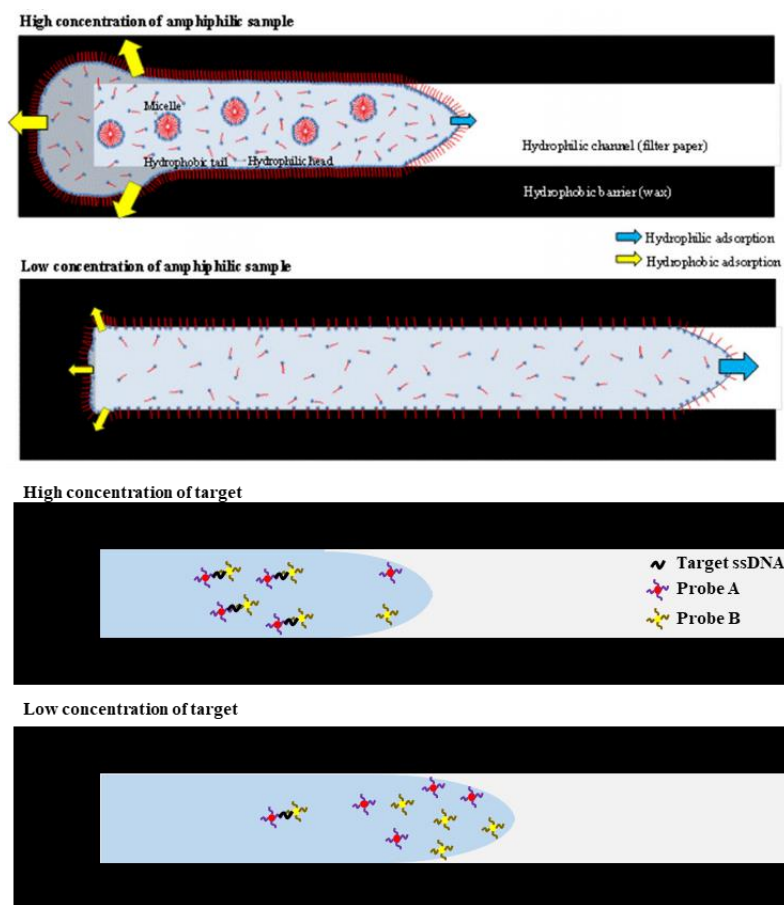


Figure C-2. The flow distance on  $\mu$ PAD is correlated to the target concentration. Top: amphiphilic target molecules leak into the wax barrier, reducing the final flow distance.

Reprinted from [44] with permission. (C) 2015 Springer Science Business Media.

Bottom: target ssDNA results in aggregation of particles, reducing the final flow distance.

Kalish et al.<sup>[45]</sup> pre-deposited two colored microspheres conjugated with one ssDNA (single-stranded DNA) probe onto the paper substrate. Each ssDNA probe's sequence was half complementary to the target ssDNA sequence, such that in the presence of the target ssDNA, a three-unit aggregate formed. Due to the paper pores, this aggregate was inhibited from wicking along the channel and a reduced flow distance was observed

(Figure C-2 in the bottom). Without the presence of target ssDNA, wicking was not inhibited, leading to maximum flow distance. The final flow distance in the channel was then observed via the microsphere coloration. The device has a limit of detection of 10 nM with an assay time of 15 minutes.

There are many advantages of using a distance-based measurement compared to optical or electrochemical detection, as described in the Introduction. Quantification is easily made even with the naked eye, without the need for bulky equipment. Some advantages are that it is not severely affected by ambient lighting perturbations, complicated electrode patterning is not required, and it provides a low-cost and user-friendly platform appropriate for POC diagnostics and field-based assays.

Despite these advantages, several limitations still exist in distance-based methods. Specifically, the distance of flow can be affected by how the sample is loaded. The pressure applied to the  $\mu$ PAD's inlet can be significantly varied depending on the method of sample loading, e.g. pipetting. Such variation in external pressure can affect the flow rate, according to the Darcy's equation. Darcy's equation describes the capillary flow in a porous media and it explains the relation between the pressure gradient and the flow rate of a liquid. The total discharge ( $Q$ ) is derived from intrinsic permeability of the medium ( $k$ ), cross-sectional area to flow ( $A$ ), and the pressure gradient ( $P_b - P_a$ ) divided by the dynamic viscosity of liquid ( $\mu$ ) and length across the pressure drop ( $L$ ), as represented in Eq. (1). When external pressure is applied via pipetting, it will affect the flow, as  $P_a$  will increase (or decrease if the external pressure is negative).

$$Q = -\frac{kA(P_b - P_a)}{\mu L} \quad (1)$$

In addition, the distance can be also affected by environmental humidity. While the humidity term is not included in the Darcy's equation, humidity does affect the evaporation time, which may shorten the flow distance prematurely. Most importantly, the user should wait until the flow is fully developed, leading to substantially long assay time (up to 40 min) as summarized in Table 1. A better alternative is to monitor the time-dependent changes of flow rates from  $\mu$ PADs, i.e. capillary flow dynamics, as described in the next section.<sup>[52]</sup>

### **3. Capillary flow dynamics-based detection on LFA or $\mu$ PAD**

As a precursor to capillary flow dynamic-based method, Phillips et al.<sup>[53]</sup> demonstrated a method that can quantitatively analyze active enzyme such as alkaline phosphatase and  $\beta$ -D-galactosidase using 'time' difference caused by variations in flow rate through paper. It works as a bridge between distance-based method and capillary flow dynamics-based method. They measured the time difference between the generation of green color on the control region compared to an assay region in the paper chip shown in Figure C-3.

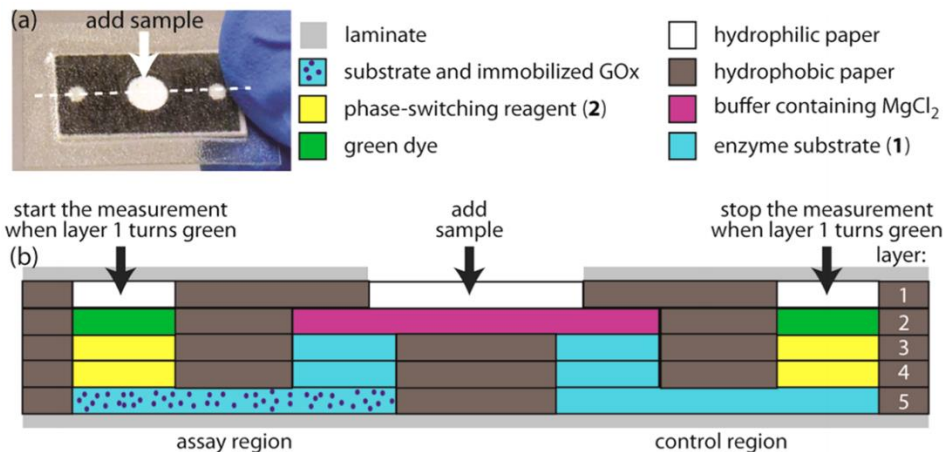


Figure C-3. Variations in the flow rates on  $\mu$ PAD are correlated to the target enzyme concentration. (a) Photograph of  $\mu$ PAD for quantifying active enzyme analytes. (b) Schematic diagram of stacked layers of paper. Reprinted from [53] with permission. (C) 2013 American Chemical Society.

In their experimental set-up, target enzyme analyte reacts with substrate and releases glucose (blue-colored areas in layers 3 and 4). Then, in the assay region, the glucose encounters the glucose oxidase and releases hydrogen peroxide (blue area in layer 5). Hydrogen peroxide encounters the oligomer which makes the paper hydrophobic (yellow areas in layers 3 and 4). Hydrogen peroxide alters the oligomer to hydrophilic products, which causes the paper to become hydrophilic so that the solution flows faster to layer 2 to generate a green color to layer 1. However, in the control region, glucose cannot generate hydrogen peroxide due to the absence of glucose oxidase. Therefore, the oligomer remains hydrophobic and the time to pass the yellow areas in layers 3 and 4 takes longer. Hence, the larger the time difference to green color generation between control region and assay region represent a higher concentration of target. This is because the reaction time is

dependent on the concentration of hydrogen peroxide which causes a difference in flow rate by changing the properties of the paper from hydrophobic to hydrophilic.

Capillary flow dynamics-based method has been recently demonstrated on  $\mu$ PAD by Klug et al.,<sup>[52]</sup> where the time-dependent changes of flow rates (capillary flow dynamics) were monitored in real-time from a video acquired via smartphone. Antibody-conjugated submicron polystyrene particles were pre-loaded to a  $\mu$ PAD, and two different pathogenic targets, *Escherichia coli* K12 and Zika virus (ZIKV) were assayed. Without target presence, particles do not aggregate, and diffuse to the wetting front (liquid-air interface; shown in Figure C-4) as they are relatively hydrophobic. Adsorption of such particles to the wetting front changes the interfacial tension and slows down the capillary flow rate accordingly. With presence of target, antibody-conjugated particles become immunoagglutinated through antibody-antigen binding. As these agglutinated particles diffuse to the wetting front much slower than non-agglutinated particles, the capillary flow rate increases but not as quickly as that with no particles. Therefore, particles function as a signal transducer that allows real-time monitoring of the extent of particle immunoagglutination, and subsequently the presence of target and its concentration.

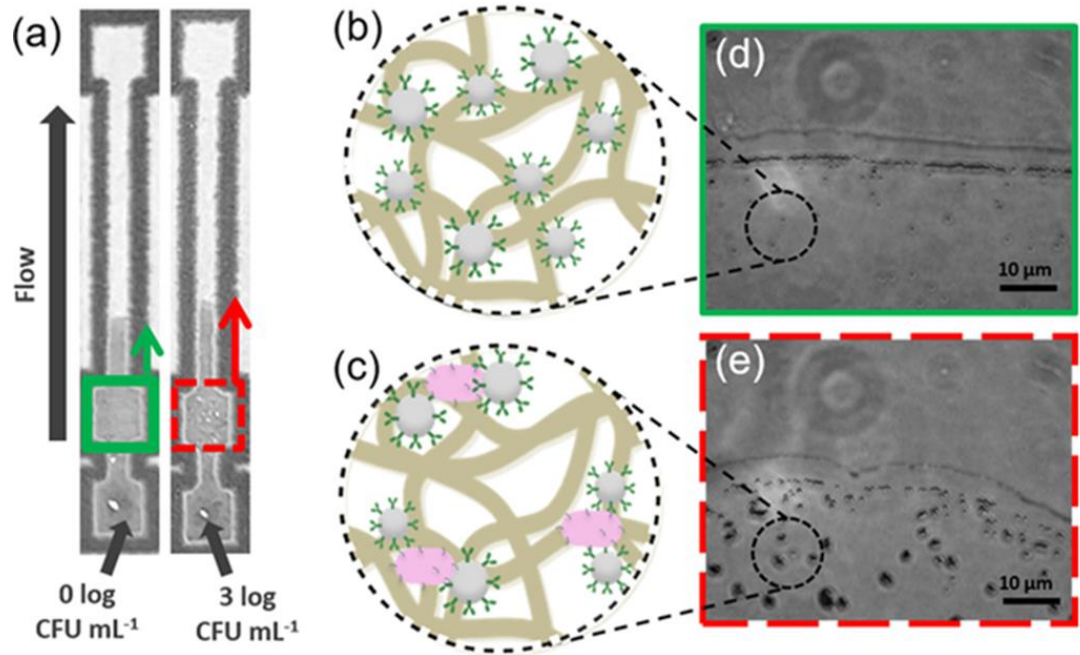


Figure C-4. Conceptual diagram of the capillary flow dynamics transducer mechanism.

(a) Incremental changes in capillary flow rates of antibody-conjugated particles are observed with different target pathogen (*E. coli* K12) concentrations. (b) Particles are monodisperse in the absence of target, (c) and become immunoagglutinated upon antibody-antigen binding. (d–e) This manifests in higher or lower particle diffusion toward the wetting front, respectively, which influences wetting front interfacial properties. Reprinted from [52] with permission. (C) 2018 John Wiley & Sons.

Klug et al.<sup>[52]</sup> modeled the capillary flow dynamics using the Lucas-Washburn (L-W) capillary flow model, as represented in Eq. (2),<sup>[54,55]</sup> modified with Cassie-Baxter non-homogenous wetting assumptions. With no externally applied pressure, the pressure difference in Darcy's equation can be expressed in terms of the interfacial tension at the wetting front ( $\gamma_{LG}$ ) and the contact angle at the wetting front ( $\theta$ ), i.e. the capillary pressure. The apparent contact angle ( $\theta^*$ ) is used instead of true contact angle, which is a function

of the surface roughness ( $r_f$ ) and wetted fraction ( $f$ ) following Cassie-Baxter assumption. The force balance between inertia force (by capillary pressure) and viscous force (represented by the dynamic viscosity of liquid  $\mu$ ) can be related to the horizontal capillary flow represented by the incremental flow distance ( $l$ ) over time ( $t$ ). The capillary radius ( $R$ ) can be replaced with the paper pore size.

$$\frac{l^2}{t} \propto \frac{R \gamma_{LG} \cos \theta}{2\mu} \quad (2)$$

The change in capillary flow dynamics has been successfully utilized to detect and quantify target, with the LOD of 10 CFU/mL for *E. coli* K12 in water samples and 20 pg/mL for Zika virus in serum samples. Since a change in flow rate can be observed almost immediately after loading samples, there was no need to wait until the flow was fully developed. In fact, the assay time was as short as 30 seconds.

While this method was demonstrated for detecting a single target, where the flow rates at a fixed time were measured, it opens up a door for assaying complicated samples that contain multiple target and non-target molecules. As  $\mu$ PAD is essentially a paper chromatography, separation and retention of different target and non-target molecules are expected as the liquid sample flows through paper pores. As a result, the moving front may not travel at a constant speed, as molecular separation and retention should affect the diffusion and adsorption of such molecules in a complicated manner. The flow rate of a moving front can be plotted over time, i.e. flow rate profile, which can be used to qualitatively and quantitatively detect multiple targets. Figure C-5 shows an example of such case – it is made-up based on our preliminary data from a mixture of organic

molecules travelling through a paper substrate. Each molecule should interact differently with paper fibers, and as a result, their diffusion towards the wetting front would be varied over time. A sudden change in flow rate can be correlated to the presence of specific target and potentially quantified.

Furthermore, it will be also possible to analyze different types of targets in a single channel that contains multiple detection zones. In each detection zone, different antibodies or receptors are pre-loaded (Figure C-6). As the mixture flows through this channel, a certain target molecule should interact with and be accordingly retained at a specific detection zone, generating a unique flow rate profile.

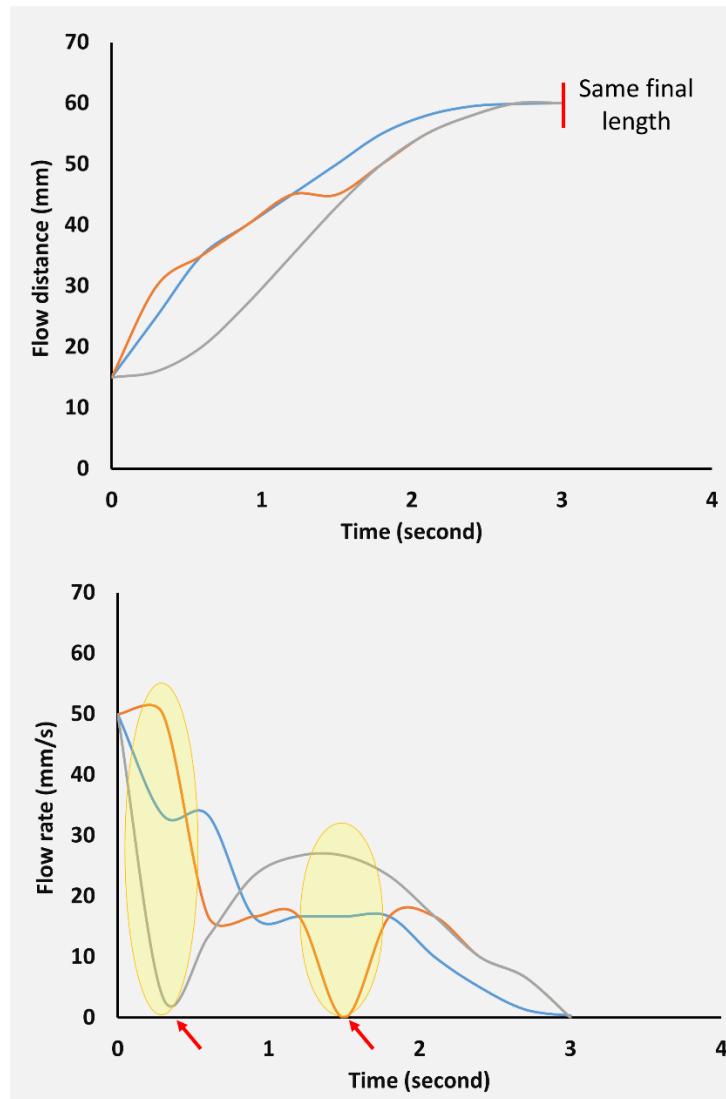


Figure C-5. A made-up example of real-time monitoring of flow rate, e.g. capillary flow dynamics-based detection of multiple target molecules. The flow distance is varied by different target molecules, where the final distances are the same (top). The plot of flow rate vs. time can be used to identify the presence of certain target molecule(s) (bottom).

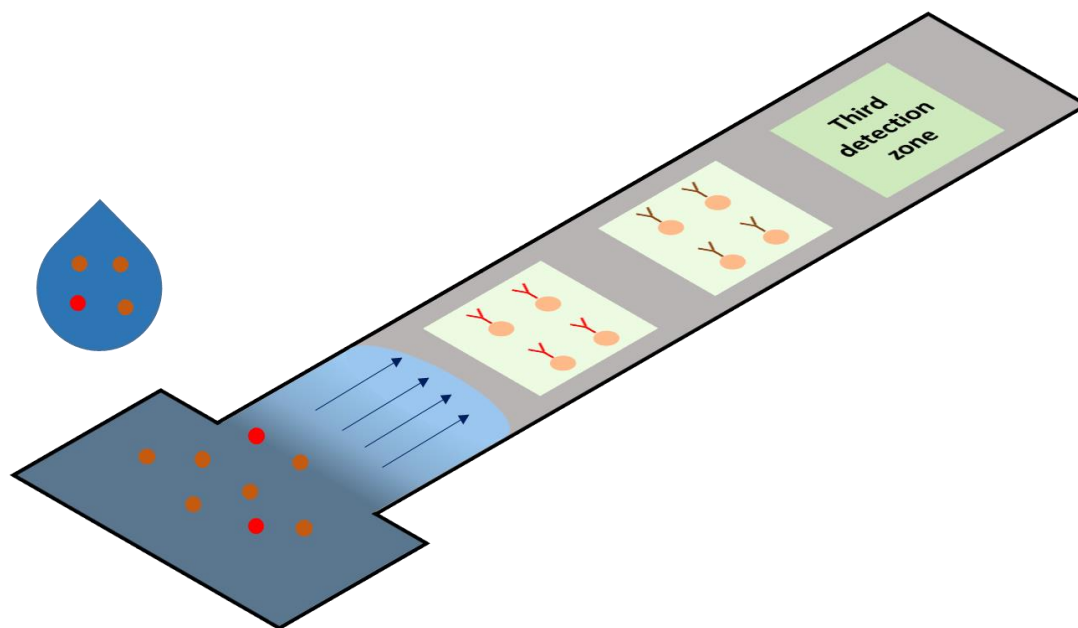


Figure C-6. A  $\mu$ PAD with multiple detection zone for capillary flow dynamics-based detection. Each detection zone is pre-loaded with the antibody-conjugated particles targeting different protein molecules.

Machine learning algorithms and statistical inference methods have recently become popular for their ability to handle a large amount of data (“big data”), and their application to this method would strengthen it. A large number of flow rate profiles can be collected and analyzed with these methods, for example, principal component analysis (PCA) or support vector machine (SVM). With these methods and a large amount of flow rate profile data, a predictive model can be developed from iterative training on experimental measurements. These methods are quite different from the distance-based methods where each experiment generates only one data point, whereas the capillary flow dynamics-based method has the potential to generate a large dataset, which can be trained to generate more accurate model with higher positive classification of new input values.

### **3. Conclusion**

Paper microfluidic devices or microfluidic paper-based analytic devices ( $\mu$ PADs) have been popularly fabricated and demonstrated for sensing chemical and biological targets as low-cost, simple, portable, and disposable alternatives to silicone- or glass-based microfluidic devices. As discussed, optical (colorimetric and fluorescent) and electrochemical detection methods on  $\mu$ PADs are limited by factors such as inferior sensitivity, vulnerability to ambient lighting perturbation, or the need for additional equipment to construct the detection system. Distance-based measurement has emerged as an alternative that is easy to monitor and unaffected by ambient lighting conditions. As an improvement to these distance-based measurements, we propose to use capillary flow dynamics that will further improve the sensitivity, significantly reduce the assay time, and enable the analysis of complicated mixture. This method can be further strengthened by machine learning algorithms and statistical inference methods. Combined with smartphone or microcontroller detection, these methods can be easily automated and commercialized such that they can be used by a layperson.

## Acknowledgements

The authors acknowledge financial support from Korea Institute of Ocean Science and Technology (KIOST), Republic of Korea. CMJ acknowledges financial support from Environmental Health Sciences Transformative Research Undergraduate Experience (EHS-TRUE) at the University of Arizona.

## References

- [1] G. A. Posthuma-Trumpie, J. Korf, A. van Amerongen, *Anal. Bioanal. Chem.* **2009**, *393*, 569–582.
- [2] P. Yager, T. Edwards, E. Fu, K. Helton, K. Nelson, M. R. Tam, B. H. Weigl, *Nature* **2006**, *442*, 412–418.
- [3] D. A. Giljohann, C. A. Mirkin, *Nature* **2009**, *462*, 461–464.
- [4] G. Gauglitz, *Annu. Rev. Anal. Chem.* **2014**, *7*, 297–315.
- [5] S. K. Sia, L. J. Kricka, *Lab Chip* **2008**, *8*, 1982–1983.
- [6] A. W. Martinez, S. T. Phillips, G. M. Whitesides, E. Carrilho, *Anal. Chem.* **2010**, *82*, 3–10.
- [7] E. Carrilho, A. W. Martinez, G. M. Whitesides, *Anal. Chem.* **2009**, *81*, 7091–7095.
- [8] K. Scida, B. Li, A. D. Ellington, R. M. Crooks, *Anal. Chem.* **2013**, *85*, 9713–9720.
- [9] A. K. Yetisen, M. S. Akram, C. R. Lowe, *Lab Chip* **2013**, *13*, 2210–2251.
- [10] W. Dungchai, O. Chailapakul, C. S. Henry, *Analyst* **2011**, *136*, 77–82.
- [11] S. M. Z. Hossain, R. E. Luckham, A. M. Smith, J. M. Lebert, L. M. Davies, R. H. Pelton, C. D. M. Filipe, J. D. Brennan, *Anal. Chem.* **2009**, *81*, 5474–5483.
- [12] P. von Lode, *Clin. Biochem.* **2005**, *38*, 591–606.

- [13] W. Zhao, M. M. Ali, S. D. Aguirre, M. A. Brook, Y. Li, *Anal. Chem.* **2008**, *80*, 8431–8437.
- [14] A. W. Martinez, S. T. Phillips, M. J. Butte, G. M. Whitesides, *Angew. Chem. Int. Ed.* **2007**, *46*, 1318–1320.
- [15] W. Wang, W.-Y. Wu, W. Wang, J.-J. Zhu, *J. Chromatogr. A* **2010**, *1217*, 3896–3899.
- [16] S. A. Klasner, A. K. Price, K. W. Hoeman, R. S. Wilson, K. J. Bell, C. T. Culbertson, *Anal. Bioanal. Chem.* **2010**, *397*, 1821–1829.
- [17] A. W. Martinez, S. T. Phillips, E. Carrilho, S. W. Thomas, H. Sindi, G. M. Whitesides, *Anal. Chem.* **2008**, *80*, 3699–3707.
- [18] S. Cho, T. S. Park, T. G. Nahapetian, J.-Y. Yoon, *Biosens. Bioelectron.* **2015**, *74*, 601–611.
- [19] S. P. Johnston, M. M. Ballard, M. J. Beach, L. Causer, P. P. Wilkins, *J. Clin. Microbiol.* **2003**, *41*, 623–626.
- [20] M. L. Wilson, L. Gaido, *Clin. Infect. Dis.* **2004**, *38*, 1150–1158.
- [21] Z. Li, Y. Wang, J. Wang, Z. Tang, J. G. Pounds, Y. Lin, *Anal. Chem.* **2010**, *82*, 7008–7014.
- [22] J. Yu, L. Ge, J. Huang, S. Wang, S. Ge, *Lab Chip* **2011**, *11*, 1286–1291.
- [23] J. A. Hansen, J. Wang, A.-N. Kawde, Y. Xiang, K. V. Gothelf, G. Collins, *J. Am. Chem. Soc.* **2006**, *128*, 2228–2229.
- [24] Y. Wang, L. Ge, P. Wang, M. Yan, S. Ge, N. Li, J. Yu, J. Huang, *Lab. Chip* **2013**, *13*, 3945–3955.

- [25] M. Wu, Q. Lai, Q. Ju, L. Li, H.-D. Yu, W. Huang, *Biosens. Bioelectron.* **2018**, *102*, 256–266.
- [26] J. R. Choi, J. Hu, S. Feng, W. A. B. Wan Abas, B. Pinguang-Murphy, F. Xu, *Biosens. Bioelectron.* **2016**, *79*, 98–107.
- [27] K. E. McCracken, S. V. Angus, K. A. Reynolds, J.-Y. Yoon, *Sci. Rep.* **2016**, *6*, 27529.
- [28] W.-J. Lan, X. U. Zou, M. M. Hamed, J. Hu, C. Parolo, E. J. Maxwell, P. Bühlmann, G. M. Whitesides, *Anal. Chem.* **2014**, *86*, 9548–9553.
- [29] W. Dungchai, O. Chailapakul, C. S. Henry, *Anal. Chem.* **2009**, *81*, 5821–5826.
- [30] Z. Nie, F. Deiss, X. Liu, O. Akbulut, G. M. Whitesides, *Lab Chip* **2010**, *10*, 3163–3169.
- [31] D. M. Cate, W. Dungchai, J. C. Cunningham, J. Volckens, C. S. Henry, *Lab Chip* **2013**, *13*, 2397–2404.
- [32] K. Phoosawat, N. Ratnarathorn, C. S. Henry, W. Dungchai, *Analyst* **2018**, *143*, 3867–3873.
- [33] R. Pratiwi, M. P. Nguyen, S. Ibrahim, N. Yoshioka, C. S. Henry, D. H. Tjahjono, *Talanta* **2017**, *174*, 493–499.
- [34] G. C. Bandara, C. A. Heist, V. T. Remcho, *Anal. Chem.* **2018**, *90*, 2594–2600.
- [35] C. W. Quinn, D. M. Cate, D. D. Miller-Lionberg, T. Reilly, J. Volckens, C. S. Henry, *Environ. Sci. Technol.* **2018**, *52*, 3567–3573.
- [36] Y. Shimada, T. Kaneta, *Anal. Sci.* **2018**, *34*, 65–70.
- [37] D. M. Cate, S. D. Noblitt, J. Volckens, C. S. Henry, *Lab Chip* **2015**, *15*, 2808–2818.

- [38] J. C. Hofstetter, J. B. Wydallis, G. Neymark, T. H. R. Iii, J. Harrington, C. S. Henry, *Analyst* **2018**, *143*, 3085–3090.
- [39] C. T. Gerold, E. Bakker, C. S. Henry, *Anal. Chem.* **2018**, *90*, 4894–4900.
- [40] L. Cai, Y. Fang, Y. Mo, Y. Huang, C. Xu, Z. Zhang, M. Wang, *AIP Adv.* **2017**, *7*, 085214.
- [41] M. Rahbar, P. N. Nesterenko, B. Paull, M. Macka, *Anal. Chem.* **2017**, *89*, 11918–11923.
- [42] X. Wei, T. Tian, S. Jia, Z. Zhu, Y. Ma, J. Sun, Z. Lin, C. J. Yang, *Anal. Chem.* **2016**, *88*, 2345–2352.
- [43] T. Tian, Y. An, Y. Wu, Y. Song, Z. Zhu, C. Yang, *ACS Appl. Mater. Interfaces* **2017**, *9*, 30480–30487.
- [44] Y.-T. Chen, J.-T. Yang, *Biomed. Microdev.* **2015**, *17*, 52.
- [45] B. Kalish, J. Luong, J. Roper, C. Beaudette, H. Tsutsui, in *2017 IEEE 12th Int. Conf. NanoMicro Eng. Mol. Syst (NEMS)*, **2017**, pp. 337–341.
- [46] A. G. Wang, T. Dong, H. Mansour, G. Matamoros, A. L. Sanchez, F. Li, *ACS Sens.* **2018**, *3*, 205–210.
- [47] I. Hongwarittorn, N. Chaichanawongsaroj, W. Laiwattanapaisal, *Talanta* **2017**, *175*, 135–142.
- [48] Y. Chen, W. Chu, W. Liu, X. Guo, *Sens. Actuat. B* **2018**, *260*, 452–459.
- [49] K. Yamada, T. G. Henares, K. Suzuki, D. Citterio, *ACS Appl. Mater. Interfaces* **2015**, *7*, 24864–24875.
- [50] L. Zhang, J. Nie, H. Wang, J. Yang, B. Wang, Y. Zhang, J. Li, *Anal. Meth.* **2017**, *9*, 3375–3379.

- [51] S. B. Berry, S. C. Fernandes, A. Rajaratnam, N. S. DeChiara, C. R. Mace, *Lab Chip* **2016**, *16*, 3689–3694.
- [52] K. E. Klug, K. A. Reynolds, J.-Y. Yoon, *Chem. Eur. J.* **2018**, *24*, 6025–6029.
- [53] G. G. Lewis, J. S. Robbins, S. T. Phillips, *Anal. Chem.* **2013**, *85*, 10432–10439.
- [54] K. Li, D. Zhang, H. Bian, C. Meng, Y. Yang, *Sci. Rep.* **2015**, *5*, 14085.
- [55] J. Hyväluoma, P. Raiskinmäki, A. Jäsberg, A. Koponen, M. Kataja, J. Timonen, *Phys. Rev. E* **2006**, *73*, 036705.

## Appendix D

### **Classifying the origins of oil samples using Raspberry Pi and paper microfluidic chip**

Soo Chung<sup>1</sup>, Christian M. Jennings<sup>2</sup>, Sean Perea<sup>3</sup>, Un Hyuk Yim<sup>4</sup>, and Jeong-Yeol Yoon<sup>1,2\*</sup>

<sup>1</sup>Department of Biosystems Engineering, <sup>2</sup>Department of Biomedical Engineering,

<sup>3</sup>Department of Chemical and Environmental Engineering, The University of Arizona, Tucson, Arizona 85721, United States, and <sup>4</sup>Oil and POPs Research Group, Korea

Institute of Ocean Science and Technology, Geoje 53201, Republic of Korea,

\*Corresponding author. E-mail address: [jyyoon@email.arizona.edu](mailto:jyyoon@email.arizona.edu)

Manuscript in preparation

## **ABSTRACT**

In recent years, the number of oil spill incidences in sea have been increasing around the world. The analyses of the components from the leaked crude oil are used to trace their origin. Immediate analysis in the field is required to identify the oil tanker responsible for the leak before their departure from port. However, current laboratory equipment is typically too large and delicate to use in the field. Therefore, there is a need for an on-site applicable device which permits the classification of the origins of crude oils. In this research, we attempted to use a commercial single board computer (Raspberry Pi) and paper microfluidic chip to classify the oil samples. We loaded ten different diluted oil samples on microfluidic chips to show how the differences in each oil's components resulted in different flow rates through the paper. A real-time video clip was captured with a Raspberry Pi camera and the first 1 second was divided into 25 frames to obtain the flow rate profile. The entire flow rate profiles were analyzed by principal component analysis (PCA) and t-distributed stochastic neighbor embedding (t-SNE), as well as a statistical classification model developed with support vector machine (SVM). Basrah and Iranian crude oil samples, which have similar chemical components, were recognized as related oils whereas Pyreness crude oil was contrastingly different from the other two. Marine fuel oils and lubricant oils were also distinguished according to its composition. The assay took less than few seconds and required only Raspberry Pi and paper microfluidic chip. This simple and inexpensive device allows field-applicable prediction of origins of oil samples.

*Keywords:* Crude oil, Raspberry Pi, Paper microfluidic chip, Flow rate, PCA, t-SNE, SVM

## 1. Introduction

Oil leaking (e.g., crude, fuel, or lubricants oil) frequently occurs all over the world from ships that are sailing or anchored in a harbor.<sup>1,2</sup> Governments have endeavored to prevent oil spills at sea, leading to reduction in large-scale oil spill accidents, while many small-scale oil spills continue to occur almost every day.<sup>2</sup> It is necessary to track down these ships early to prevent further accidents and to enforce cleanup responsibility on the ship and shipping company. The current gold standard is to collect a seawater sample, and analyze in a remote laboratory, which takes substantial amount of time and resources. Oil fingerprinting analysis can be classified into two categories, one based on spectrophotometry and the other on chromatography. Oils contain aromatic hydrocarbons and the composition of these can be predicted by UV spectrometry or Fourier transform infra-red (FTIR) spectrometry to obtain reliable information of the oils.<sup>3,4</sup> Gas chromatography-mass spectrometry (GC-MS) or gas chromatography-flame ionization detector (GC-FID) is the widely used for oil fingerprinting because of accuracy and sensitivity.<sup>5,6</sup> However, both methods typically require benchtop equipment and thus a laboratory environment, which is not appropriate for field use and is difficult for use on a ship. Therefore, there exists a strong need for field-ready fingerprinting analysis method to identify suspected oil-leaking ships.

Microfluidic chips have commonly been used for many different chemical and biological analysis. Recently, the use of a paper substrate (cellulose or nitrocellulose fibers) have become increasingly popular.<sup>7-9</sup> To create liquid flow in conventional silicon based microfluidic chips, high voltage is necessary to create electroosmotic flow or an external syringe pump to create hydrodynamic flow.<sup>10</sup> These pumping systems have also increased

the cost of microfluidic chips overall and created entry hurdles for non-experts. In paper microfluidic chips, liquid spontaneously flows through the pores of cellulose fibers without the need for high voltage or a syringe pump. Capillary action, also known as wicking, is the phenomena responsible and is the major advantage of paper microfluidic chips. Additionally, filtration effects and paper chromatography of samples are expected since liquid flows through porous fibers.<sup>11,12</sup>

In this work, we demonstrated a method to measure the flow rate of crude oil through paper-based microfluidic chips and demonstrated that different components of each oil traveled through paper pores at different rate. This phenomenon can be described in a modified Lucas-Washburn (L-W) capillary flow model (Eq. 1). The capillary flow through porous media can be derived from incremental flow distance ( $l$ ) over time ( $t$ ) to capillary pressure and inertial/viscous forces.<sup>7</sup>

$$\frac{l^2}{t} \propto \frac{R \gamma_{LG} \cos \theta}{2\mu} \quad (1)$$

Different oil would have a different viscosity ( $\mu$ ), leading to different flow rate. Most oil samples are mixtures, i.e., each oil component in a mixture will flow at a different rate, effectively separating them on paper strips. This, in turn, will alter the time-dependent flow rate profile to change in a complicated manner. This fractionation behavior was visualized with a Raspberry Pi camera and the video clip was split into frames. Using an image processing algorithm, the flow rates could be obtained over the duration of flow. The whole flow rate profile (i.e. normalized flow rate vs. time) was fed into statistical tools to find out a common pattern between similar oil samples. First, principal component

analysis (PCA) was used to effectively convert correlated variables into linearly uncorrelated variables. PCA has been used to effectively classify data by clustering between similar components.<sup>13,14</sup> Second, t-distributed stochastic neighbour embedding (t-SNE), a nonlinear dimension reduction method, was used to visualize and discover patterns that PCA may miss out.<sup>15,16</sup> Also, support vector machines (SVM), a supervised machine learning, was used to develop an estimation model that can predict the type and origin of the oils. SVM is able to classify nonlinear observations by mapping a set of training data into a higher dimension kernel space that linearizes the data set and allows for groups of observations to be distinguished by a linear hyper-plane.<sup>17</sup> This was suitable for this project since SVM effectively analyze multivariate dataset without overfitting. The developed predictive models can be applied to new data acquired from the field oil samples.

The overarching aim of this work is to investigate Raspberry Pi-based paper microfluidic chromatography to replace the laboratory equipment, towards the goal of developing a field-usable device capable of oil fingerprinting analysis.

## **2. Materials and Method**

### **2.1. $\mu$ PAD fabrication**

Paper microfluidic chips were fabricated using wax printer (ColorQube8580, Xerox Corporation; Norwalk, CT, USA). Chips were designed using SolidWorks (Dassault Systemes, SolidWorks Corporation; Waltham, MA, USA) and each channel was 1.5 mm wide and 25 mm long. Chip designs were printed with solid ink on nitrocellulose paper (Hi-Flow<sup>TM</sup> Plus Membrane, catalog number HF07502XSS; Millipore; Billerica, MA, USA) and cellulose chromatography paper (GE Healthcare, Maidstone, Kent, UK). Each

chip was cut out and placed on a hot plate at 100°C for 1 minute to melt the wax through the depth of the paper, while coating fibers evenly. Unlike other typical paper microfluidic chips, the inside of the channel was hydrophobic to allow the oil to flow through the chip.

## **2.2. Oil samples preparation**

All the oil samples were provided from the Korea Institute of Ocean Science and Technology (KIOST). Total of 10 different oil samples were used in this work: Three were crude oil samples from the Middle East Asia (Basrah and Iranian) and Australia (Pyreness), five marine fuel oils and two lubricant oils. All the oil samples are diluted at a ratio of 10:1 with heptane (SigmaAldrich) and stored at 4°C.

## **2.3. Raspberry Pi device**

The Raspberry Pi device was designed using SolidWorks (Dassault Systemes, SolidWorks Corporation; Waltham, MA, USA) to be size of 130 mm (W) x 90 mm (L) x 80 mm (H) and was printed out using 3D printer (Ultimaker 3, Ultimaker B.V.; Cambridge, MA, USA). Paper microfluidic chip channel was coated with hydrophobic wax to allow the oil to flow through the chip. The paper microfluidic chip is placed on the tray and inserted into the device. The oil sample was loaded onto the head of a paper microfluidic chip. Through capillary action, the oil sample flowed rapidly through the channel (within a few seconds) and real-time video was taken by the Raspberry Pi camera at the top of the device (Figure D-1).

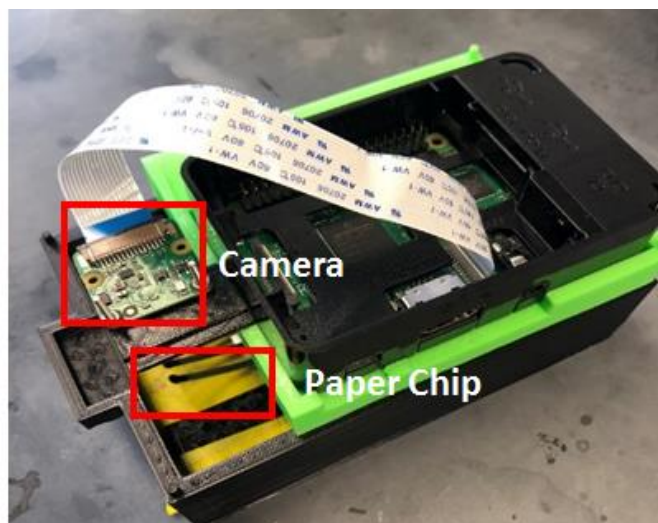


Figure D-1. Raspberry Pi device. Raspberry Pi camera positioned on the top of the paper microfluidic chips captures a video clip during capillary action-driven flow.

## 2.4. Flow rate analysis

The recorded video clip was split into each frame using MATLAB version R2019a (The Mathworks, Inc.; Natick, MA, USA) and ImageJ (U.S. National Institutes of Health; Bethesda, MD, USA) was used to measure flow distance using desktop computer to analyze the split images taken on a Raspberry Pi Camera. The color intensity changes as oil flows over existing paper microfluidic chips based on the center of the chip.

## 2.5. Statistical analysis for classification

Principal component analysis (PCA) was performed using Unscrambler 9.7 (CAMO ASA, Oslo, Norway). PCA is a linear discriminant analysis method that classify multivariate data into reduced dimension. PCA plots used 2 principal component (PC-1

and PC-2) to classify oil samples and were separated to plot the three crude oils on one plot and the remaining other oils on another plot.

*t*-distributed stochastic neighbor embedding (t-SNE) is a nonlinear dimension reduction method. This method is useful for visualizing differences in nonlinear datasets that PCA a linear dimension reduction technique could potentially miss.<sup>15</sup> Similarly, t-SNE plots were separated to plot the three crude oils on one plot and the remaining marine fuel oils on another plot. t-SNE was performed using an R open source code.

Support vector machines (SVM), is a supervised machine learning technique that classifies observations based off of an observation's location relative to a decision boundary. For this research, SVM classification was completed using the R open source code. Our SVM classification model was used to classify an oil from an input of ten sequential, flow rate observations, which accumulates together to be one data point to be classified. Additionally, our dataset is multivariate as it is composed of ten sequential flow rate observations for ten different oils, using two different paper substrates and each experimental condition was conducted in triplicate. Therefore, we were able to use one third of the dataset, randomly selected each time the program was run, as a training set with the remaining two thirds of the dataset being withheld to test the accuracy of the SVM model. The SVM algorithm was run such that there were two categories: crude oil and marine fuel oil. The "unknown" test observations would be preselected to be run in their respective categories, i.e. Basrah crude oil would be selected to be classified under the crude oil category rather than the marine fuel oil category. From this, the model would be run to classify the oil against other oils in the same category and the accuracy of the general

model was assessed by taking 30 random iterations and averaging Cohen's kappa coefficient.<sup>18</sup>

### 3. Results and Discussion

#### 3.1. Flow rate profiles

The flow rate profile was obtained by dividing the flow length from the stationary images by time, and a flow-time plot obtained. Since the oil sample is a mixture, chromatographic separation occurs as shown in Figure D-2. A significant change in flow rate was observed within the first 1 second, and it took less than 5 seconds for the sample to reach the end of the channel (Figure D-3 left). Also, when passing through a paper microfluidic chip, changes in flow rates over time show complex pattern rather than a monotonous reduction (Figure D-3 right), presumably due to chromatographic separation mentioned in the above. Three different experiments were repeated for each oil sample and paper type. Paper microfluidic chips were used once and then discarded.

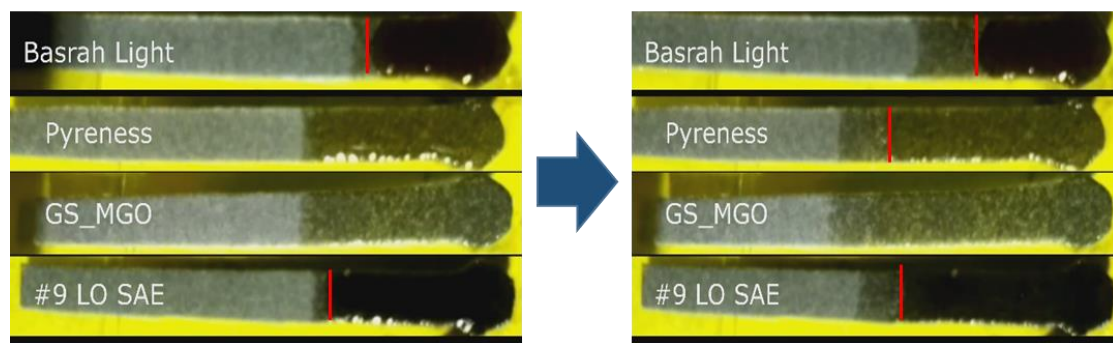


Figure D-2. Diverse flow distances at given time (1 second and 3 seconds). Separation of oil samples are indicated with red lines.

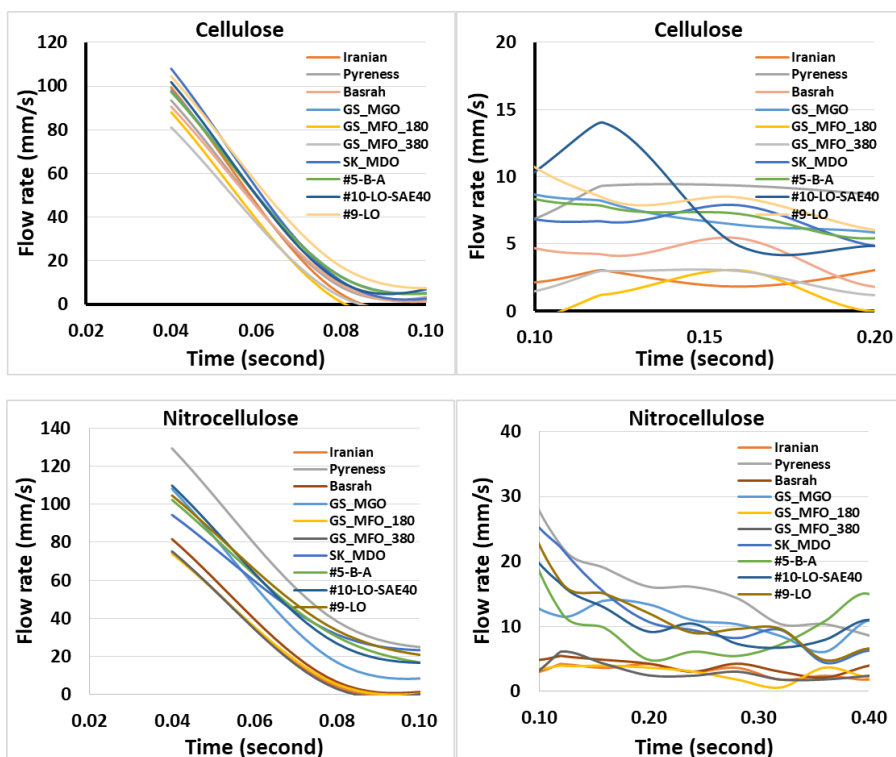


Figure D-3. Flow rate profiles for the first 0.1 second (left) or 0.1-0.4 second (right) on cellulose (top) or nitrocellulose (bottom) paper microfluidic chips

### 3.2. Oil classification by PCA

The flow rate profiles were used as input variables for the PCA analysis and converted to PCs. In the cellulose paper microfluidic chip data, PC-1 represented 95% of data for all 10 oil samples and PC-2 represented 4%. PC-1 and PC-2 represented 99% of data and used for all analyses. Among crude oil samples, Iranian and Basrah crude oil are clustered very closely while Pyreness crude oil is substantially apart from them. For the remaining oil samples, GS-180 and GS-380 (both marine fuel oils) are clustered together (colored light blue), GS-MGO, SK-MDO and B-A (also marine fuel oils) formed second

cluster (colored light green) and lubricant oils the third cluster (colored light yellow). (Figure D-4 top)

In the nitrocellulose paper microfluidic chip data, PC-1 represented 71% of data, PC-2 16%, and 87% of data were represented by two principal components (PCs). It is worth noting that the contribution of PC-2 (16%) increased significantly using a nitrocellulose-based chip while overall trends are similar to those with cellulose chips. It is possible to make a distinction among individual oil types within each clustered group, due to the increase in PC-2 contribution. For example, in the case of cellulose data, it was difficult to distinguish between GS-MGO, SK-MDO and B-A in light green clustered group, whereas such distinction is clearly possible with nitrocellulose data (Figure D-4 bottom).

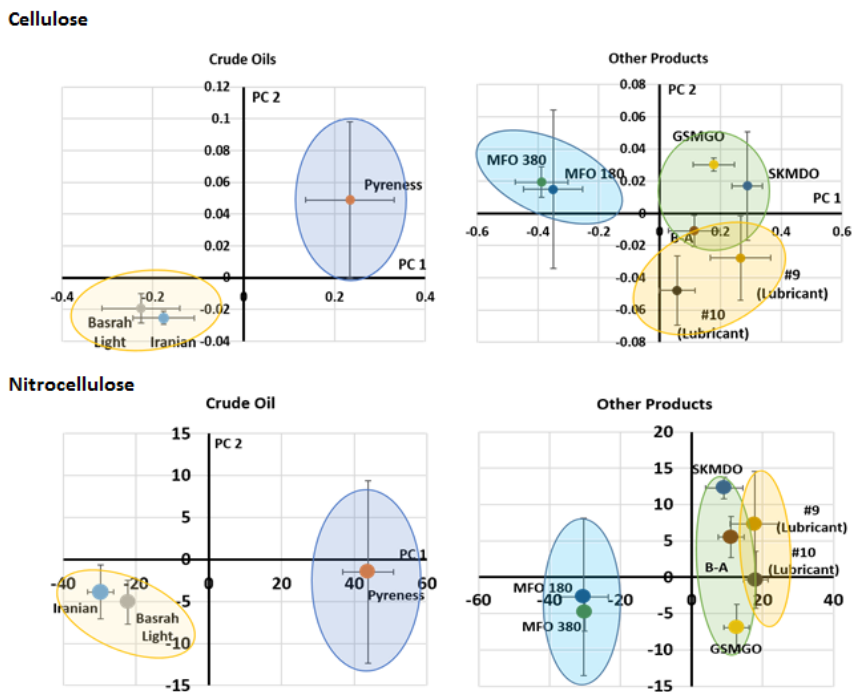


Figure D-4. PCA analysis of flow rate profiles on cellulose (top) or nitrocellulose (bottom) paper microfluidic chips for 10 different oil samples.

The PC-1 and PC-2 values obtained with PCA were compared with the material analysis table of the oil samples provided by KIOST (Table D-1). PC-1 is strongly correlated with resin content, both cellulose and nitrocellulose paper microfluidic chips, and PC-2 is strongly correlated with asphaltene content only on nitrocellulose. This is summarized in Table D-2 and D-3. According to cellulose data, the correlation between resin content and PC-1 is very clear. Therefore, it can be seen that PC-1 is a factor that represents resin content of the oil sample. However, PC-2 could not be statistically significant to any data in the provided physical analysis table, which is understandable considering that PC-2 data of cellulose paper accounts for only 4% of the data.

Table D-1. The material analysis of oil samples

Sample	Density g/cm <sup>3</sup>	Dynamic Viscosity mPa-S	Aromatic Content %	Resin Content %	Asphaltene Content %
<b>Crude oil</b>					
Basrah	0.86715	11.3	44.0	15.4	13.0
Iranian	0.87812	14.2	46.4	12.9	14.7
Pyreness	0.93576	147.7	47.7	8.5	0.8
<b>Marine fuel oil</b>					
GS_MGO	0.84820	4.5	32.3	1.3	No data
GS_180	0.97031	1091.0	55.0	19.9	18.1
GS_380	0.98336	2254.8	50.2	25.3	16.6
SK_MDO	0.89021	5.1	50.3	3.6	0.8
B-A	0.86316	4.7	22.6	3.8	0.9
<b>Lubricant oil</b>					
#9-SAE-40	0.89012	376.9	1.2	2.9	6.5
#10-SAE-40	0.88232	288.6	2.3	1.6	2.1

Table D-2. Correlation between PC-1 to resin content on cellulose data

Sample	Resin Content %	PC-1
MFO: GS-380	25.3	-0.388
MFO: GS-180	19.9	-0.349
Basrah	15.4	-0.226
Iranian	12.9	-0.177
LO: SAE-40 (Fresh)	1.6	0.058
MFO: B-A	3.8	0.114
MFO: MGO	1.3	0.178
Pyreness	8.5	0.234
LO: SAE-40 (Used)	2.9	0.267
MFO: SK-MDO	3.6	0.289

In the nitrocellulose data, similar to cellulose data (Table D-3), PC-1 is strongly correlated with resin content and PC-2 is strongly correlated with asphaltene content among the factors in the provided physical analysis table (table D-1).

In conclusion, nitrocellulose provides more information in the analysis of oil samples than cellulose, which is most likely due to the stronger negative polarity possessed by nitrocellulose. Both cellulose and nitrocellulose were about 10  $\mu\text{m}$  in pore size, and there were no other significant differences in physical properties.

Table D-3. Correlation between PC-1 and PC-2 to resin content and asphaltene content on nitrocellulose data

Sample	Resin Content %	PC-1	Sample	Asphaltene Content %	PC-2
MFO: GS-180	19.9	-30.4	MFO: MGO	no data	-6.92
MFO: GS-380	25.3	-30.1	Crude: Basrah Light	13	-5.07
Iranian	12.9	-29.8	MFO: GS-380	16.6	-4.77
Basrah	15.4	-22.2	Crude: Iranian Heavy	14.7	-3.85
MFO: SK-MDO	3.6	9.1	MFO: GS-180	18.1	-2.70
MFO: B-A	3.8	11.1	Crude: Pyreness	0.8	-1.48
MFO: MGO	1.3	12.7	LO: SAE-40 (Fresh)	2.1	-0.37
LO: SAE-40 (Used)	2.9	17.7	MFO: B-A	0.9	5.52
LO: SAE-40 (Fresh)	1.6	18.1	LO: SAE-40 (Used)	6.5	7.33
Pyreness	8.5	43.8	MFO: SK-MDO	0.8	12.30

### 3.3. Oil classification by t-SNE and SVM

The flow rate profiles were used for t-SNE analysis, a non-linear dimensionality deduction technique, and converted into two-dimensional plot. The separation is similar to the results from PCA, but the size of the error bars decreased when t-SNE is used as it is a nonlinear dimension reduction technique (Figure D-5). Both cellulose and nitrocellulose data clustered Iranian and Basrah crude oil very closely while Pyreness crude oil is significantly apart from them. In the cellulose data, GS-180 and GS-380 clustered together

(colored light blue) while GS-MGO, SK-MDO, and B-A formed another cluster (colored light yellow) among marine fuel oil samples. In the nitrocellulose data, GS-MGO was individually clustered (colored light green) by further distinguishing between marine fuel oil samples. However, unlike PCA, each axis was not correlated with any component in the provided physical analysis table.

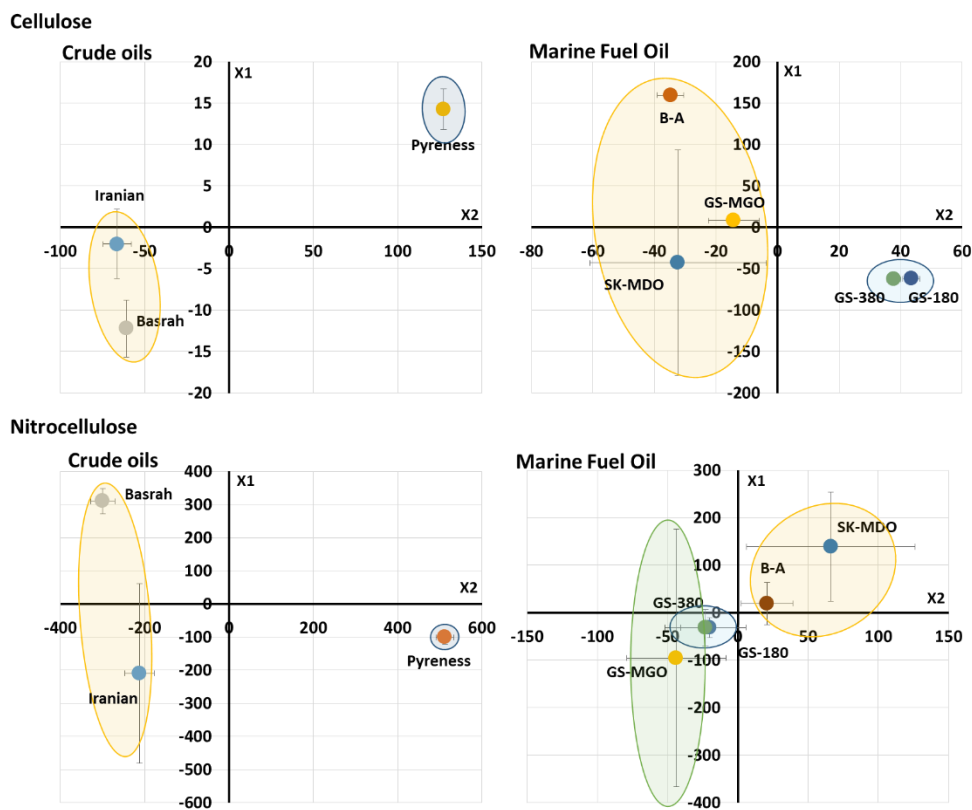


Figure D-5. t-SNE analysis of flow rate profiles on cellulose (top) or nitrocellulose (bottom) paper microfluidic chips for crude and marine fuel oil samples.

SVM was used for developing non-linear data model and classifying the oil samples using leave-one-out cross-validation. Pattern analysis is performed using N-1 data points

to develop a prediction model. The model developed was used to classify two thirds of the oil sample dataset through 30 random iterations. The analysis results for crude oil and marine fuel oil are summarized in Table D-4 and Table D-5. The cells marked in green diagonally from the top left to the bottom right indicate the number of cases in which the predicted results match the actual sample. Cells marked in yellow show incorrectly classified results by the model. In the case of cellulose paper microfluidic data, the incorrectly classified sample is limited to oils with similar chemical composition: Basrah and Iranian for crude oil, B-A and SK-MDO for marine fuel oil, and GS-180 and GS-380.

Table D- 4. Cross-validation results from SVM analysis on cellulose chips

Crude Oil	Basrah	Iranian	Pyreness		
	Light	Heavy			
Basrah	29	24	1		
Iranian	0	5	3		
Pyreness	1	1	26		

MFO	B-A	SK-MDO	MGO	GS-180	GS-380
B-A	6	15	0	1	0
SK-MDO	13	1	0	0	1
GS-MGO	7	1	30	0	0
GS-180	4	6	0	10	19
GS-380	0	7	0	20	9

Table D-5. Cross-validation results from SVM analysis on nitrocellulose chips

Crude Oil	Basrah	Iranian	Pyreness		
	Light	Heavy			
Basrah	4	9	0		
Iranian	21	8	0		
Pyreness	5	13	30		

MFO	B-A	SK-MDO	MGO	GS-180	GS-380
B-A	15	2	12	0	0
SK-MDO	11	28	0	0	0
GS-MGO	4	0	18	0	0
GS-180	0	0	0	22	25
GS-380	0	0	0	8	5

#### 4. Conclusion

To summarize, we developed an easy-to-use, low-cost and rapid assay for identifying the origin or type of oil through measuring the flow rate profile of each oil sample. A microfluidic paper chip was fabricated by wax printing on a paper substrate. An oil sample was placed on the chip and it flowed through the chip resulting in a unique flow rate-time profile, which was dependent on the composition of the oil. These activities were recorded with a Raspberry Pi camera, flow rate profiles were obtained, and such dataset

was classified by PCA and t-SNE. Both were capable of grouping and classifying different oil samples of similar composition. Additionally, the cross-validation model through SVM produced high accuracy predictions of origin or type of oil samples. This simple and effective assay will allow rapid fingerprinting analysis without need of laboratory equipment that cannot be operated in the field such as a ship on the sea.

### **Acknowledgements**

This research was funded by KIOST (Korea Institute of Ocean Science and Technology)

### **References**

- (1) Gaines, R. B.; Hall, G. J.; Frysiner, G. S.; Gronlund, W. R.; Juare, K. L. Chemometric Determination of Target Compounds Used to Fingerprint Unweathered Diesel Fuels. *Environ. Forensics* **2006**, *7* (1), 77–87.  
<https://doi.org/10.1080/15275920500506949>.
- (2) Yim, U. H.; Kim, M.; Ha, S. Y.; Kim, S.; Shim, W. J. Oil Spill Environmental Forensics: The Hebei Spirit Oil Spill Case. *Environ. Sci. Technol.* **2012**, *46* (12), 6431–6437. <https://doi.org/10.1021/es3004156>.
- (3) Permanyer, A.; Douifi, L.; Dupuy, N.; Lahcini, A.; Kister, J. FTIR and SUVF Spectroscopy as an Alternative Method in Reservoir Studies. Application to Western Mediterranean Oils. *Fuel* **2005**, *84* (2), 159–168.  
<https://doi.org/10.1016/j.fuel.2004.06.027>.
- (4) Mirnaghi, F. S.; Soucy, N.; Hollebone, B. P.; Brown, C. E. Rapid Fingerprinting of Spilled Petroleum Products Using Fluorescence Spectroscopy Coupled with

- Parallel Factor and Principal Component Analysis. *Chemosphere* **2018**, *208*, 185–195. <https://doi.org/10.1016/j.chemosphere.2018.05.111>.
- (5) Riley, B. J.; Lennard, C.; Fuller, S.; Spikmans, V. Pyrolysis-GC-MS Analysis of Crude and Heavy Fuel Oil Asphaltenes for Application in Oil Fingerprinting. *Environ. Forensics* **2018**, *19* (1), 14–26. <https://doi.org/10.1080/15275922.2017.1408163>.
- (6) Juahir, H.; Ismail, A.; Mohamed, S. B.; Toriman, M. E.; Kassim, A. Md.; Zain, S. Md.; Ahmad, W. K. W.; Wah, W. K.; Zali, M. A.; Retnam, A.; et al. Improving Oil Classification Quality from Oil Spill Fingerprint beyond Six Sigma Approach. *Mar. Pollut. Bull.* **2017**, *120* (1), 322–332. <https://doi.org/10.1016/j.marpolbul.2017.04.032>.
- (7) Klug, K. E.; Reynolds, K. A.; Yoon, J.-Y. A Capillary Flow Dynamics-Based Sensing Modality for Direct Environmental Pathogen Monitoring. *Chem. – Eur. J.* **2018**, *24* (23), 6025–6029. <https://doi.org/10.1002/chem.201800085>.
- (8) Kaarj, K.; Akarapipad, P.; Yoon, J.-Y. Simpler, Faster, and Sensitive Zika Virus Assay Using Smartphone Detection of Loop-Mediated Isothermal Amplification on Paper Microfluidic Chips. *Sci. Rep.* **2018**, *8* (1). <https://doi.org/10.1038/s41598-018-30797-9>.
- (9) Yetisen, A. K.; Akram, M. S.; Lowe, C. R. Paper-Based Microfluidic Point-of-Care Diagnostic Devices. *Lab. Chip* **2013**, *13* (12), 2210. <https://doi.org/10.1039/c3lc50169h>.
- (10) Pantoja, R.; Nagarah, J. M.; Starace, D. M.; Melosh, N. A.; Blunck, R.; Bezanilla, F.; Heath, J. R. Silicon Chip-Based Patch-Clamp Electrodes Integrated with PDMS

- Microfluidics. *Biosens. Bioelectron.* **2004**, *20* (3), 509–517.  
<https://doi.org/10.1016/j.bios.2004.02.020>.
- (11) Songjaroen, T.; Dungchai, W.; Chailapakul, O.; S. Henry, C.; Laiwattanapaisal, W. Blood Separation on Microfluidic Paper-Based Analytical Devices. *Lab. Chip* **2012**, *12* (18), 3392–3398. <https://doi.org/10.1039/C2LC21299D>.
- (12) Santhiago, M.; Henry, C. S.; Kubota, L. T. Low Cost, Simple Three Dimensional Electrochemical Paper-Based Analytical Device for Determination of p-Nitrophenol. *Electrochimica Acta* **2014**, *130*, 771–777.  
<https://doi.org/10.1016/j.electacta.2014.03.109>.
- (13) Stravers, C. S.; Gool, E. L.; van Leeuwen, T. G.; Aalders, M. C. G.; van Dam, A. Multiplex Body Fluid Identification Using Surface Plasmon Resonance Imaging with Principal Component Analysis. *Sens. Actuators B Chem.* **2019**, *283*, 355–362.  
<https://doi.org/10.1016/j.snb.2018.12.050>.
- (14) Imamura, R.; Murata, N.; Shimanouchi, T.; Yamashita, K.; Fukuzawa, M.; Noda, M. A Label-Free Fluorescent Array Sensor Utilizing Liposome Encapsulating Calcein for Discriminating Target Proteins by Principal Component Analysis. *Sensors* **2017**, *17* (7), 1630. <https://doi.org/10.3390/s17071630>.
- (15) Maaten, L. van der; Hinton, G. Visualizing Data Using T-SNE. *J. Mach. Learn. Res.* **2008**, *9* (Nov), 2579–2605.
- (16) Miao, A.; Zhuang, J.; Tang, Y.; He, Y.; Chu, X.; Luo, S. Hyperspectral Image-Based Variety Classification of Waxy Maize Seeds by the t-SNE Model and Procrustes Analysis. *Sensors* **2018**, *18* (12), 4391.  
<https://doi.org/10.3390/s18124391>.

- (17) Kernel Parameter Selection for Support Vector Machine Classification - Zhiliang Liu, Hongbing Xu, 2014 <https://journals.sagepub.com/doi/abs/10.1260/1748-3018.8.2.163> (accessed Jul 14, 2019).
- (18) Cohen, J. A Coefficient of Agreement for Nominal Scales. *Educ. Psychol. Meas.* **1960**, 20 (1), 37–46. <https://doi.org/10.1177/001316446002000104>.